$\cancel{\;}$ C.3

SERI/TP-32-206

ELECTRICAL PROPERTIES OF POLYCRYSTALLINE
SEMICONDUCTOR THIN FILMS

LAWRENCE L. KAZMERSKI

TO BE PUBLISHED AS CHAPTER 3 OF
A FORTHCOMING BOOK, PROPERTIES OF
POLYCRYSTALLINE AND AMORPHOUS THIN
FILMS AND DEVICES, L.L. KAZMERSKI,
EDITOR; ACADEMIC PRESS, PUBLISHER.

Solar Energy Research Institute

1536 Cole Boulevard
Golden, Colorado 80401
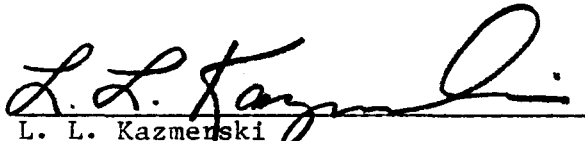
A Division of Midwest Research Institute

ELECTRICAL PROPERTIES OF POLYCRYSTALLINE SEMICONDUCTOR THIN FILMS

Lawrence L. Kazmerski

To be published as Chapter 3 of
a forthcoming book, PROPERTIES OF
POLYCRYSTALLINE AND AMORPHOUS THIN
FILMS AND DEVICES, L.L. KAZMERSKI,
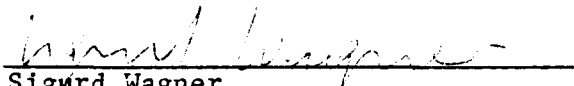EDITOR; ACADEMIC PRESS, PUBLISHER.

PREFACE

The understanding and subsequent control of the electrical properties of thin films have become very important due to the evolution of devices based upon these thin material layers. This is especially true for photovoltaics, since the potential economic, large-scale deployment of such devices depends largely upon substantial progress in this area. Although a number of books and reviews are available which adequately cover the properties of discontinuous metal and insulator films, the overall treatment of carrier transport mechanisms in polycrystalline semiconductor thin films has been heuristic and superficial. Since many of the major contributions to this field remain segmented in the literature, it is the purpose of this work to delineate the basic electrical mechanisms, to integrate and compare recent contributions to previous research, and to provide a general basis for understanding thin semiconductor film properties.

This report has been completed as part of the FY79 Photovoltaics Branch research task, 3221.10. It also serves as a chapter in the forthcoming book Properties of Polycrystalline and Amorphous Thin Films and Devices, published by Academic Press and edited by L. L. Kazmerski. This limited access report is being distributed with the permission of the publisher and should not be reproduced further.

L. L. Kazmerski
Photovoltaics Branch

Sigurd Wagner
Branch Chief, Photovoltaics

CONTENTS

CONTENTS (continued)

CHAPTER 3

ELECTRICAL PROPERTIES OF POLYCRYSTALLINE SEMICONDUCTOR THIN FILMS

3.1 INTRODUCTION

This chapter focuses on the basic electronic transport in polycrystalline semiconductor thin films. A number of books [1] and reviews are available that cover in detail the properties of discontinuous [2], metal [3, 4], and insulator films [5]. Except for earlier reviews by Anderson [6] and Bube [7], the treatment of carrier transport mechanisms in polycrystalline semiconductor thin films has been largely heuristic and superficial. Although the identification of the electrical properties of these films is an expanding area of research, many of the major contributions to this field remain segmented in the literature. It is the purpose of this chapter to delineate the basic mechanisms involved, to integrate and compare some recent contributions with earlier work, and to provide a general basis for understanding thin semiconductor film properties.

In this chapter, the carrier transport is considered separately for two cases. First, the electrical characteristics of perfect, single-crystal thin films are examined. These transport properties are regarded as essentially those of the bulk crystalline semiconductor, but they are altered by the major physical feature of the film--the surface. Flat-band and surface-band bending conditions are investigated and film thickness effects are identified. Second, transport mechanisms in polycrystalline films are discussed. In this case, the complicating factors of film defects and discontinuities are considered, with some emphasis on the grain boundary. The combined effects of surface scattering and defect-dominated properties are also indicated.

At the onset of this chapter, it must be emphasized that the identification and definition of electronic transport in polycrystalline semiconductor films has largely been a modeling effort. At this writing, no universal explanation of transport characteristics exists for thin films. Differences should be anticipated. For example, polycrystalline compound semiconductor films can

gain their extrinsic character by stoichiometry control, but elemental semiconductors by doping. Grain boundaries differ not only between those two types but also between large-grained and small-grained materials. The understanding and control of the electrical properties of thin semiconductor films has now progressed from a scientific curiosity to a necessity. The potential economic, large-scale deployment of devices based upon these thin films depends upon substantial progress in this area. While the thin-film research veteran may express caution or hesitancy because of the magnitude or seeming unsolvability of the problems, the challenge envisioned by others might bring about the solutions. It is hoped that this chapter might serve especially the latter group.

3.2 TRANSPORT IN THIN CRYSTALLINE FILMS

1. Definitions and Formulations

In this section, the most simple case of a semiconductor thin film is considered--the continuous single-crystal film. Conceptually, the situation avoids the complicating factors of film defects, defect structures (e.g., dislocations, stacking faults, grain boundaries, etc.) and other discontinuities as may affect conduction mechanisms. Therefore, the transport properties can be regarded as essentially those of the bulk crystalline material, influenced and altered by the remaining major physical feature of the film--the surface.

The surface of a thin film affects the electrical transport properties of a material, whether a semiconductor or a metal, by limiting the traversal of the charge carriers and their mean free paths. Even bulk materials experience these surface effects, but they are more pronounced in thin films because of the large surface-to-volume ratios. When the thickness of the film becomes less than or comparable to the mean free path of the carriers, the scattering of the electrons and holes from the film surfaces has measurable effects on carrier transport properties and can dominate the electrical characteristics of the film. Of course, the extent of the influence of surface scattering

depends upon the nature of the scattering mechanism(s) involved. The two limiting cases are:

- Specular Reflection: During the scattering process, the carriers (electrons or holes) have only their velocity component perpendicular to the surface reversed and their energy remains constant. Since no losses occur, there is no effect on conductivity. The surface represents a perfect reflector and the scattering is elastic.

- Diffuse Reflection: After scattering, the carriers emerge from the surface with velocities independent of their incident ones. This process is indicative of inelastic or random scattering. The change in momentum leads to a related change in conductivity.

Specular reflection is the type of scattering expected from an ideal surface. Real surfaces exhibit some amount of disorder which, in turn, results in some degree of diffuse scattering. The extent of diffuse scattering is determined by the type, density, and cross sections of the surface defects. The major mechanisms, primarily surface charge impurities and electron-phonon interactions, that determine the extent of diffuse or specular scattering have been treated in detail by Greene [8-10] and Tavger et al. [11-13]. Quantitatively, total diffuse scattering can lower effective film conductivities and mobilities more than an order of magnitude below their single-crystal, bulk magnitudes. For a real surface, both partial specular/partial diffuse scattering mechanisms exist and the resultant electrical properties usually lie between those predicted by either scattering mode.

This section discusses the perfect semiconductor thin film, relating the effective film transport properties as influenced by surface conditions to the predicted bulk behavior. Bulk properties are summarized, and the effects of diffuse and specular reflection are related. Two surface conditions are considered. The first models the film with energy bands constant to the surface itself. This is commonly called the flat-band condition and is illustrated schematically in Fig. 3-1a. Although this case is somewhat

artificial and does not exactly represent the situation for the real semiconductor surface region, it is instructive and provides a basis for understanding the various scattering phenomena and their effects. Because of its simplicity, the flat-band model can be used to predict transport properties and has been used to explain the general electrical behavior of some films. The second model includes band-bending at the surface. The existence of surface states complicates the transport mechanisms. Band structures for surface depletion, inversion and accumulation are illustrated in Figs. 3-1b, c, and d, respectively. Effects of band bending on semiconductor film properties have been studied, but it is not easy to control surface state densities and associated surface potentials by or during film growth processes. Field effect techniques, discussed later in this section, can be utilized to demonstrate the relationships between the degree of the non-flat-band condition and the resulting electrical properties of the thin semiconductor films.

For all film geometries in this chapter, the coordinate system shown in Fig. 3-2 has been adopted. The z-direction is perpendicular to the film surface and the total film thickness defined in this direction is d.

2. Essential Transport Phenomena

In evaluating electrical characteristics of thin films, it is common to compare the film's behavior to that of the bulk crystal. If the bulk crystal were perfect, the electrons and holes could flow unimpeded in the perfect periodic potential. In the absence of external fields, each carrier would maintain its velocity and wavevector indefinitely. However, in the real bulk crystal lattice vibrations, impurities, and defects could deviations from the ideal behavior. The carriers experience a nonzero scattering probability which provides for a random movement and continual velocity change for the electrons or holes. A drift current results when an electrical field is imposed.

The various scattering processes can each be characterized by a fundamental relaxation time, τ, defined as the average time required for a disturbance in the electron distribution to fade by the random action of the scattering. Two scattering processes are especially important for bulk crystal behavior: first, scattering by lattice vibrations, dominant in chemically pure crystals at ordinary temperatures; and second, scattering from impurity centers. For the first case, the relaxation time is [14]

$$\tau_{\ell} \sim T^{-1} E^{-1/2} \qquad [3.1]$$

where T is the temperature and E the carrier energy. In case 2, scattering occurs from impurity centers, such as ionized impurities. In this case [14]

$$\tau_{i} \sim E^{3/2}/N_{i} \qquad [3.2]$$

where N_{i} is the density of ionized impurities. All scattering mechanisms act simultaneously to some extent in real crystals. The total bulk relaxation time, considering each of the scattering mechanisms to be essentially independent, is given by [14]

$$1/\tau_{b} = 1/\tau_{\ell} + 1/\tau_{i} + \ldots \qquad [3.3]$$

In order to relate the effects of the various scattering phenomena to the determination of the transport equations, the relaxation times are incorporated into the Boltzmann transport equation [15]. From this, the current-field relationship can be generated and the pertinent transport parameters (mobility, conductivity, carrier concentration) can be extracted. Following this procedure, the temperature dependencies of the lattice and the ionized impurity scattering carrier mobilities can be expressed [14]:

$$\mu_{\ell} = CT^{-3/2} \qquad [3.4]$$

and

$$\mu_{i} = C'T^{3/2} \qquad [3.5]$$

respectively, where C and C' are constants. In addition, when both types of scattering are present and noninteracting, the mobilities "add" according to the relaxation times (Eq. 3.3), with the effective bulk crystalline mobility given by [16].

$$1/\mu_b = 1/\mu_\ell + 1/\mu_i \qquad [3.6]$$

From Eqs. 3.4 and 3.5 it is apparent that lattice scattering predominates at high temperatures and impurity scattering at lower temperatures. The transition from the domination by one type to the other depends upon the material and the impurity nature and concentration. Some deviations from the "3/2 law" are encountered in real semiconductors due to complex band structures as well as optical-phonon scattering. Experimentally it has been found that the mobility variations usually range from $T^{-5/2}$ to $T^{5/2}$ dependencies. For example, near room temperature the electron and hole mobilities for GaP follow Eq. 3.4, whereas for silicon, $\mu_n \sim T^{-5/2}$ [17].*

3. The Effects of Surfaces on Carrier Transport

The bulk transport case summarized briefly in the previous section must be modified even for the single-crystal thin film since the surface can scatter a greater number of carriers than the number not being scattered. It is assumed that the flat-band condition holds for the analysis in this section. The perturbations due to band-bending are included in Section 4.

---

*In general, the temperature dependence of the mobility of a crystalline semiconductor can be expressed [13]

$$\mu \sim T^{\alpha + \beta/2} \qquad [3.7]$$

where α and β are constants whose magnitudes and signs are indicative of the dominant scattering mechanism(s).

a. Flat—Band Conditions: Rigorous Treatment

The method utilized to incorporate the effects of surface scattering is similar to that cited for bulk phenomena in the previous section and starts with the Boltzmann equation [15]

$$a\nabla_c f + c\nabla_r f = (\partial f/\partial t)_{scattering}$$ [3.8]

where a and c are the acceleration and the velocity of the scattered carriers, respectively, and f is the distribution function. This theoretical approach applied to surface scattering has been reported by Fuchs [18], Sondheimer [19], Lucas [20], Tavger [13], Zemel [20], Anderson [6], Frankl [22], and Fleitner [23]. Reviews have also been compiled by Campbell [24], Mayer [25], Chopra [26], and Many et al. [27]. When an electric field, $\mathcal{E}$, is applied in the x-direction, Eq. 3.8 reduces to a one-dimensional representation for the geometry shown in Fig. 3-2, in which the x and y film dimensions are very much greater than d, the film thickness. Therefore,

$$\frac{-q\mathcal{E}_x}{m^*} \frac{\partial f}{\partial c_x} + c_z \frac{\partial f}{\partial z} = \frac{(f-f_o)}{\tau}$$ [3.9]

The distribution function can be written [6, 27]

$$f = f_o + f_1(c,z)$$ [3.10]

since the perturbation, f_1, is independent of x and y. The general form of the solution of the differential equation (Eq. 3.9) is [27]

$$f_1 = \frac{q\mathcal{E}_x \tau}{m^*} \frac{\partial f_o}{\partial c_x} [1 + F(c) \exp(-z/\tau c_z)]$$ [3.11]

where the functional form of F(c) depends upon the boundary conditions.

If the upper and lower surfaces of the film are identical, from the symmetry of the situation

$$f_1(c_{x,y},c_z;z) = f_1(c_{x,y},-c_z;d-z)$$ [3.12]

Therefore, two solutions of Eq. 3.12 are found [6, 27]:

$$c_z \geq 0 : f_1 = f_1^+ = \frac{q \mathcal{E} \tau}{m^*} \frac{\partial f_0}{\partial c_x} [1 + F(c) \exp(-x/\tau c_z)] \qquad [3.13a]$$

and

$$c_z \leq 0 : f_1 = f_1^- = \frac{q \mathcal{E} \tau}{m^*} \frac{\partial f_0}{\partial c_x} [1 + F(-c) \exp((d-z)/\tau c_z)] \qquad [3.13b]$$

However, it has already been noted that carriers can be scattered diffusely from the surface, and the solutions given by Eqs. 3.13a and 3.13b represent the specular case only. The condition of the surface and its effect on the carrier transport can now be introduced in a simple fashion. From Eq. 3.10 the distribution function of carriers <u>arriving</u> at the surface is given by

$$f' = f_0 + f_1^+ \qquad [3.14]$$

If some fraction, p, of these undergo <u>specular reflection,</u> their resultant distribution function <u>leaving</u> the surface is

$$f'' = p (f_0 + f_1^-) \qquad [3.15]$$

The fraction p is called the specular scattering factor, with p=1 indicating pure specular reflection and p=0 entirely diffuse reflection. The remaining carriers leaving the surface, 1-p, are scattered diffusely, and their distribution function is

$$f''' = (1-p) f_0 \qquad [3.16]$$

But,

$$f' = f'' + f''' \qquad [3.17]$$

or

$$f_0 + f_1^+ = p(f_0 + f_1^-) + (1-p) f_0 \qquad [3.18]$$

Substituting Eqs. 3.13a and 3.13b into Eq. 3.18 yields [6]

$$F(c) = - (1-p)/[1 - p \exp(-d/\tau c_z)] \qquad [3.19]$$

The carrier current density is calculated by inserting F(c) into Eq. 3.11 and integrating the product of the velocity, density of states, and distribution functions; that is,

$$J_x = -q \int_c c_x N_c f_1 dc$$

$$= nq\mu'$$

[3.20]

where μ' is the effective film mobility.

Two solutions for the mobility result, depending on whether the semiconductor is degenerate or nondegenerate. For the former case, in which Fermi-Dirac statistics apply, the ratio of the effective to the bulk mobility is [6, 27]

$$\frac{\mu'}{\mu_b} = 1 - \frac{3(1-p)}{2(d/\lambda)} \int_1^\infty \left(\frac{1}{\xi^3} - \frac{1}{\xi^5}\right) \left[\frac{1 - \exp(-(d/\lambda)\xi)}{1 - p\,\exp(-(d/\lambda)\xi)}\right] d\xi$$

[3.21]

where is the carrier mean free path. For the nondegenerate semiconductor case having spherical energy surfaces, Boltzmann statistics apply and [6],

$$\frac{\mu'}{\mu_b} = 1 - (1-p)(2\lambda/d) + (1-2p)(2\lambda/d)\ \Gamma_1\left(\frac{2\lambda}{d}\right) + (2p\lambda/d)\ \Gamma_1\left(\frac{\lambda}{d}\right)$$

[3.22]

where

$$\Gamma_1\left(\frac{n\lambda}{d}\right) = \int_0^\infty \exp\left[-\epsilon - (d/n\lambda)(\pi\epsilon)^{-1/2}\right] d\epsilon$$

[3.23]

and n = 1 or 2.

The functional dependencies of the mobility ratios for the degenerate and nondegenerate cases (predicted by Eqs. 3.21 and 3.22, respectively) are shown in Fig. 3-3. Surface scattering is more dominant for the nondegenerate semiconductor than for the corresponding degenerate semiconductor or metal. As the semiconductor becomes more degenerate, the effect of surface scattering becomes less significant.

Anisotropy of the effective mobility can result if the semiconductor has nonspherical equal-energy surfaces. The case of ellipsoidal energy surfaces has been considered by Ham and Mattis [28]. Their refinement of the previous spherical case indicates a fractional difference in mobility magnitudes for

different crystal directions. Fig. 3-4 presents their results for the completely diffuse (p=0) scattering case, for a diamond structure nondegenerate semiconductor. The symbol "n" refers to the direction normal to the film surface and "j" is the current density. For a given thickness, the value of μ' depends significantly upon the current direction and can be as much as an order of magnitude lower than that presented in Fig. 3-3. Thus the semiconductor thin film might be even more sensitive to the surface condition and film thickness than the previous analysis indicates, and some caution must be exhibited in applying this interpretation for transport in thinner semiconductor films.

b. Flat-Band Conditions: Simplified Approach

Another more simple approach can be used to predict the effect of surface scattering and film thickness on transport properties. For a nondegenerate semiconductor, assuming flat-bands and noninteracting scattering mechanisms, the total relaxation time using Matteissen's rule [16] is

$$1/\tau' = 1/\tau_s + 1/\tau_b \qquad\qquad [3.24]$$

where τ_s represents the average time a carrier requires to collide with the surface toward which it is moving and τ_b is defined in Eq. 3.3. The mean free distance of a carrier from a surface is approximately the film half thickness, d/2. If the unilateral mean velocity v_z is defined as the average over the positive (or negative) z-direction veocity component of all carriers, then the average surface scattering time can be estimated by [27]

$$\tau_s \simeq \frac{d/2}{v_z} \qquad\qquad [3.25]$$

But since the unilateral mean free path, λ, is defined as [27]

$$\lambda = \tau_b \, v_z \qquad\qquad [3.26]$$

Then,

$$\tau_s \simeq (d/2\lambda)\tau_b \qquad\qquad [3.27]$$

Combining Eq. 3.24 and 3.27, the effective mobility becomes [27]

$$\mu' = \mu_b/(1+2\lambda/d) \qquad\qquad [3.28]$$

This simple derivation assumes that the surface scattering is entirely specular (p=1). To generalize to the case in which a fraction p of the carriers is scattered inelastically (diffuse scattering), it is necessary to adjust the expression for τ_s, which represents the reciprocal per unit time probability that an electron will be scattered by a surface. Since p is the fraction undergoing specular (elastic) scattering, (1-p) is the fraction undergoing diffuse (inelastic) scattering, and the surface scattering term in Eq. 3.28 becomes $(1-p)/\tau_s$. Thus, the mobility can be written [6, 27]

$$\mu' = \mu_b \left[1 + (1-p)(2\lambda/d)\right]^{-1} \qquad\qquad [3.29]$$

The good agreement of Eq. 3.29 with the more rigorously derived Eq. 3.22 is shown in Fig. 3-3.

The conditions of the upper and lower surfaces of a thin film might be expected to be quite different since one is in contact with a supporting substrate and the other is exposed to a dissimilar environment (gas, solid, or liquid). In this situation, the contributions from each surface can be averaged (a first order approximation) and p can be replaced by (p+q)/2 where p and q are the specular scattering coefficients from the upper and lower film surfaces, respectively. Thus, Eq. 3.29 becomes [29]

$$\mu' = \mu_b \left[1 + (2\lambda/d)\left(1 - \frac{p+q}{2}\right)\right]^{-1} \qquad\qquad [3.30]$$

This same substitution can be incorporated directly into Eq. 3.22, keeping the formulation and the results consistent.

c. Effective Surface Scattering Length

In effect, the parameter λ is a measure of the influence of the surface upon the carrier transport. The surface scattering length is defined in terms of the mean velocity of the carriers [27, 29, 30].

$$\lambda = v_z \tau_b \qquad\qquad [3.31]$$

where τ_b is the bulk relaxation time. The velocity component is measured perpendicular to the film surface over which it is being averaged. This mean velocity is given by

$$v_z = (kT/2m*)^{1/2} \qquad\qquad [3.32]$$

Therefore, combining Eq. 3.32 with Eq. 3.31 and noting that $\mu_b = q\tau_b/m*$, one can express the mean surface scattering length as [30]

$$\lambda = C'\mu_b \, T^{1/2} \qquad\qquad [3.33]$$

where $C' = (m*k/2\pi q^2)^{1/2}$. Fig. 3-5 shows the dependence of λ/μ_b on temperature, indicating the predicted dependence of Eq. 3.33 for CdS films [29].

The magnitude of λ is material dependent. For carrier concentrations comparable to the CdS (i.e., 10^{15}-$10^{16}/cm^3$), $\lambda = 1.95$ μm, 0.85 μm, and 0.12 μm for Si, GaAs, and Ge, respectively [31]. Thus, surface scattering is expected to affect the electrical properties of Si more than those of the other semiconductors at a given film thickness. For a 1 μm thick film, the mobility of Ge is expected to be only about 5% less than its bulk value, while that for Si is about 55% less.

4. Effects of Band-Bending at Surface

The derivations of the previous sections assumed that the semiconductor energy bands were constant from the bulk to the surface itself. If surface states exist, some degree of band-bending at the surface will result under the following conditions:

- Depletion: Majority carriers can be trapped in acceptor-type surface states (n-type semiconductor) or donor-type surface states (p-type semiconductor) at energy levels below or above the Fermi level, respectively. In the case of an n-type semiconductor, electrons are repelled from the surface region making it less n-type (i.e., the surface is depleted of electrons). The band edges will bend up at the surface, away from the Fermi level. If this bending is sufficient, the surface can become p-type (i.e., the Fermi level is closer to the valence band) and this condition is called inversion. For a p-type semiconductor, holes are repelled from the surface and the band edges bend down toward the Fermi level. Once again, if this bending is sufficient, the surface region can be inverted (i.e., become n-type). The effect is equivalent to applying a negative bias to the surface of the p-type semiconductor, or a positive bias to the surface of the n-type semiconductor.

- Accumulation: This situation is the converse to depletion. Donor states at the surface of an n-type semiconductor, or acceptor states for a p-type semiconductor, contribute additional majority carriers (accumulation of majority carriers) to the conduction or valence bands, respectively. The band edges will bend toward the Fermi level (i.e., bend downward for the n-type and upward for the p-type semiconductor). The effect here is the application of a positive bias to the surface of the p-type semiconductor, or a negative bias to the surface of the n-type semiconductor.

Depletion and accumulation are illustrated in Fig. 3-1 in comparison to the flat-band case. Generally, the free surface of an impurity semiconductor is in depletion unless external fields are applied. The depletion condition will

therefore receive emphasis in subsequent sections.

a. The Surface Space Charge Region

Fig. 3-1 shows that the extent of the penetration of the surface depletion region is significant. The width of this region, L_c, depends upon the condition of the surface (surface charge, surface potential) and the condition of the bulk semiconductor (doping concentrations, Fermi level position, intrinsic concentration). For example, Waxman et al. [78] calculated the effective layer thickness for CdS as a function of the surface potential ($v_s = qV_s/kT$), as shown in Fig. 3-6. The change in L_c is predicted to be more than an order of magnitude for a corresponding 0-0.2 eV change in qV_s. Many et al. [27] carefully considered this problem, using a solution of the Poisson's equation

$$\frac{d^2v}{dz^2} = - (\rho/\epsilon kT)$$

$$= -(q^2/\epsilon kT)[n_b - p_b + p_b \exp(-v) - n_b \exp(v)]$$

[3.34]

where ϵ is the semiconductor permittivity, n_b and p_b are the bulk carrier concentrations, and v is a dimensionless potential ($= qV/kT$). The potential barrier V is defined as the potential at any point in the space charge region with respect to the value in the bulk (i.e., $V = \phi - \phi_b$).

For the case of small perturbations (e.g., $|v| \leq 1/2$), the integration of Eq. 3.34, applying the boundary condition $[(dv)/(dz)]|_{z=0} = 0$, yields [26]

$$\frac{dv}{dz} = \mp \frac{F(v,u_b)}{L}$$

[3.35]

where L is the effective Debye length ($= [\epsilon kT/q^2(n_b+p_b)]^{1/2}$); u_b is a reduced potential ($= q\phi_b/kT$); and [26]

$$F(v,u_b) = 2^{1/2}\left[\frac{\cosh(u_b+v)}{\cosh(u_b)} - v\,\tanh(u_b) - 1\right]^{1/2}$$

[3.36]

The minus sign in Eq. 3.35 refers to v>0, and the plus sign to v<0.

The resultant potential-penetration profile was obtained by Many et al. by numerically integrating the complex Eq. 3.35. The potential barrier |v| is shown as a function of z/L, a normalized distance from the surface, Fig. 3-7. This profile is significant for thin films. The band diagram for the depletion condition (Fig. 3-1b) shows that the reduced potentials, v and u_b, are opposite in sign. The flat-band condition exists when v(0) = 0. Band-bending continues until v(0) = $-2u_b$. In this condition, the semiconductor is quasi-intrinsic since the minority carrier density equals the majority carrier density in the bulk (i.e., in terms of the band diagram, the Fermi level now lies below E_i, the midgap energy, by the same amount, u_b, that it was positioned above it in the flat-band condition). As the band-bending continues (|v(0)| > $2u_b$), the total inversion condition is reached and the surface undergoes a change in majority carrier type.

Consider a film with $|u_b|$ = 6 (i.e., the Fermi level lies about 0.15 eV above mid-gap for the n-type semiconductor at room temperature). At z/L ~ 0.7, the quasi-intrinsic condition holds. Therefore, if d ~ 2(z/L) or approximately 1.4, the film would appear intrinsic. Anderson observes that this situation corresponds physically to having the total number of carriers dominated by the surface trapping mechanism due to the small volume of the film. It can be observed further that for higher doping levels ($|u_b|$ > 6), quite thinner films would be needed to provide the intrinsic appearance.

An interesting situation results when the band-bending occurs at both the upper and lower surfaces of the film. For a sufficiently thin film, the conduction and valence band edges cannot reach the positions with respect to the Fermi level that would be expected for a corresponding bulk material with the pertinent doping level. This situation is illustrated simplistically in Fig. 3-8. It is interesting to note that if the film is thin enough, the band-bending can develop only to a small extent [33, 34]. As a result, the potential and carrier concentrations appear almost uniform throughout the film, and the transport properties are characterized by the less complicated flat-band models (e.g., Eqs. 3.22 and 3.29).

b. Surface Transport Parameters

A major effect of the band-bending phenomenon is the generation of an excess
or a deficiency of mobile carriers within the surface region. These
quantities are defined [27]

$$\Delta N = \int_0^\infty (n-n_b) \, dz \qquad [3.37a]$$

and

$$\Delta P = \int_0^\infty (p-p_b) \, dz \qquad [3.37b]$$

where $p = p_b \exp(-v)$ and $n = n_b \exp(v)$. Since ΔN and ΔP are surface quantities,
they have per-unit-area units. Many et al. [27] solved these integrals
numerically for accumulation, depletion, and inversion conditions. These
parameters can be related to the carrier transport since ΔN and ΔP effect a
change in the surface conductivity

$$\Delta\sigma = q(\mu_{ns}\Delta N + \mu_{ps}\Delta P) \qquad [3.38]$$

where $\Delta\sigma$ is expressed per unit surface area, and μ_{ns} and μ_{ps} are the electron
and hole surface mobilities, respectively. The surface conductivity change
can be measured although it depends greatly on the nature and magnitude of the
surface potential. Although it is fairly simple to measure the surface
conductance it is impossible to separate the product $\mu_{ns} \Delta N$ (or $\mu_{ps} \Delta P$)
without some further theoretical estimates.

The surface mobilities, μ_{ns} and μ_{ps}, can be calculated, and their
relationships to the surface conditions can be predicted. The general case of
nonparabolic bands for a nondegenerate or degenerate semiconductor has been
treated by Juhasz [35]. For either the depletion or accumulation he showed
that

$$\frac{\mu_{ns}}{\mu_b} = 1 - \frac{\lambda n_b}{\Delta N} H_n(v) \qquad [3.39]$$

and

$$\frac{\mu_{ns}}{\mu_b} = 1 - \frac{\lambda p_b}{\Delta P} H_p(v) \qquad [3.40]$$

where n_p and p_b are bulk concentrations and $H_n(v)$ and $H_p(v)$ are functions which reduce to the Γ functions derived by Many et al. [27] and are presented in Eq. 3.23 for a nondegenerate semiconductor. The dependence of μ_{ns}/μ_b on surface potential is presented in Fig. 3-9 for both degenerate and nondegenerate cases. For the nondegenerate case, μ_{ns}/μ_b decreases with increasing v_s as expected. However, a maximum of unity (i.e., $\mu_{ns}=\mu_b$) is not predicted for the $v_s=0$ (i.e., no band-bending) case. In this limit, μ_{ns} corresponds to the surface mobility with normal diffuse scattering. For the degenerate film, the reasons for the mobility cusp as v_s approaches zero have been discussed by Greene [9] and Frankl [22]. Similar electrical characteristics have been derived by Covington and Ray [33] and Hezel [36].

Anderson [6] calculated the effective mobilities for the band-bending case by modeling the surface region as shown in Fig. 3-10. The surface region of width L_c is approximated by two independent mean scattering times. The first is associated with bound carriers. These carriers are constrained to move in the surface potential well and scatter diffusely at the surface ($z=0$) but specularly at the boundary ($z=L_c$). The second is associated with unbound electrons. These have energies above the well and are scattered at the surface under a flat-band condition modified by the surface potential. The resultant mean surface scattering times are given by:

$$1/\tau_s = 1/\tau_s(\text{bound}) + 1/\tau_s(\text{unbound}) \qquad [3.41]$$

$$1/\tau_s = \frac{(1-p)\lambda(1+v_s)^{1/2}}{L_c \tau_b} + \frac{(1-p)\lambda(1+v_s)^{1/2}}{d\tau_b} \qquad [3.42]$$

When this modified surface scattering time is substituted into Eq. 3.24 for a surface accumulation layer, the effective mobility is [6]

$$\frac{\mu'}{\mu_b} = \left\{ 1 + (1-p)\lambda\left[(1/L_c) + (2/d)\right]\left[1 + qV_s/kT\right]^{1/2} \right\}^{-1} \qquad [3.43]$$

For the more common depletion-layer at the surface of the semiconductor film [6],

$$\frac{\mu'}{\mu_b} = \frac{1 + (1-p)(2\lambda/d)[1 - \exp(qV_s/kT)]}{1 + (1-p)(2\lambda/d)} \qquad [3.44]$$

Eqs. 3.43 and 3.44 are both consistent with the expression derived for the flat-band situation. As $V_s \rightarrow 0$ and $L_c \rightarrow \infty$, these equations are identical to Eq. 3.29. The effects of the surface potential on the mobility are illustrated in Fig. 3-11.

c. Hall Effect Parameters

The previously derived expressions for film mobilities apply to the measurement of Hall mobility under small (normal) magnetic fields. However, the measured carrier concentrations are surface scattering and thickness dependent, just as for the cases of mobility or resistivity, when the number of carriers being scattered from the surface is much greater than the number not being scattered. The relationship of this scattering mechanism to the magnitude of the Hall constant has been treated by Amith [37] who solved the Boltzmann equation for an extrinsic semiconductor with an additional drift field due to an applied magnetic field. The result indicates that the effective Hall constant, R_H', is related to the crystalline quantity, R_{Hb}, through the expression

$$R_H' = \eta(\lambda/d)R_{Hb} \qquad [3.45]$$

where the solution of the Boltzmann equation yields

$$\eta(\lambda/d) = \frac{1 - 4\lambda/d + 4(\lambda/d)\,\Gamma_1(\lambda/d) + \Gamma_3(\lambda/d)}{\left\{1 - 2\lambda/d + (2\lambda/d)\,\Gamma_1(\lambda/d)\right\}^2} \qquad [3.46]$$

and $\Gamma_3 = \int_0^\infty (\epsilon\pi)^{-1/2}\Gamma_1(\lambda/d)d\epsilon$ with $\Gamma_1(\lambda/d)$ defined in Eq. 3.23. Values for Γ_1 and Γ_3 can be gained by numerical integration, and the resulting general dependence of $\eta(\lambda/d)$ upon the mean scattering length and thickness is shown in Fig. 3-12.

Zemel et al. [21, 38-40] compared the relative mobilities for a semiconductor film with a surface space-charge region present both without and with an applied magnetic field. With no magnetic field [21],

$$\frac{\mu'}{\mu_b} = 1 - \exp(\alpha^2) \, \text{erfc}(\alpha) \qquad\qquad [3.47]$$

where $\alpha = L_c(2mkT)^{1/2}/q\tau V_s$. This expression is similar to that derived earlier by Petritz [41] for semiconductors and Schrieffer [42] for metals. With a magnetic field present, Zemel showed that [21]

$$\left(\frac{\mu'}{\mu_b}\right)_{R_H} = [1 - \frac{2\alpha}{\pi^{1/2}} - \left(1-2\alpha^2\right)\exp(\alpha^2) \, \text{erfc}(\alpha)]^{1/2} \qquad\qquad [3.48]$$

where the subscript R_H indicates a Hall measurement. Eqs. 3.47 and 3.48 are compared as functions of α in Fig. 3-13, and the difference is quite small. For minimal band-bending, V_s approaches zero and α becomes large. As expected, $\mu' = \mu_b = \mu'_{R_H}$ for this flat-band condition. As the surface potential well gets larger (i.e., V_s becomes large and surface band-bending exists), α approaches zero. In this situation, $(\mu'/\mu_b)|_{\alpha \to 0} = 2\alpha/\pi^{1/2}$ and $(\mu'/\mu_b)_{R_H}|_{\to 0} = \alpha$. Thus, even under this extreme condition, the mobilities differ by only some 12%.

Measurements of resistivity and Hall coefficient are necessary for determining of both the mobility and carrier concentration in thin films. However, caution must be exercised since errors in measurements can arise from specimen contours; electrode size, geometry, and positions; electrode symmetry; and spatial and thickness inhomogeneities. Weider [43] reviewed these sources of error for galvanomagnetic measurements and presented a useful analysis that can be used to either avoid these errors or correct for them.

5. <u>Experimental Results</u>

The semiconductor surface and its relationship to the electrical characteristics of the thin film have been the subject of many investigations. In general, such experiments are tedious and sometimes difficult to reproduce, especially if the films are polycrystalline. Although the thin films for such

studies have been grown on a variety of substrates by all possible deposition techniques, epitaxial growth methods have been most successful for isolating the effects of surfaces because of fewer defect associated problems. With the improvements in deposition control, monitoring, and measurement for thin-film processing, it can now be expected that the semiconductor surface will be analyzed more accurately and rigorously. Among the more interesting and important are the recent advances in molecular beam epitaxy (MBE) [44-46]. This technique has the potential to make significant contributions to the knowledge of surface-related properties of films since it produces very thin films, growing them a single layer at a time, with accurate and reproducible electrical, structural, and physical properties. It is <u>not</u> the purpose of this section to present an exhaustive compendium of surface related data, but rather to present results which verify or demonstrate the thin-film surface analyses and modeling discussed previously.

a. Surface Scattering

Evidence illustrating the effects of surface scattering upon the electrical properties of semiconductor and metal thin films is well-represented in the literature [1, 36-43, 47-72]. The thickness dependence of the mobility (and resistivity) predicted by Eqs. 3.21, 3.22, and 3.29 has been experimentally demonstrated for Ge [40, 47-50], Si [36, 51-54], PbSe [38, 55], PbTe [39, 56], PbS [39, 57], CdS [29, 30, 58-63], CdSe [64], CdTe [65], GaAs [66, 67], and several other semiconductor thin films [68-72]. For the first example, Fig. 3-14 shows the dependence of the inverse film mobility upon thickness for CdS films deposited at two different substrate temperatures [29]. In each case the mobility approaches a constant value (μ_b in Eqs. 3.22 and 3.29), while the mobility decreases significantly for films less than 1 μm in thickness. The solid lines represent the model of Eq. 3.29 with λ = 1100 $\overset{\circ}{A}$. For these films, the scattering was found to be almost entirely diffuse by comparison to the relationship given by Eq. 3.30. Fig. 3-15 shows that these data lie very near the (p+q) = 0 line [29].

The predicted dependence of the Hall coefficient (and carrier concentration) given by Eq. 3.45 has been verified for these CdS films. Fig. 3-16 presents these data for a number of substrate temperatures [30]. The Hall coefficient for each case approaches a constant value for thicker fims, with a relative increase for each substrate temperature observed for thinner films. By fitting these data in the vicinity of the knees of each of the curves in Fig. 3-16, the dependence of the surface scattering length upon substrate temperature has been evaluated (Fig. 3-17) [30]. The magnitude of λ varies from about 680 $\overset{o}{A}$ at low substrate temperatures to 1200 $\overset{o}{A}$ at higher ones. The more or less constant λ at the extreme values is expected since the carrier concentrations become constant in these ranges.

Effects of band-bending upon the electrical properties of semiconductor films have been investigated by controlling the gaseous environment to which the film is exposed, thereby providing accumulation or depletion to some degree. Earlier studies exposed film surfaces to a variety of gases (e.g., O_2, H_2, H_2S) and correlated the changes in conductivity with the partial pressure of the gases [73-78]. These investigations are summarized in two good reviews [73, 74] and will not be covered in detail here. In some cases, the electrical properties were reversible with gas exposure and cycling, which led to the development of solid-state gas sensors [79].

b. Field Effect Experiments

Waxman et al. [32] demonstrated the effects of surface states on the mobility of CdS thin films by providing a solid interface at the CdS surface to control the band-bending. In these experiments the band-bending was varied by using a field-effect structure--similar to that of a field-effect transistor--which had a metal field plate electrode deposited on the top insulator. A controlled bias, V_p, could be applied to the surface of the CdS, allowing observation of the relationship between change in band-bending and the measured Hall mobility. Fig. 3-18 shows the variation in Hall mobility with field-plate potential using a CaF_2 insulator on the CdS film [78]. The CaF_2 tends to cause a depletion region at the surface of the CdS. The mobility decreases monotonically as a function of V_p, as predicted by Eq. 3.44, for

increasing V_s (i.e., positive and increasing V_p). Fig. 3-19 presents analogous data for a SiO-CdS structure for which the SiO tends to cause an accumulation layer in the CdS with no applied bias [78]. For V_p < 6V, μ and the resistance are about constant, demonstrating for the existence of surface states. The charge induced into these states is immobile and the surface potential, V_s, is expected to be constant and independent of V_p; therefore, the mobility should be constant as predicted by Eq. 3.43. Above this 6V region the ratio of free to trapped charge increases and the surface mobility (and conductance) likewise increases. At very high V_p the mobility begins to decrease due to surface scattering.

Several other investigators used field effect structures to study the mobility of semiconductor thin-film surfaces [80-83]. Van Heek [80] showed that even a relatively small number of surface states can have a strong influence on mobilities and carrier concentrations of CdSe thin films, consistent with the models discussed in the previous sections. Ipri used the field effect technique to determine the electrical properties of silicon films grown epitaxially on sapphire [81]. Ipri varied the plate potential from negative through positive values, causing the silicon film surface to change from depletion to flat-based to accumulation. The effect on mobility is shown in Fig. 3-20. A maximum is observed in this characteristic curve for light accumulation, indicating a higher mobility near the surface, and the mobility decreases at higher V_p due to surface scattering. This result is similar to that observed by Waxman (Fig. 3-19) for the CdS films [32]. For the silicon case, however, the mobility decreases rapidly as the depletion region widens, again indicating a mobility gradient through the film, consistent with the Anderson model (Fig. 3-10). For more negative values of V_p, the mobility becomes constant, since the inversion condition is reached and the depletion width becomes about constant. Ipri also provides a theoretical analysis with this field-effect technique to determine actual surface concentrations and the gradients of the mobilities and carrier concentrations through the z or thickness direction of the film.

3.3 TRANSPORT IN POLYCRYSTALLINE FILMS

Perfect epitaxial thin films are not the usual case encountered in thin-film technology. Even epitaxial films commonly contain point defects and dislocations that can affect carrier transport. Most often, the situation is even more complicated. For reasons of economics, large-scale deployment, or necessity film growth is confined largely to different material, noncrystalline substrates (e.g., on metal films for electrical contact), and the resulting semiconductor thin films are usually polycrystalline. Therefore, the conduction mechanism is dominated by the inherent intercrystalline boundaries rather than the intracrystalline characteristics.

This section focuses on the relationships between the defects found in polycrystalline semiconductor films and the resulting electrical characteristics. The intercrystalline boundaries, or grain boundaries, are emphasized because they are the most dominant, least controllable, and perhaps the most misunderstood problems for the thin-film investigator. Attempts at producing generalized models that explain for the transport behavior due to grain boundaries have been unsuccessful. Although they do provide insight to the general physics involved, the techniques must be understood as modeling methods, which can predict behavior accurately only under a specific controlled set of experimental and material circumstances. It should be expected, for instance, that grain boundaries in compound semiconductor films are quite different for carrier transport than those in elemental semiconductors. Boundaries for larger crystallite films differ from those fore small-grained ones. Also, the physical, structural, electrical, and optical characteristics of grain boundary regions are drastically altered by exposure to impurities, diffusion, and field effects. Thus, care must be taken in applying or interpreting of any general analysis of grain boundary phenomena. Several models of polycrystalline semiconductor thin films are summarized here. Some expansions and explanations of the basic physical processes are included. Carrier transport associated with dislocations, stacking faults, mechanical stress, and defect types are discussed. Data representative of these effects are presented for elemental and compound semiconductors. Finally, the integration of surface scattering effects with defect dominated phenomena is discussed.

1. Initial Representation – Boundary Scattering

Fig. 3-21 presents a conceptual cross section of thin film having a cylindrical grain structure. This geometry has been observed in many thin-film systems and is effectively represented by the scanning electron micrograph of the cross section of a polysilicon film shown in Fig. 3-22 [84, 85]. It should be added that, in some film growth cases, the columnar growth can be interrupted and grain boundaries can occur along the z-direction of the film.

A simple approach is to consider the grain boundaries represented in Fig. 3-21 as having the major effect of controlling the carrier transport from grain to grain. Thus, the carriers collide at the boundaries and, in the steady state, have an effective mean free path, λ_g, and a mean relaxation time, τ_g. The mobility associated with this mechanism can be expressed

$$\mu_g = q\tau_g/m^*$$

$$= (q\lambda_g)/m^*v$$

[3.49]

where v is the mean thermal carrier velocity. Anderson [6] calculated this effective mobility for two cases. First, for a <u>degenerate semiconductor</u> (using Fermi-Dirac statistics),

$$\mu_g = \frac{q\lambda_g}{h} (3\pi^2 n)^{-1/3} \left(\frac{m_d^*}{m_i^*}\right)^{1/2}$$

[3.50]

where n is the free carrier density, m_d^* is the density of states effective mass and m_i^*, the inertial or conductivity mass of the carrier. Second, for a <u>nondegenerate</u> case (using Boltzmann statistics),

$$\mu_g = q\lambda_g \left(\frac{9\pi}{8} m_i^* kT\right)^{-1/2}$$

[3.51]

The exact temperature sensitivities of Eqs. 3.50 and 3.51 will depend upon the semiconductor involved. If it has a low bandgap, E_g is more affected by temperature changes (i.e., E_g becomes more significant), and m_i^* and m_d^* are especially temperature sensitive. Thus the mobility of a nondegenerate semiconductor is more likely to deviate from the $T^{-1/2}$ dependence of Eq. 3.51 for the low bandgap case. On the other hand, the temperature sensitivity of the degenerate semiconductor mobility (Eq. 3.50) depends upon the ratio of m_d^* to m_i^*. Since the temperature dependence of each of these masses is approximately the same, only small variations in μ_g with T are expected. For either case, the masses are relatively temperature independent for materials with larger bandgaps. Thus μ_g follows the $T^{-1/2}$ dependence for the nondegenerate semiconductor, and μ_g is relatively temperature independent for the degenerate case. Measurements supporting this simple analysis are scant in the literature. In his work with PbTe, Egerton [86] reported the expected behavior for degenerate n-type films grown on mica. The mobility demonstrated was both reduced from the single crystal value as predicted by Eq. 3.50 and approximately independent of temperature as expected for this low bandgap semiconductor. This situation is somewhat special since the boundary scattering model requires that the potential barriers at the grain boundaries be relatively small. The Egerton films fulfilled this condition since the grain sizes were relatively small and the material permittivity was high, allowing little band-bending to develop at the boundaries. This is, of course, similar to the surface scattering situation presented in Fig. 3-8 [34].

2. Grain Boundary Potential Barrier Models: Compound Semiconductors

Most analysis and modeling techniques correlating the transport properties with the polycrystallinity of thin films are based upon the consideration that the grain boundaries have an inherent space charge region due to the interface. Band-bending occurs and potential barriers to the charge transport result. This situation is represented schematically for an n-type semiconductor in Fig. 3-23. The transport properties of both metals and semiconductors were scrutinized using this rather simple description, and the reduced mobility and conductivity of the materials as compared to single

crystal analogues were predicted. The major contributions to compound semiconductor thin films using this approach are now considered.

a. The Models

Transport Mechanisms

One of the earliest models accounting for the conductivity in polycrystalline semiconductor films was that of Volger [87]. Volger based his model on that of an inhomogeneous conductor consisting of series-connected, separately homogeneous (electrically and structurally) domains of high conductivity and very low conductivity in which no space charge regions exist. The width of the low conductivity domains (i.e., the grain boundary regions) is negligible with respect to the high conductivity regions or grains. Thus, the situation simulates a polycrystalline semiconductor in which ohmic transport of the carriers dominates. Defining ℓ_1 as the grain size and ℓ_2 as the boundary width, Volger derived the expression for the Hall coefficient

$$R_H = R_{H1} + c(\ell_2/\ell_1)^2 R_{H2} \qquad [3.52]$$

where c is an unspecified constant and R_{H1} and R_{H2} are the Hall coefficients in the grain and boundary regions, respectively. He related this to the mobility, showing that

$$\mu_g = \mu_1 \left\{ [1 + (\ell_2/\ell_1) \exp(q\phi_b/kT)]^{-1} + (\ell_2/\ell_1) \right\} \qquad [3.53]$$

where μ_1 is the bulk grain mobility and ϕ_b is a barrier potential relating to the concentrations in the grain and boundary domains.

This analysis was followed by the perhaps most cited, theoretical analysis of transport mechanisms in polycrystalline thin films--that of Petritz [88]. Although his initial emphasis was directed toward the theory of photoconductivity in polycrystalline compound semiconductors, his straightforward modeling of the conductivity is applicable to a wider range of

cases. The model differs slightly from Volger's and is based upon a polycrystalline semiconductor in which thermionic emission of carriers is prevalent.

Petritz dealt with parameters as averages of many grains. Thus the analysis considered initially a single grain and a single boundary or barrier. The total resistivity of this case is written

$$\rho_g = \rho_1 + \rho_2 \qquad\qquad [3.54]$$

where the subscripts signify grain or crystallite (1) and boundary (2) regions, respectively. It was assumed that for the usual case, $\rho_2 \gg \rho_1$; then the current-voltage relationship for the barrier could be expressed (analogous to simple diode theory) as

$$j = Mn_1 \exp(-q\phi_b/kT)[\exp(-qV_B/kT) - 1] \qquad\qquad [3.55]$$

where j is the current density; n_1 is the mean majority carrier density in the grains; ϕ_b is the potential height of the barriers; V_B is the voltage drop across the barrier; and M is a factor that is barrier dependent but independent of ϕ_b. If the film has many barriers (i.e., small grain sizes) the voltage drop across any one is small as compared to kT/q, and Eq. 3.55 may be written

$$j = Mn \exp(-q\phi_b/kT)(qV_B/kT) \qquad\qquad [3.56]$$

If V is the total voltage drop across the film and there are n_c crystallites or grains per unit length along the film of length L, then

$$j = [q\mu_0 n \exp(-q\phi_b/kT)]\mathcal{E} \qquad\qquad [3.57]$$

where $\mu_0 = M/n_c kT$; $\mathcal{E}$ is the electric field; and the quantity in the brackets is the conductivity. Petritz observed that the exponential term in Eq. 3.57 provided the essential characterization of the barrier. Petritz assumed that since $\rho_1 \ll \rho_2$, the carrier concentration is not reduced by the exponential factor, but rather all carriers take part in the conduction process but with

reduced mobility; that is,

$$\mu_g = \mu_0 \, \exp(-q\phi_b/kT) \qquad\qquad [3.58]$$

Eq. 3.58 can be generalized to include the case in which scattering within the grain can be significant [7]. To accomplish this, $\mu_0 = \mu_b(T)$, the bulk or single crystalline value. Therefore,

$$\mu_g = \mu_b \, \exp(-q\phi_b/kT) \qquad\qquad [3.59]$$

It has been proposed that more correctly $\mu_b = C\mu_{cryst}$ where C is a constant and μ_{cryst} is the perfect crystalline value of mobility [29]. Thus μ_b is the bulk-representation of the grain or crystallite mobility, which may include inherent defects or impurities.

Berger [62, 87] showed that the Hall coefficient and the carrier concentrations also exhibit exponential dependences, similar to that of Eq. 3.59. Berger showed that

$$R_H = R_0 \, \exp(-E_n/kT) \qquad\qquad [3.60]$$

and the magnitude of the activation energy, E_n, depends upon the relative concentrations in the grain and the boundary region. Mankarious [90] and others [91-94] extended this work by observing that the conductivity term in Eq. 3.57 should be written more generally as

$$\sigma_g \sim \exp(-E_\sigma/kT) \qquad\qquad [3.61]$$

where E_σ is the conductivity activation energy. Since $\sigma = ne\mu_n$ (for an n-type semiconductor) or $\sigma = pe\mu_p$ (for a p-type one), the carrier concentrations can be expressed by similar relationships, consistent with Berger's observation. Therefore,

$$n \sim \exp(-E_n/kT) \qquad\qquad [3.62]$$
or
$$p \sim \exp(-E_p/kT) \qquad\qquad [3.63]$$

where E_n and E_p are the carrier activation energies for n- and p-type films, respectively. The relationship among the conductivity, mobility, and carrier concentrations further predicts that

$$E_\sigma \simeq E_{n(or\ p)} + q\phi_b \qquad [3.64]$$

Therefore, for the special case proposed by Petritz ($\rho_1 \ll \rho_2$), the mobility activation energy is identical to the conductivity activation energy, and R_H is constant.

Berger expanded the Petritz model further, using a more general yet precise representation of the polycrystalline film (Fig. 3-24). The grain size and resistivity are given by ℓ_1 and ρ_1 and the boundary parameters by ℓ_2 and ρ_2. Thus the effective resistivity is written

$$\rho_g = \rho_1 + (\ell_2/\ell_1)\rho_2 \qquad [3.65]$$

Berger derived an expression for the effective mobility based upon this model,

$$\mu_g = \mu_1/[1 + c\ \exp(\ E/kT)] \qquad [3.66]$$

where $c = (\ell_2/\ell_1)(n_{01}/n_{02})$, and n_{01} and n_{02} are the characteristic carrier concentrations at infinite temperature defined from $n_{1\ (or\ 2)} = n_{01\ (or\ 02)}$ $\exp(-E_{1(or\ 2)}/kT)$ (see Eq. 3.62), in the grain and grain boundary regions, respectively. μ_1 is the mobility in the grain. The second term in the denominator of Eq. 3.66 usually dominates, and the mobility term is often written in a form similar to that derived by Petritz:

$$\mu_g = \mu_1[(\ell_1/\ell_2)(n_{02}/n_{01})\ \exp(-\Delta E/kT)] \qquad [3.67]$$

Comparison of Eqs. 3.58 and 3.67 leads to two interpretations of the activation energies and the magnitudes of μ_0 and μ_1. Kassing and Bax [95] demonstrated that in the limiting (or comparative) cases for these two models,

$$\mu_o \simeq \mu_1 (\ell_1/\ell_2)(n_{02}/n_{01}) \tag{3.68}$$

and μ_1 is the mobility of the bulk single crystal. In the special case for which the grain size is large enough (i.e., greater than the mean free path of the carriers), scattering within the grain becomes important. Therefore, Eq. 3.68 reduces to $\mu_o \simeq \mu_1 = \mu_b$, and Eq. 3.59 holds.

Barrier Heights

The barrier heights (or mobility activation energies) used in the previous models can be compared. For both the Volger and Petritz models [87, 88],

$$q\phi_b = kT \ln(n_1/n_2) \tag{3.69}$$

where n_1 and n_2 are the carrier densities in the grain and boundary regions, respectively. By comparison, Berger found that

$$\Delta E = E_2 - E_1 \tag{3.70}$$

where this difference is determined by the difference in the ratios:

$$\Delta E = \ln\left(\frac{N_A}{N_D}\bigg|_{\text{grain boundary}} - \frac{N_A}{N_D}\bigg|_{\text{grain}}\right) \tag{3.71}$$

and N_A, N_D are the acceptor and donor densities.

Since in a more general sense than assumed by Petritz, $n_1 = n_{01} \exp(-E_1/kT)$ and $n_2 = n_{02} \exp(-E_2/kT)$, Eq. 3.69 becomes

$$q\phi = kT \ln(n_{01}/n_{02}) + (E_2 - E_1) \tag{3.72}$$

Substituting this into Eq. 3.58 shows that

$$\mu_g \sim (n_{01}/n_{02}) \exp[-(E_1-E_2)/kT] \qquad\qquad [3.73]$$

which is consistent with the Berger representation.

Other Analytical Approaches

Several other models for the conductivity in compound semiconductor films investigated produced results similar to those of Volger, Petritz, and Berger [96-104]. Among them are several more complicated approaches based upon electrical component modeling of the polycrystalline film. An example is the methodology of Kuznicki, whose structural model and electrical equivalents are shown in Fig. 3-25. The model was used to verify numerically the static electrical characteristics of CdSe films. The qualitative resemblance of the analytical and experimental characteristics is shown in Fig. 3-26.

b. The Results

Experimental verifications of the models discussed in the previous section, especially the predicted reduced mobility and its exponential dependence upon inverse temperature, have appeared throughout the literature. Compound semiconductors reported to follow these models include: CdS [29, 32, 61, 103-115]; CdSe [64, 115, 116]; CdTe [118-121]; PbS [38, 122]; PbSe [38, 47, 52, 122, 125]; PbTe [38, 55, 126-128]; InAs [129]; InP [92, 130-133]; InSb [134-136]; Cu_xS [137-140]; SnO_x [141]; SnTe [39, 142]; GaAs [143-147]; GaP [148]; $CuInS_2$ [89, 149]; $CuInSe_2$ [90, 149-151]; $CuInTe_2$ [91].

Typical results are presented in Fig. 3-27 for CdS thin films deposited by resistive heating onto glass substrates. Values for $q\phi$ ranging from 0.05 to 0.50 eV have been reported for CdS films, and this activation energy can be seen from Fig. 3-28 for CdS and Fig. 3-29 for $CuInSe_2$ to be a function of the deposition conditions. The relationships among the mobility, conductivity, and carrier concentration activation energies are illustrated in Figs. 3-30 and 3-31. Fig. 3-30 shows the data of Mankarious for CdS thin films, from

which $E_\sigma(0.44eV) = E_n(0.33eV) + q\phi_b(0.11eV)$ as predicted by Eq. 3.64. This relationship has also been demonstrated for InP [92], CuInS$_2$ [89], CuInSe$_2$ [90], and CuInTe$_2$ (which is shown in Fig. 3-31) [91].

Expected deviations from the exponential temperature dependence of electrical properties reported include nonuniform grain sizes [61, 152], concentration variations [153], and lattice and impurity scattering [39, 50, 88, 154]. For high temperatures Mankarious [88] demonstrated that the mobility of CdS films is dominated by both the impurity (see Eq. 3.5) and lattice (see Eq. 3.4) scattering (Fig. 3-32).

3. Transport Properties: Elemental Semiconductors

The transport properties of elemental semiconductor films (silicon and germanium) are considered separately from the previous section mainly because these semiconductors develop their extrinsic characteristics through the incorporation of impurity atoms rather than through compositional or stoichiometric effects. Two models have been used to interpret the electrical properties of elemental thin-film semiconductors:

- Segregation Model--in which the impurity atoms segregate to the grain boundaries and are electrically inactive [155, 156]. The basic limitation of this model is that it fails to represent the temperature dependence of the resistivity. In addition, this model predicts a negative temperature coefficient of resistance which has not been experimentally demonstrable.

- Grain Boundary Trapping Model--in which there is a large concentration of active trapping sites at the grain boundary which, in turn, captures free carriers [157-159]. As a result, these charge states at the grain boundaries become potential barriers as shown in Fig. 3-23. Similar to the Petritz and Berger models of the previous section, these barriers limit the transport of carriers between grains and the mechanism is dominated primarily by thermionic emission.

The evolution of the potential at the grain boundary is an interesting phenomenon. In general, such grain boundary barriers are formed when the boundary region has a lower electrochemical potential for minority carriers than the grains, providing for the inflow of electrons or holes into the region. A space charge layer is thereby created that inhibits further flow of carriers. If barriers are formed in both n- and p-majority-carrier-types of a semiconductor, the Fermi level is located somewhere near the center of the bandgap. Such is the case for silicon [156, 157]. However, the Fermi level is sometimes not in the midgap vicinity, and potential barriers can be created in only one majority carrier type of the semiconductor. Such is the case with germanium, in which grain boundary potential barriers form only in n-type material [161-163].

a. Grain Boundary Trapping Model

Seto [160] developed the most comprehensive theoretical analysis of grain boundary trapping based upon the physical, charge, and energy band structures shown in Fig. 3-33. Seto made the following assumptions: (1) grains are identical, with cross section σ; (2) only one type of impurity atom is present (monovalent trapping) and is uniformly distributed with a concentration N/cm^3; (3) the grain boundary thickness is negligible and contains Q_t/cm^2 traps located at energy E_t with respect to E_i; (4) the traps are initially neutral and become charged by trapping a free carrier. Thus all the mobile carriers which are in a region $\ell/2 - \delta$ (see Fig. 3-33) from the grain boundary are trapped, resulting in a space charge region. Seto neglected the mobile carriers in this region.

The one-dimensional Poisson equation for this region, for a p-type film, is

$$\frac{d^2V}{dx^2} = \frac{q}{\epsilon} N \qquad \delta < |x| < \ell/2 \qquad\qquad [3.74]$$

The solution of this equation yields for $\delta < |x| < \ell/2$,

$$V(x) = (qN/2\epsilon)(x-\delta)^2 + V_{vo} \qquad [3.75]$$

where V_{vo} is the potential of the valence band edge (Fig. 3-33).

Two possible conditions exist for the trap densities depending upon the doping concentrations: $Q_t > \ell N$ or $Q_t < \ell N$. For the former case, the grain is completely depleted of carriers and the traps are partially filled. Thus $\delta = 0$, and Eq. 3.75 yields the potential. Therefore, since $p(x) = N_v \exp[-(qV(x)-E_f)/kT]$, the average concentration, through integration over the region $-\ell/2 < x < \ell/2$, becomes

$$p_{av} = \left(\frac{N_v}{q\ell}\right)\left(\frac{2\pi\epsilon kT}{N}\right)^{1/2} \exp\left(\frac{E_b + E_f}{kT}\right) \mathrm{erf}\left[\frac{q\ell}{2}\left(\frac{N}{2\epsilon kT}\right)^{1/2}\right] \qquad [3.76]$$

where n_i is the intrinsic concentration of the single crystal and

$$E_b = q\phi_b$$
$$\qquad [3.77]$$
$$\quad = q(q\ell^2 N/8\epsilon)$$

For $Q_t < \ell N$, only <u>part</u> of the crystallite is depleted of carriers and $\delta > 0$. In this case,

$$p_{av} = p_b\left[(1 - \frac{Q_t}{\ell N}) + \frac{1}{q\ell}(\frac{2\pi\epsilon kT}{N})^{1/2}\right]\mathrm{erf}[\frac{qQ_t}{2}(2\epsilon kTN)^{-1/2}] \qquad [3.78]$$

where $p_b = N_v \exp[-(E_{vo}-E_f)/kT]$ as in similarly doped single crystal silicon.

It should be noted that the net effect of doping concentration and trap density is to vary the barrier height, $q\phi_b$. This behavior is shown for an arbitrary case in Fig. 3-34. The variation results from the dipole layer, which is created by impurities and filling of the traps. As the impurity concentration increases so does the strength of the dipole region. Once all the traps are filled, however, both the width of the dipole layer and the magnitude of $q\phi_b$ decrease, while the total charge in the region remains constant.

The conductivity can now be determined using thermionic emission current similar to that of Petritz [86]; that is,

$$j = q P_{av} \left(\frac{kT}{2\pi m^*} \right)^{1/2} \exp\left(-\frac{q\phi_b}{kT}\right) \left[\exp\left(\frac{qV_B}{kT}\right) - 1\right] \qquad [3.79]$$

where V_B is the voltage applied across the grain boundary. For small V_B ($\ll kT/q$), the conductivity is calculated from Eq. 3.79:

$$\sigma_g = q^2 \ell\, P_{av} (2\pi m^* kT)^{-1/2} \exp(-q\phi_b/kT) \qquad [3.80]$$

Thus two solutions are obtainable, corresponding to the doping density regimes. Substituting Eqs. 3.76 and 3.78 into Eq. 3.80 yields

$$\sigma_g \sim \exp[-(E_g/2 - E_f)/kT] \qquad \ell N < Q_t \qquad [3.81]$$

and

$$\sigma_g \sim T^{-1/2} \exp(-E_b/kT) \qquad \ell N > Q_t \qquad [3.82]$$

In either case, the effective mobility from Eq. 3.80 is

$$\mu_g = q\ell (2\pi m^* kT)^{-1/2} \exp(-q\phi_b/kT) \qquad [3.83]$$

In the case of polycrystalline silicon, Seto showed experimentally the validity of Eqs. 3.81 and 3.82 by plotting the logarithm of the resistivity vs. $(kT)^{-1}$ [158]. These data gave the predicted straight line dependence with slope $E_g/2 - E_f$ for $\ell N < Q_t$ and E_b for $\ell N > Q_t$. Fig. 3-35 presents the data for the mobility of Seto's polycrystalline Si films as a function of inverse temperature. As expected, the dependence shows a straight line with a negative slope ($= q\phi_b$) and a deviation when $q\phi_b < kT$. Seto's model also accounts for the Hall mobility, carrier concentration, and resistivity dependencies upon doping concentration for polycrystalline films (Figs. 3-36, 3.37, and 3.38). In each, the solid line indicates the model with a very good correspondence observable.

b. Model Limitations and Refinements

Seto [159, 160] and others [164-166] noted several basic limitations of the grain boundary trapping model, including:

- Grain Resistivity—In Seto's model, the bulk resistivity of the grain was assumed to be insignificant with respect to the resistivity of the boundary region. If the grain size is large and the doping relatively high, the grain resistivity must be considered. Kamins demonstrated this effect with polysilicon doped above $7 \times 10^{18}/cm^3$ [157, 167, 168].

- Discrete vs. Distributed Energy States—Rather than the discrete or fixed energy assumed in the model, it is possible that the trapping states at the grain boundaries are distributed over some energy range, as has been reported for the surface states of the free silicon surface [169] or the Si/SiO_x interface [170]. This affects directly the activation energy, mobility, and carrier concentration, especially if $N \lesssim Q_t/\ell$ (see Fig. 3-34).

- Depletion Region Free-Carrier Density—In some cases (e.g., large-grain polysilicon), the carrier concentration in the space-charge layer can become appreciable, leading to inaccurate values of the barrier heights calculated by the Seto model. Since μ_g depends exponentially upon $q\phi_b$, significant variances can result. The carrier concentration is more sensitive to the shape of the barrier in the depletion region and is less affected by changes in the magnitude of the barrier height.

- Energy Level of Interface (Trapping) States—The Seto model predicts (depending upon impurity type) that the trapping states are located in either the upper or lower half of the bandgap—excluding the midgap position [164, 166].

- Trap Population--A major assumption of the Seto model, that available grain boundary traps in the bandgap are always filled, is not universally true.

Several modifications to the Seto model have been proposed by Baccarani et al. [164]. Directed toward clarifying the model for the intermediate range of impurity concentrations, their work considers two trapping cases: (1) monovalent trapping states; and (2) continuous distribution of trapping states within the bandgap.

Monovalent Trapping States at the Grain Boundary

For the case of monovalent trapping states at the grain boundary, Baccarani et al. assume the existence of N_t acceptor states (using an n-type semiconductor analogous to the Seto p-type situation) with energy E_t with respect to E_i at the interface. For a given set of ℓ, N_t, and E_t there is an impurity concentration, N_D^*, such that if N_D is less than N_D^*, the grains are entirely depleted. Two possible impurity conditions exist:

(i) For $N_D < N_D^*$, the energy barrier is given by [164]

$$E_b = q^2 \ell^2 N_D / 8\epsilon \tag{3.84}$$

and the conductivity becomes

$$\sigma_g = \frac{q^2 \ell^2 N_c N_D v}{2kT(N_t - \ell N_D)} \exp(-E_a/kT) \tag{3.85}$$

where $v = (kT/2\pi m^*)^{1/2}$ and the activation energy is given by

$$E_a = (E_g/2) - E_t \tag{3.86}$$

(ii) For $N_D > N_D^*$, the grains are partially depleted and the barrier height is [164]

$$E_b = E_f - E_i + kT \ln[2(qN_t/(8\epsilon N_D E_b)^{1/2} - 1)] \hspace{2cm} [3.87]$$

which must be solved iteratively. Two solutions for the conductivity can be calculated corresponding to two energy regions.

$$\sigma_g = (q^2 \ell N_c^2 v n_o/kT) \exp(-E_a/kT) \left.\begin{array}{l} \\ \\ \end{array}\right\} E_f - E_t - E_b \gg kT \hspace{1cm} [3.88]$$

$$E_a = E_b$$

and

$$\sigma_g = q N_c^2 v (2\epsilon N_D^{-1} E_b)^{1/2} (kTN_t)^{-1} \exp(-E_a/kT) \left.\begin{array}{l} \\ \\ \end{array}\right\} E_t + E_b - E_f \gg kT \hspace{1cm} [3.89]$$

$$E_a = (E_g/2) - E_t$$

where n_o is the concentration in the neutral region neglected by the Seto treatment. The latter energy region (Eq. 3.89) also had not been covered by Seto's approach and solution.

Fig. 3-39 represents the calculated activation energy as a function of N_D for several trap densities. The grain sizes are assumed to be 0.1 μm, and the dashed line indicates the boundary between the two energy regions and their respective solutions (Eqs. 3.88 and 3.89). For lower values of N_t, an abrupt transition in E_a occurs (between $E_g/2$ and E_b) at the onset of complete depletion. However, for larger N_t, E_a becomes more continuous. For either complete or incomplete depletion, E_a approaches $(E_g/2) - E_f$ for the condition given by Eq. 3.87.

Continuous Distribution of Trapping States

For the comparative case of a continuous energy distribution of interface states, N_i (expressed in units of $cm^{-2}eV^{-1}$), acceptors are assumed to be uniformly distributed in the upper half of the bandgap and donors in the lower half. Baccarani et al. solved the charge neutrality equation for this situation to determine the effective space charge region width and the position of the Fermi level in terms of the barrier potential, doping, grain

size and interface state density. For <u>complete</u> <u>depletion</u> of the grains $(N_D < N_D^*)$ [164],

$$\sigma_g = (q^2 \ell N_c v / kT) \exp(-E_a / kT) \qquad [3.90]$$

with

$$E_a = (E_g / 2) - \ell N_D / N_i \qquad [3.91]$$

Corresponding to <u>incomplete</u> <u>depletion</u> $(N_D > N_D^*$ and the space charge region width $< \ell / 2)$ [164],

$$\sigma_g = (q^2 \ell N_c v / kT)(N_c / N_D)^{-\beta} \exp(-E_a / kT) \qquad [3.92]$$

with

$$E_a = (E_g / 2) - [(4\epsilon N_D)/(q^2 N_i)^2](\beta - 1) \qquad [3.93]$$

where $\beta = (1 + q^2 N_i^2 E_g / 4\epsilon N_D)^{-1/2}$

Fig. 3-40 shows the calculated activation energy versus N_D for the distributed interface state case with the same basic parameters used to determine Fig. 3-39, the comparable discrete situation. For smaller impurity densities, E_a approaches $E_g / 2$ and for higher impurity concentrations it is proportional to N_D^{-1}. Both these limits correspond to monovalent trapping states. However, the transition between these two limits is more extended in the present case, with the abrupt transition between complete and partial depletion always occurring, even at high N_i.

Baccarani <u>et</u> <u>al.</u> performed Hall studies on sputter-deposited polycrystalline silicon films implanted with phosphorus. Their results indicate some impurity segregation at the grain boundaries and the presence of an interface-state peak located at <u>midgap</u>. Fig. 3-41 presents their activation energy data, taken as a function of phosphorus concentration. The solid line indicates the monovalent trapping state model, fitted to the experimental data by adjusting N_t to $3.9 \times 10^{12}/cm^2$. The model based upon the continuous distribution of interface states failed to fit the experimental data.

c. Grain Boundary Potential, Concentration Problems

Three major problems associated with the quality and nature of the polycrystalline semiconductors--especially silicon--have impeded the exact interpretation of the results of transport studies. The <u>first</u> is the uncertainty in the actual, total doping of films. This is especially true of the chemical vapor deposition process, in which uniform accurate control is difficult. However, even in the case of ion-implanted films, such as those used by Baccarani <u>et al.</u> [164], the post-implantation high-temperature anneals necessary to minimize high energy damage can cause impurity diffusion, especially to grain boundary regions. The <u>second</u> problem is the uncertainty in impurity concentration, which varies with film thickness [157, 171]. The <u>third</u> problem concerns the contamination of the grain boundary by gases inherent to the film growth procedure. Although film processing techniques can minimize this risk, the large grain boundary surface-to-volume ratios in polycrystalline thin films magnify the problem.

In order to avoid such complications, Seager and Castner [165] characterized the electrical transport properties of neutron-transmutation-doped polycrystalline silicon [172]. Their samples had larger grain sizes, with a minimum 25 μm diameter. The electrical measurement techniques included four-probe and traveling-potential probe measurements carried out as close to zero-bias as possible. For very univorm controlled samples, Seager and Castner observed that the resistivity was linearly dependent upon inverse temperature--as previously observed [157-160]--below a doping level of approximately $2\times10^{15}/cm^3$ of phosphorus. The activation energy was nearly the midgap value, 0.55eV. However, above $2\times10^{15}/cm^3$ doping, deviations from linear dependence were observed (Fig. 3-42). Potential probe measurements made on these more highly doped polysilicon samples indicate that a large range of grain boundary impedances exist (i.e., a variety of grain boundary barrier heights are present).

Seager and Castner examined the mechanism for current flow in the presence of grain boundary potential barriers. The grain boundary potential was represented analytically under three different conditions for the interface or

defect state density, N_i:

- ### Energy-Independent N_i

$$q\phi_b = \Delta E_f [1 + \alpha/2\Delta E_f - (\alpha/\Delta E_f + \alpha^2/4\Delta E_f^2)^{1/2}] \qquad [3.94]$$

where, $\Delta E_f = E_{fg} - E_{fb}$, the Fermi levels in the grain and boundary regions, respectively, measured from the valence band edge; and $\alpha = 8\epsilon N_D/q^2 N_t$, with N_D the doping level and N_t the two-dimensional density of defect states.

- ### Monoenergetic N_i
In this case, a closed-form solution is not obtained, but

$$[8\epsilon N_D q\phi_b/(q^2 N_t^2)]^{1/2} = (\alpha q\phi_b)^{1/2} \qquad [3.95]$$

which can be solved using iterative techniques.

- ### Exponentially-Dependent N_i
A transcendental equation also results,

$$(8\epsilon N_D/q^2)^{1/2}(q\phi_b)^{1/2} = E_o[N_{TO} \exp(-E_{fb}/E_o)]\left\{1-\exp[(q\phi_b-\Delta E_f)/E_o]\right\} \qquad [3.96]$$

where $N_t = N_{TO} \exp(-E_{fb}/E_o)$ and N_o and E_o are adjustable parameters.

These three cases for N_i are summarized in the band diagram of Fig. 3-43, with the parameters used in Eqs. 3.94, 3.95, and 3.96 to fit the zero-bias data specified. Fig. 3-44 presents the dependence of $q\phi_b$ upon N_D for the three interface density cases, using the fitting parameters determined by Seager and Castner [165]. The exponential density-of-states model fits the data somewhat better than the single trap model and the energy independent N_i model, has the poorest agreement. These comparisons indicate that the largest grain-boundary state densities consist of $6\times10^{11}/cm^2$ available electron states located within 0.2eV of the midgap position. This is lower than the corresponding value of $3\times10^{12}/cm^2$ in the Seto and Baccarani polysilicon [160, 164], which is ascribed to the extrinsic quality (probably due to contamination) of the grain boundary states.

Seager and Castner correlated their results with the effects of doping concentrations on the electrical transport in polysilicon. The regions of interest, based upon Fig. 3-42, include:

- $N_D \leq 10^{14}/cm^3$--The majority of the barriers in the polycrystalline silicon are characterized by $q\phi_b = 0.55eV$, and the resistivity is dominated by this activation energy.

- $10^{14} < N_D < 2x10^{15}/cm^3$--A substantial number of barrier heights are less than 0.55eV, but the largest $q\phi_b$ still dominate the resistivity-temperature dependence.

- $N_D > 2x10^{15}/cm^3$--A range in barrier heights exists, and the magnitude of the resistivity activation energy depends upon the physical features of the sample and the analysis technique. A major problem of the shape of the grain boundary density of states function still exists. Seager and Castner propose that a careful (but difficult) measurement of the I-V characteristics of individual grain boundaries would provide this information.

4. Grain Boundary Measurements

Although some research has focused directly on the electrical and associated properties of individual grain boundaries [161, 173, 180], the literature-- including a detailed overview by Matare [173]--has been scant in synthesizing such data with either the modeling results or the broader application aspects of the polycrystalline films. However, it is becoming more evident that such research and correlations are now necessary, especially with the potential markets provided by the large-scale deployment of thin-film solar cells and other polycrystalline semiconductor devices [181, 182].

Cohen et al. reported on the carrier transport at twin and low-angle boundaries in MBE-produced GaAs [183]. This work is representative of the synergistic approach mentioned above. They reported the measurement, by scanning Auger spectroscopy, of the resistivity of single-grain and twin

boundaries in controlled gallium arsenide samples based upon spatially-resolved potential techniques.

In their experiment, two ohmic contacts were deposited such that a single-grain boundary was located perpendicular to these (Fig. 3-45). Auger electron spectroscopy is ordinarily used as a surface chemical analysis technique since the escape depths of the analyzed Auger electrons usually are less than 10Å [184]. However, Cohen et al. utilized this surface constraint along with the fact that the emitted Auger electron has a characteristic energy relative to the potential of the host atom with the analyzer referenced to ground. If the sample is biased, however, the entire Auger spectrum is shifted by an energy proportional to the known bias voltage [183]. Cohen et al. applied a voltage between the two ohmic contacts and used the energy shift of the carbon Auger peak (272eV) as a spatially resolved contactless voltmeter [183]. The carbon line was chosen for its sharpness and the fact that the element occurs on any surface exposed to air.

Fig. 3-46 shows the result for a lightly doped sample and a 6V bias with a resulting 6×10^{-4} Å current. From the grounded contact, the voltage increases linearly across the sample until the vicinity of the grain boundary. In this region an observable change in slope, representative of the grain boundary resistance, is seen. Beyond this region, the slope continues to increase linearly with its original slope.

The increase in voltage at the grain boundary in Fig. 3-46 corresponds to a region more than 3 μm in width, which represents the depletion width of a diode fabricated from such lightly doped material. Cohen et al. note that the Fermi level of the GaAs is probably pinned at the grain boundary by interface states. Band-bending on both sides of the interface would result, forming a double-depletion region (shown in Fig. 3-47). When a potential is applied to the sample, the major portion appears across the depletion region at the grain boundary as long as the grain resistivity is moderate. The resistivity of the grain boundary shown in Fig. 3-46 was calculated to be 3.3×10^{-4} Ω-cm^2, which is consistent with that reported by Dapkus et al. [185].

5. Generalized Hall Parameters for Semiconductor Thin Films

Hall effect measurements are the most common technique used in determining thin-film mobility and carrier concentration. Several interpretive problems that can arise from such measurements have been discussed by Seager and Castner [165]. Recently, a phenomenological theory of the Hall effect in polycrystalline semiconductors, providing for a general and reasonable interpretation of results, was reported by Jerhot and Snejdar [186]. Their approach models the film as depicted in Fig. 3-48, which also shows that the detailed electrical equivalent circuit of the film is compatible with previous analogies [94-99]. Jerhot and Snejdar provided a complex analysis of this model, with the resultant Hall coefficient given by

$$R_{Hg} = [\sigma'(d_G + d_B)]^{-1} \left\{ R_{HBb}\,\sigma_{Bb}\frac{d_d}{d_B} B\left[\frac{d_G - d_B}{2L_{Db}d_G}\,(R_N\,\sigma_{Bb}d_B)^{-1}(J_2(V_{Db},V_{ob}))^{\mp1}1\right] + R_{B2}D \right\}$$

[3.97]

and the Hall mobility by

$$\mu_g = (d_G + d_B)^{-1} \left\{ R_{HBb}\,\sigma_{Bb}d_B\left[\frac{d_G + d_B}{2L_{DB}d_G}\,(R_n\sigma_{Bb})^{-1}\frac{1}{J_2(V_{DB},V_{oB})} + 1\right] + R_{B2}D \right\}$$

[3.98]

where the various parameters are defined in Fig. 3-48 and Table 3-1.

This generalized approach can be used to generate the analytical results presented previously [85-87, 158, 187]. Jerhot and Snejdar have shown that the proper expressions for μ_g and R_{Hg} are obtained from Eqs. 3.97 and 3.98 for the limiting cases derived by Volger, Petritz, Berger, and Seto [85-87, 158]. In line with previous discussions of the Hall effect [43, 187], they conclude from their modeling analysis that:

- In polycrystalline semiconducters, the Hall mobility measured should never be equated with the conductivity mobility [86] even if the Hall coefficient is known. Thus, the physical parameters associated with the charge transport cannot be calculated directly from μ_H measured under the condition of zero current through the Hall contacts.

- In general, a smaller value of Hall mobility is measured in polycrystalline semiconductors as a result of the smaller number of carriers that transfer charge between current contacts as compared with the potential barrier-free case. Their predicted barrier height effects on mobility and carrier concentration are shown in Fig. 3-47.

6. Minority Carrier Properties

Some attention has been given to problems and mechanisms of recombination of minority carriers at the grain boundaries of polycrystalline thin films [188-195]. Much of the effort has been devoted to understanding the processes of minority carriers at grain boundaries in order to improve thin-film device performance and lifetime. Since a major concern involves thin-film solar cells, the behavior of the minority carriers both in the dark and under illumination has been discussed.

a. Grain Boundary Model and Diffusion Potential

Card and Yang [188] systematically developed the dependence of the minority carrier lifetime, τ, on the doping concentration, grain size, and interface state density at the grain boundaries in polycrystalline silicon. Other semiconducters have been likewise characterized, using the Card and Yang approach [188-193].

Fig. 3-50 represents the band diagram of the region surrounding a grain boundary in an n-type semiconductor. For the dark case (Fig. 3-50a), the states are filled (in equilibrium) to the Fermi level, and the band bending occurs in order to preserve charge neutrality. In the usual case, the width of the grain boundary (w) is much less than the width of the depleted region (2d') thus balancing the charge

$$Q_i = Q_d \qquad\qquad\qquad [3.99]$$

where Q_i is the net negative charge contained in the interface states, and Q_d is the net positive charge in the depletion region. Letting $E_v(0) = 0$, these charge densities are expressed [188, 189]

$$Q_c = qN_d(2d)$$

$$= 8q\epsilon N_d(q\phi_b)$$

[3.100]

and

$$Q_i = qN_i(2E_f/3q - E_v/q)$$

[3.101]

where ϵ is the semiconductor permittivity; ϕ_b is the diffusion potential; N_d is the density of states (i.e., doping concentration); and N_i is the grain boundary interface state density with units $cm^{-2}eV^{-1}$. The diffusion potential, ϕ_b, can then be calculated by using these relationships in Eq. 3.99. A similar relationship can be obtained with a model for a p-type semiconductor. Fig. 3-51 shows the dark diffusion potential for p-type CuInSe$_2$ as a function of the grain boundary interface density for various carrier concentrations. The interface state densities correspond roughly to the following grain boundary types:

- $N_i > 10^{13}/cm^2$-eV High-angle grain boundaries

- $10^{11} < N_i < 10^{13}/cm^2$-eV Medium-angle grain boundaries

- $N_i < 10^{11}/cm^2$-eV Low-angle grain boundaries

For a solar cell under illumination, the interface states adjust their charge by an initial net capture of holes (n-type semiconductor) or electrons (p-type). This, in turn, reduces the diffusion potential to a value $q\phi_b'$, which is ~0.1 $q\phi_b$ and results in the maximum recombination rate. The grain boundary region under illumination is shown in Fig. 3-50b.

b. Recombination Velocity and Minority Carrier Lifetime

In the case of a solar cell material under illumination, the recombination velocity, S, of the minority carriers at the grain boundary can be estimated in a straightforward manner. The recombination current is defined [196]

$$J_r = qS_o p_o'$$
$$\simeq qS_o p_o \qquad [3.102]$$

where the subscript o indicates x=0; p_o' is the excess concentration; and p_o is the equilibrium concentration which can be expressed $p_o = p(d') \exp(q\phi_b'/kT)$ from Fig. 3-50b. If $p_o \simeq n_o$, the recombination current is given by [197]

$$J_r = (q/2) N_i \sigma v (E_{fn} - E_{fp}) \qquad [3.103]$$

where σ is the capture cross section and v is the thermal velocity of carriers. The recombination current at the edge of the depletion region has been calculated [188] as

$$J_r \simeq qSp(d') \qquad [3.104]$$

And, combining Eq. 3.104 with Eqs. 3.102 and 3.103

$$S \simeq (1/4)\, \sigma\, v\, (E_{fn} - E_{fp})N_i \exp(q\phi_b'/kT) \qquad [3.105]$$

Thus the diffusion potential, ϕ_b', enhances the recombination at the grain boundary.

The dependence of S upon $q\phi_b'$ for various N_i is presented in Fig. 3-52 for CuInSe$_2$ ($\sigma = 2 \times 10^{-15}/cm^2$, $v = 10^7 cm/s$, $E_{fn}-E_{fp} \simeq 0.5 eV$). For $N_A \simeq 10^{16}/cm^3$, $q\phi_b' \simeq 0.13 eV$. Thus for high-angle grain boundaries ($N_i > {}^{13}/cm^2-eV$), recombination velocities in excess of $10^6 cm/s$ are expected.

The minority carrier lifetime can be calculated for a film with columnar-grain geometry. In this case, the volume recombination center density is [188]

$$N_r = 4N/\ell \qquad\qquad\qquad [3.106]$$

where N is the surface density at x=d' (i.e., from examination of Eq. 3.105, S = N v or N = $(1/4)(E_{fn}-E_{fp}) N_i \exp(q\phi_b'/kT)$. Therefore,

$$N_r = (E_{fn}-E_{fp})(N_i/\ell) \exp(q\phi_b'/kT) \qquad\qquad [3.107]$$

Therefore, for a p-type semiconductor, the minority carrier lifetime is

$$\tau_n = 1/\sigma v N_r$$
$$\qquad\qquad\qquad\qquad\qquad [3.108]$$
$$= \ell \exp(-q\phi_b'/kT)/\sigma v N_i (E_{fn}-E_{fp})$$

This dependence is shown in Fig. 3-53 for $CuInSe_2$. For the high-angle-grain boundary case, with typical 10^{-4}cm grain size, the minority carrier lifetime is in the 10^{-9}-10^{-10} s range, which is more than one order of magnitude lower than that reported for the corresponding single crystal.

The validity of these calculations has been verified for the $CuInSe_2$/CdS thin-film solar cell [189, 191, 198] and by comparison to the cylindrical grain model (see Chapter 7). Rothwarf and Barnett [199] used a geometrical argument to account for grain boundary recombination. Simply, all carriers generated closer to the grain boundary than the collecting site (i.e., the junction in the case of the solar cell) are lost. A good correspondence has been demonstrated [190] between the collection efficiency evolving from the minority carrier lifetime model (Eq. 3.108) and that derived by Rothwarf and Barnett.

Leong and Yee [200] recently reported a standard photoconductance measurement for determining the intragrain recombination velocity of excess charge carriers in large grain size materials. This technique is similar to that described by Wang and Wallis [201] and simply monitors the current passing perpendicular to the grain boundary. The analysis assumes that the incident light is absorbed entirely on the surface parallel to the grain boundary but in the grain itself. Thus no excess carriers are generated in the boundary

region. Leong and Yee's analysis of the simple bicrystal case shows that:
(i) if the grain size, ℓ, is much larger than the diffusion length, L, the
excess carrier lifetime in the polycrystalline material is not distinguishable
from that in the comparable single crystal (i.e., having the same bulk and
surface proporties); and   (ii) as the intergrain recombination velocity
increases, the effective lifetime tends to saturate.

c. Minority Carrier Mobility in Polycrystalline Thin Films

Yee [202] has provided some insight into the behavior of minority carriers in
polycrystalline semiconductors. Yee used the simple model shown in Fig. 3-54,
similar to those of other investigators, in which the grain boundary is
inverted with respect to the grain majority carrier type to estimate the
minority carrier mobility. Considering the regions on each side of the grain
boundary (labeled in Fig. 3-54), the carrier concentrations can be written for
each

$$\text{Region 1:} \quad p(x) = p_{no} + A_1 \exp(-x/L_p) + A_2 \exp(x/L_p) \qquad [3.109]$$
$$p(x) = p_{no} \exp(q\psi_e/kT) \qquad x = \ell/2 - w/2$$

with boundary conditions:
$$p(x) = p_{no} \qquad x = 0$$

$$\text{Region 2:} \quad p(x) = B_1 \exp(-x/L_p) + B_2 \exp(x/L_p) + p_{no} \qquad [3.110]$$
$$p(x) = p_{no} \exp(q\psi_c/kT) \qquad x = \ell/2 + w/2$$

with boundary conditions:
$$p(x) = p_{no} \qquad x = \ell$$

where the effective quasi-Fermi levels, ψ_e and ψ_c, are defined in the band
diagram of Fig. 3-55. From Eqs. 3.108 and 3.109 and the boundary conditions,
the diffusion equations are derived:

$$J_1 = - qD_p \left. \frac{\partial p}{\partial x} \right|_{\frac{\ell}{2} - \frac{w}{2}}$$

$$= -(qD_p p_{no}/L_p)[\exp(q\psi_e/kT) - 1] \tanh(\ell/2L_p) \qquad [3.111]$$

and likewise

$$J_2 = (qD_p p_{no}/L_p)[\exp(q\psi_c/kT) - 1] \tanh(\ell/2L_p) \qquad [3.112]$$

It can be observed from Fig. 3-55 that $\psi_e = -(V - V) = V - \psi_c$. It has been previously shown that [162]

$$\exp(q\Delta V/kT) = 2[1 + \exp(qV/kT)]^{-1} \qquad [3.113]$$

Therefore, the minority carrier current can now be derived by substituting Eq. 3.113 into either Eq. 3.111 or Eq. 3.112, making use of the relationships between the quasi-Fermi levels and ΔV and V. Thus,

$$J' = (qD_p p_{no}/L_p) \tanh(qV/2kT) \tanh(\ell/2L_p) \qquad [3.114]$$

This can now be combined with the majority carrier current density derived by Seto (Eq. 3.80) to give the total current. Assuming $qV/kT \ll 1$,

$$J = n_{av} q \mathcal{E}[q\ell/(2\pi m^*kT)^{1/2} \exp(-q\phi_b/kT)]$$
$$+ \bar{p}_n q \mathcal{E}[(\alpha\ell/2L_p) \mu \tanh(\ell/2L_p)] \qquad [3.115]$$

where $\bar{p}_n = (1/\ell) \int_0^\ell p(x)dx$, $\alpha = p_{no}/\bar{p}$ and μ is the minority carrier mobility due to bulk and impurity contributions (i.e., $\mu^{-1} = \mu_b^{-1} + \mu_i^{-1}$). But, since [194, 195]

$$J = qN_a \mu_n \mathcal{E} + q\bar{p}_n \mu_n \mathcal{E} \qquad [3.116]$$

the mobility can be obtained using Eqs. 3.115 and 3.116:

$$\mu_n = [q\ell/2\pi m^*kT)^{1/2}] \exp(-q\phi_b/kT) \qquad [3.117]$$

$$\mu_n = (\ell/2L_p) \mu \tanh(\ell/2L_p) \qquad [3.118]$$

Therefore the effective minority carrier mobility can be written [16]

$$1/\mu_e = 1/\mu + 1/\mu_n \qquad [3.119]$$

Or, solving for μ_e using Eqs. 3.118 and 3.119,

$$\mu_e = \mu[\ell/(\ell+\bar{L})]$$ [3.120]

where $\bar{L} = (2L_p)/[\alpha \tanh(\ell/2L_p)]$ and $L_p = [(kT/q)\mu\tau]^{1/2}$ in which τ is the lifetime associated with μ.

Yee extended this analysis to approximate the effects of grain size and interface (grain boundary) recombination velocity, S, on the minority carrier diffusion length. The effective diffusion length is defined

$$L_{eff} = (kT\mu_e\tau_{eff}/q)^{1/2}$$ [3.121]

where the lifetime is given by the bulk, impurity, and the interface lifetimes, τ_g'.

$$1/\tau_{eff} = 1/\tau + 1/\tau_g'$$ [3.122]

Since [186]

$$\tau_g \simeq (2\ell/3S) \exp(-q\phi_b/kT)$$ [3.123]

Combining Eqs. 3.121 and 3.123 with the expression for the recombination velocity (Eq. 3.105), the behavior of the effective diffusion length with grain size and S can be estimated. Fig. 3-56 shows such an analysis for CdTe. Yee has shown some correlation with experimental data, as presented in Fig. 3-56.

7. Composite Models and Other Effects

a. Surface and Grain Boundary Scattering

For semiconductor thin films, the carrier transport can be determined by more than one mechanism. The composite influence of the surface scattering mechanisms discussed in Section 3.1 and of the grain boundary scattering

mechanism presented in Section 3.2 have been reported in the literature [7, 29, 56]. Considering the additive nature of noninteracting scattering mechanisms, the effective film mobility may be written

$$1/\mu_f = 1/\mu_g + 1/\mu_s \qquad [3.124]$$

By incorporating Eqs. 3.28 and 3.59 into Eq. 3.124, one obtains [29]

$$\mu_f = \mu_b \exp(-q\phi_b/kT)(1+2\lambda/d)^{-1} \qquad [3.125]$$

An examination of Eq. 3.125 as a function of film thickness shows that for $d \gg \lambda$, the effect of surface scattering becomes negligible, and the mobility approaches a constant value since μ_b and μ_g do not depend upon thickness for a uniform film. However, if the thickness is of the order of magnitude of the mean surface scattering length, λ, the mobility is reduced. This composite effect was already shown in Fig. 3-14 for CdS. From these data, λ can be calculated from the thickness-dependent portions of the curves and $q\phi_b$ and μ_b can be evaluated from the constant mobility, thicker film portions.

Waxman et al. [32] developed a composite description of the behavior of polycrystalline films in their field effect experiments (Section 3-1). The effective barrier height, $q\phi'$, of the grain boundaries was calculated for a change in the carrier density and a surface depletion region of width L_c due to the band bending. Thus [32]

$$q\phi' = kT \ln[(n_1+\Delta n/L_c)/(n_2+\Delta n/L_c)] \qquad [3.126]$$

where n_1 and n_2 are the original carrier densities in the grain and grain boundary, respectively (see Eq. 3.69), and Δn is the induced concentration. From this, the change in barrier potential can be calculated to be

$$\begin{aligned}
(q\phi) &= q\phi-q\phi' \\
&= -kT \ln [(1+\alpha V_p)/(1+\beta V_p)] \qquad [3.127]
\end{aligned}$$

where

$$\alpha = \theta\epsilon_i/qd_iL_cn_1$$
$$\beta = \theta\epsilon_i/qd_iL_cn_2$$

and ϵ_i is the permittivity of the insulator in the field-effect structure; d_i is the insulator film thickness; and θ is the ratio of induced free charge to trapped charge in surface states and traps ($= q\Delta n d_i/\epsilon_i V_p$) [32]. The film mobility becomes

$$\mu_f = (C/kT)\left[\frac{1+\beta V_p}{1+\alpha V_p}\right] \exp(-q\phi/kT) \tag{3.128}$$

where $C = qv/4n_1$. The effective film mobility is predicted to rise as a function of V_p, as shown in Fig. 3-57 for various values of θ. The composite effect on inverse temperature is presented in Fig. 3-58, in which the field-injected excess charge reduces the barrier height by counteracting the depletion of charge at the grain boundary barriers.

b. Other Contributions

Dislocations

Semiconductor thin films tend to have large concentrations of defects due to the growth processes [1, 211], to lattice mismatches between layers [203-206], to differences in thermal expansion coefficients between adjacent films or substrate and film [204], and to stresses [205-208]. Surface defects on the substrate or underlayer film can also extend into subsequently deposited layers. The most common among these defects is the dislocation [211]. Overviews of the relationship between dislocations and the electrical characteristics of semiconducters are reported by Broudy [212], Read [213], and Matare [173].

Dislocations, like grain boundaries, provide charged deformation regions for carrier scattering. The mobility dependence upon temperature can be written [212]

$$1/\mu_d \simeq c_1/T^{3/2} + c_2 \, T \qquad\qquad [3.129]$$

where the first term corresponds to charged-imperfection scattering and the second term to deformation scattering of the carriers, with c_1 and c_2 temperature independent constants. Broudy [212] and Dexter and Seitz [214] derived the mobility contribution due to scattering from a uniform distribution of noncharged dislocations,

$$\mu_d = \gamma \, N_d/kT \qquad\qquad [3.130]$$

where $\gamma = (3\pi/32)(E^2 b^2 m^*/\hbar q)[(1-2\nu)/(1-\nu)]^2$; b is the dislocation Burger's vector; ν is Poisson's ratio; and E is the deformation potential. The effects of dislocations on the electrical properties become more important in thicker, single-crystal films in which grain boundary and surface scattering mechanisms do not dominate the transport.

Stacking Faults

Another intragrain defect is the stacking fault, a planar defect which results from the multiple nucleation and subsequent growth to continuity for thin films [215]. A number of investigations of the electrical properties of these defects have been published [216-222]. Brown [216] treats the scattering of plane-wave electrons from the stacking faults, which are represented as constant potential surfaces. He derives an expression for the resistivity of such defects in semiconductors as

$$\rho_{sf} = \beta [(6\pi\hbar^3)/(q^2 m^* E)] \bar{R} \qquad\qquad [3.131]$$

where β is the linear fault density; $E = \hbar^2 k^2/2m^*$, the average electron energy; and $\bar{R}$ is the average value of the reflection coefficient for all faults.

The effects of stacking faults on electronic transport have also been modeled similarly to the grain boundary that is, for a sufficiently faulted film [220]

$$\rho = \rho_b \exp(q\phi_{sf}/kT) \qquad\qquad [3.132]$$

After relating the resistivity is related to the mobility and an anisotropy in the carrier concentration is assumed, the film mobility can be expressed [220]

$$\mu_f = \mu_b[\exp(-q\phi_b/kT)(1+2\lambda/d)^{-1}]\left\{1+m\ \exp[(q\phi_{sf}-q\phi)/kT]\right\}^{-1} \qquad [3.133]$$

where m is a stacking fault count density (faults/grain) and $q\phi_{sf}$ is the stacking fault potential barrier. If m=0, Eq. 3.132 reduces to the grain boundary-dominated model given by Eq. 3.125. It should be noted that the value of m depends geometrically on the relative orientation of the stacking faults and the grain boundaries [221]. The validity of Eq. 3.132 has been demonstrated for highly-faulted CdS films that have some degree of grain misorientation. For these films, the fault densities were found to be 10^3–10^6/cm, with 5-15 faults/grain. The magnitude of $q\phi_{sf}$ was estimated to be 0.035eV. A substrate temperature dependence of the fault density was reported with highest densities, corresponding to minimum film mobilities, occurring at T_{sub}=220°C for glass substrates [221, 222].

Acknowledgements

REFERENCES

1. See Appendix I of this book for a list of relevant texts on thin-film properties.

2. J. E. Morris and T. J. Coutts, Thin Solid Films 47, 3 (1977).

3. L. I. Maissel, Handbook of Thin Film Technology, L. I. Maissel, Ed. (McGraw-Hill, N.Y.; 1970), Chapter 13.

4. See, for example, T. J. Coutts, Active and Passive Thin Film Devices, T. J. Coutts, Ed. (Academic Press, London; 1978), Chapter 3.

5. J. G. Simmons, Handbook of Thin Film Technology, L. I. Maissel, Ed. (McGraw-Hill, N.Y.; 1970), Chapter 14.

6. J. C. Anderson, Advan. Phys. 19, 311 (1970).

7. R. H. Bube, Annual Rev. of Mat. Sci. 5, 201 (1975).

8. R. F. Greene, J. Phys. Chem. Solids 14, 291 (1960).

9. R. F. Greene, Surf. Sci. 2, 101 (1964).

10. R. F. Greene, Phys. Rev. 141, 687 (1966).

11. B. Tavger and W. Kogan, Phys. Lett. 19, 353 (1965).

12. B. Tavger and E. Erukhimov, Zh. Eksper. Teor. Fiz. 51, 528 (1966).

13. B. Tavger, Phys. Stat. Solidi 22, 31 (1967).

14. See, for example, A. Many, Y. Goldstein, and N. B. Grover, Semiconductor Surfaces (North-Holland, Amsterdam; 1965), Chapter 2.

15. See, for example, J. L. Moll, Physics of Semiconductors (McGraw-Hill, N.Y.; 1964), Chapters 2 and 3.

16. A. Matthiessen, Rep. Brit. Ass. 32, 144 (1862).

17. H. F. Wolf, Semiconductors (Wiley-Interscience, N.Y.; 1971), pp. 281-283.

18. K. Fuchs, Proc. Camb. Phil. Soc. 11, 120 (1938).

19. E. H. Sondheimer, Adv. Phys. 1, 1 (1952).

20. M. S. P. Lucas, J. Appl. Phys. 36, 1632 (1965).

21. J. N. Zemel, Phys. Rev. 112, 762 (1958).

22. D. R. Frankl, *Electrical Properties of Semiconductor Surfaces* (Pergamon Press, N.Y.; 1967), pp. 42-45.

23. H. Fleitner, Phys. Stat. Solidi $\underline{1}$, 483 (1961).

24. D. S. Campbell, *The Use of Thin Films in Physical Investigations*, J. C. Anderson, Ed., (Academic Press, N.Y.; 1966), p. 299.

25. H. Mayer, *Structure and Properties of Thin Films* (J. Wiley and Sons, N.Y.; 1959), p. 225.

26. K. L. Chopra, *Thin Film Phenomena* (McGraw-Hill, N.Y.; 1969), Chapters 6 and 7.

27. A. Many, Y. Goldstein, and N. B. Grover, *Semiconductor Surfaces* (North-Holland, Amsterdam; 1965), Chapters 4 and 8.

28. F. F. Ham and D. C. Mattis, IBM J. Res. Dev. $\underline{4}$, 143 (1960).

29. L. L. Kazmerski, W. B. Berry, and C. W. Allen, J. Appl. Phys. $\underline{43}$, 3515 (1972).

30. L. L. Kazmerski, Thin Solid Films $\underline{21}$, 273 (1974).

31. H. F. Wolf, *Semiconductors* (Wiley-Interscience, N.Y.; 1971), p. 287.

32. A. Waxman, V. E. Henrich, F. V. Shallcross, H. Borkan, and P. K. Weimer, J. Appl. Phys. $\underline{36}$, 168 (1965).

33. D. W. Covington and D. C. Ray, J. Appl. Phys. $\underline{45}$, 2616 (1974).

34. A. V. Sachenko, Sov. Phys. Semicond. $\underline{11}$, 264 (1977). Also, B. D. Kandilarov and V. Detcheva, J. Phys. C-Solid State $\underline{10}$, 1703 (1977).

35. C. Juhasz, Ph.D. Thesis, Univ. of London (1968). Also, C. Juhasz and J. C. Anderson, Radio Electron. Eng. $\underline{33}$, 223 (1967).

36. R. Hezel, Siemens Forsch.--V. Entwickl $\underline{3}$, 160 (1974).

37. A. Amith, J. Phys. Chem. Solids $\underline{14}$, 271 (1960).

38. J. N. Zemel and J. O. Varela, J. Phys. Chem. Solids $\underline{14}$, 142 (1960).

39. J. N. Zemel, J. D. Jensen, and R. B. Schoolar, Phys. Rev. $\underline{140}$, A330 (1965).

40. J. N. Zemel and R. L. Petritz, J. Phys. Chem. Solids $\underline{8}$, 102 (1959).

41. R. L. Petritz, Phys. Rev. $\underline{110}$, 1254 (1958).

42. J. R. Schreiffer, Phys. Rev. $\underline{97}$, 641 (1955).

43. H. H. Weider, Thin Solid Films 31, 123 (1976).

44. A. Y. Cho and J. R. Arthur, Prog. in Solid-State Chem. 10, 157 (1975).

45. A. Y. Cho, J. Vac. Sci. Technol. 13, __ (1979).

46. J. R. Arthur, J. Vac. Sci. Technol. 13, __ (1979).

47. J. E. Davy, R. G. Turner, T. Pankey and M. D. Montgomery, Solid State Electron. 6, 205 (1963).

48. B. W. Sloope and C. O. Tiller, J. Appl. Phys. 38, 140 (1967).

49. J. E. Davy, Appl. Phys. Lett. 8, 164 (1966).

50. R. L. Ramey and W. D. McLennan, J. Appl. Phys. 38, 3491 (1967).

51. C. C. Mai, T. S. Whitehouse, R. C. Thomas, and D. R. Goldstein, J. Electrochem. Soc. 118, 331 (1971).

52. J. N. Zemel and M. Kaplit, Surface Sci. 13, 17 (1969).

53. M. Hamasaki, T. Adachi, S. Wakayama, and M. Kikuchi, Solid-State Comm. 21, 591 (1977).

54. D. J. Dumin and P. H. Robinson, J. Appl. Phys. 39, 2759 (1968).

55. M. H. Brodsky and J. N. Zemel, Phys. Rev. 155, 780 (1967).

56. W. B. Berry and T. S. Jayadevaiah, Thin Solid Films 3, 77 (1969).

57. B. V. Izvochikov and I. A. Taksami, Sov. Phys.--Semicond. 1, 985 (1968).

58. C. A. Neugebauer, J. Appl. Phys. 39, 3177 (1968).

59. R. K. Swank, Phys. Rev. 153, 844 (1967).

60. W. H. Leighton, J. Appl. Phys. 44, 5011 (1973).

61. A. Amith, J. Vac. Sci. Technol. 15, 353 (1978).

62. H. Berger, W. Kahle and G. Janiche, Phys. Stat. Solidi 28, K97 (1968).

63. K. V. Shalimova, A. F. Andrusko, V. A. Dmitriev, and L. P. Pavlov, Izv. Vozov. (Mos.) 3, 134 (1964).

64. R. W. Glew, Thin Solid Films 52, 59 (1977).

65. See, for example, F. V. Wald, Rev. Phys. Appliquee 12, 277 (1977).

66. A. C. Thorsen, H. M. Manasevit and R. H. Harada, Solid-State Electron. 17, 855 (1974).

67. G. E. Stillman and C. M. Wolf, Thin Solid Films 31, 69 (1976).

68. Y. F. Orgin, V. N. Lutskii and M. I. Elinson, Sov. Phys. JETP Lett. 3, 71 (1966).

69. Y. F. Komnik and E. I. Bukhshtab, Sov. Phys. JETP Lett. 6, 58 (1967).

70. V. P. Duggal, R. Rup, and P. Tripathi, Appl. Phys. Lett. 9, 293 (1966).

71. K. L. Chopra, L. C. Bobb, and M. H. Francombe, J. Appl. Phys. 34, 1699 (1963).

72. Y. F. Komnik, E. I. Bukhshtab, and Y. V. Nikitin, Thin Solid Films, 52, 361 (1978).

73. J. G. Dash, Films on Solid Surfaces (Academic Press, N.Y.; 1975), Chapters 1-5.

74. G. Wedler, Chemisorption (Butterworths, London; 1976).

75. S. R. Morrison, Advan. Catalysis 7, 259 (1955).

76. S. Baidyaroy and P. Mark, Surface Sci. 30, 53 (1972).

77. G. South and D. M. Hughes, Thin Solid Films 20, 135 (1974).

78. C. C. Chen, A. H. Clark, and L. L. Kazmerski, Thin Solid Films 32, L5 (1976).

79. T. J. Coutts, Active and Passive Thin Film Devices, T. J. Coutts, Ed. (Academic Press, London; 1978), Chapter 5.

80. H. F. VanHeek, Solid-State Electron. 11, 459 (1968).

81. A. C. Ipri, J. Appl. Phys. 43, 2770 (1972).

82. C. A. Neugebauer and R. E. Joynson, Abst. 13 Natl. Vac. Symp. 13, 105 (1967).

83. See, for example, J. C. Anderson, Active and Passive Thin Film Devices, T. J. Coutts, Ed. (Academic Press, London; 1978), Chapter 6.

84. T. L. Chu, J. Cryst. Growth 39, 45 (1977). Also, T. L. Chu, S. S. Chu, G. A. VanderLeen, C. J. Lin, and J. R. Boyd, Solid-State Electron. 21, 781 (1978).

85. Dieter Helmreich, Wacker Heliotronic GmbH (personal communication).

86. R. F. Egerton, Ph.D. Thesis, Univ. of London (1969).

87. J. Volger, Phys. Rev. 9, 1023 (1950).

88. R. L. Petritz, Phys. Rev. 104, 1508 (1956).

89. H. Berger, Phys. Status Solidi 1, 739 (1961).

90. R. G. Mankarious, Solid-State Electron. 7, 702 (1964).

91. L. L. Kazmerski, M. S. Ayyagari, and G. A. Sanborn, J. Appl. Phys. 46, 4685 (1975).

92. L. L. Kazmerski, M. S. Ayyagari, F. R. White, and G. A. Sanborn, J. Vac. Sci. Technol. 13, 139 (1976).

93. L. L. Kazmerski and Y. J. Juang, J. Vac. Sci. Technol. 14, 769 (1977).

94. L. L. Kazmerski, F. R. White, M. S. Ayyagari, Y. J. Juang, and R. P. Patterson, J. Vac. Sci. Technol. 14, 65 (1977).

95. R. Kassing and W. Bax, Jap. J. Appl. Phys. Suppl. 2, 801 (1974).

96. Z. T. Kuznicki, Thin Solid Films 33, 349 (1976).

97. Z. T. Kuznicki, Solid-State Electron. 19, 894 (1976).

98. V. Snejdar, Slaboproudy Ob. 31, 293 (1970).

99. J. L. Davis and R. F. Greene, Appl. Phys. Lett. 11, 37 (1967).

100. D. P. Snowden and A. M. Portis, Phys. Rev. 120, 1983 (1960).

101. R. H. Bube, Appl. Phys. Lett. 13, 136 (1968).

102. K. Lipskis, A. Sakalas and J. Viscakas, Phys. Stat. Solidi A 4, K217 (1971).

103. G. H. Blout, R. H. Bube, and A. L. Robinson, J. Appl. Phys. 41, 2190 (1970).

104. S. S. Minn, J. Res. Centre Natl. Res. Sci. Lab. Bellevue 51, 131 (1960).

105. C. Wu and R. H. Bube, J. Appl. Phys. 45, 648 (1974).

106. J. Dresner and F. V. Shallcross, Solid-State Electron. 5, 205 (1962).

107. N. F. Foster, Proc. IEEE 53, 1400 (1965).

108. F. V. Shallcross, Trans. AIME 236, 309 (1966).

109. R. W. Muller and B. G. Watkins, Proc. IEEE 52 , 425 (1964).

110. J. I. B. Wilson and J. Woods, J. Phys. Chem. Solids 34, 171 (1973).

111. D. W. Readey, J. Am. Cer. Soc. 49, 681 (1966).

112. H. G. Dill and R. Zuleeg, Solid-State Technol. 1, 27 (1964).

113. J. Dresner and F. V. Shallcross, J. Appl. Phys. 34, 2390 (1963).

114. G. Hecht, J. Herberger, and C. Weissmantel, Thin Solid Films 2, 293 (1968).

115. For a comprehensive review, see A. G. Stanley, Cadmium Sulfide (Jet Propulsion Laboratory, Publication 78-77; Pasadena, Calif.; 1978) Vols. 1 and 2.

116. K. Shimizu, Jap. J. Appl. Phys. 4, 627 (1965).

117. D. E. Brodie and J. LaCombe, Can. J. Phys. 45, 1353 (1967).

118. R. Glang, J. G. Kren and W. J. Patrik, J. Electrochem. Soc. 110, 407 (1963).

119. K. Mitchell, A. L. Fahrenbruck, and R. H. Bube, J. Vac. Sci. Technol. 12, 909 (1975).

120. F. H. Nicoll, J. Electrochem. Soc. 110, 1165 (1963).

121. D. A. Cusano, Physics and Chemistry of II-VI Compounds, M. Aven and J. S. Prener, Eds. (J. Wiley and Sons, N.Y.; 1967), Chapter 14.

122. S. Espevik, C. Wu, and R. H. Bube, J. Appl. Phys. 42, 3513 (1971).

123. L. S. Palatnik and V. K. Sorokin, Isv. Vyssh. Uch. Zaved 3, 48 (1965).

124. H. Gobrecht, K. W. Boeters, and H. J. Fleisher, Z. Physik 187, 232 (1965).

125. L. S. Palatnik and V. K. Sorokin, Sov. Phys.--Solid State 8, 869 (1966).

126. Y. Makino, Jap. J. Phys. Soc. 19, 580 (1964).

127. I. P. Voronia and S. A. Semiletov, Sov. Phys.--Solid State 6, 1494 (1964).

128. D. L. Lile and J. C. Anderson, J. Phys. D. 2, 839 (1969).

129. C. Paparoditis, J. Phys. 25, 226 (1964).

130. H. M. Manasevit and W. I. Simpson, J. Electrochem. Soc. 120, 135 (1975).

131. M. J. Tsai and R. H. Bube, J. Appl. Phys. 49, 3397 (1978).

132. J. H. McFee, B. I. Miller, and K. J. Bachmann, J. Electrochem. Soc. 124, 259 (1977).

133. K. J. Bachmann, E. Buehler, J. L. Shay, S. Wagner, and M. Bettini, J. Electrochem. Soc. 123, 109 (1976).

134. R. F. Potter and H. H. Wieder, Solid-State Electron. 7, 153 (1964).

135. C. Juhasz and J. C. Anderson, Phys. Lett. 12, 163 (1964).

136. W. J. Williamson, Solid-State Electron. 9, 213 (1966).

137. L. R. Shiozawa, F. Augustine, G. A. Sullivan, J. M. Smith, and W. R. Cook, Clevite Corp. Final Report, AF33(615)-5224 (1969).

138. S. G. Ellis, J. Appl. Phys. 38, 2906 (1967).

139. S. R. Das, P. Nath, A. Banerjee, and K. L. Chopra, Solid-State Comm. 21, 49 (1971).

140. H. Nimura, A. Atoda, and T. Nakau, Jap. J. Appl. Phys. 16, 403 (1977).

141. L. L. Kazmerski and D. M. Racine, Thin Solid Films 30, L19 (1975).

142. H. R. Riedl, R. B. Schoolar and B. Houston, Solid-State Comm. 4, 399 (1966).

143. J. R. Knight, D. Effer, and P. R. Evans, Solid-State Electron. 8, 178 (1965).

144. H. Poth, H. Bruch, M. Heyer, and P. Balk, J. Appl. Phys. 49, 285 (1978).

145. W. V. McLevige, K. V. Vaidyanathan, and B. G. Streetman, Appl. Phys. Lett. 33, 127 (1978).

146. H. Poth, Solid-State Electron. 21, 801 (1978).

147. A. E. Blakeslee and S. M. Vernon, IBM J. Res. Dev. 22, 346 (1978).

148. G. S. Kamath and D. Bowman, J. Electrochem. Soc. 114, 192 (1967).

149. L. L. Kazmerski, Ternary Compounds 1977, G. D. Holah, Ed. (Inst. of Phys. Conf. Series, London; 1977), pp. 217-228.

150. Y. Kokubun and M. Wada, Jap. J. Appl. Phys. 16, 879 (1977).

151. E. Elliott, R. D. Tomlinson, J. Parkes, and M. J. Hampshire, Thin Solid Films 20, S25 (1974).

152. See, for example, Direct Solar Energy Conversion for Terrestrial Use, K. W. Boer, Ed. (Final Report, NSF/RANN/AER72-03478 A03/FR/75) 1975.

153. G. H. Blout, R. H. Bube, and A. L. Robinson, J. Appl. Phys. 41, 2190 (1970).

154. K. Tanaka and Z. Huruhata, J. Electrochem. Soc. Jap. 37, 133 (1969).

155. M. E. Crowder and T. O. Sedgewick, J. Electrochem. Soc. 119, 1565 (1972).

156. A. L. Fripp, J. Appl. Phys. 46, 1240 (1975).

157. T. I. Kamins, J. Appl. Phys. 42, 4357 (1971).

158. P. Rai-Choudhury and P. L. Hower, J. Electrochem. Soc. 120, 1761 (1973).

159. J. Y. W. Seto, J. Electrochem. Soc. 122, 701 (1975).

160. J. Y. W. Seto, J. Appl. Phys. 46, 5247 (1975).

161. W. E. Taylor, N. H. Odell, and H. V. Fan, Phys. Rev. 88, 867 (1952).

162. R. K. Mueller, J. Appl. Phys. 32, 635 (1961).

163. R. K. Mueller, J. Appl. Phys. 32, 640 (1961).

164. G. Baccarani, B. Ricco, and G. Spandini, J. Appl. Phys. 49, 5565 (1978).

165. C. H. Seager and T. G. Castner, J. Appl. Phys. 49, 3879 (1978).

166. G. Baccarani, G. Masetti, M. Severi, and G. Spandini, Proc. 3rd. Int. Symp. Silicon Mat. Sci. and Technol., Philadelphia, 1977.

167. T. I. Kamins, IEEE Trans. Parts Hyb. Packag. VHP-10, 221 (1974).

168. J. Manoliu and T. I. Kamins, Solid-State Electron. 15, 1103 (1972).

169. See, for example, A. Many, Y. Goldstein, and N. B. Grover, Semiconductor Surfaces (North-Holland, Amsterdam; 1965), Chapters 5 and 9.

170. See, for example, S. T. Pantelides, Ed., The Physics of SiO 2 and Its Interfaces (Pergamon Press, New York; 1978).

171. C. H. Seager and T. G. Castner, Bull. Am. Phys. Soc. 22, 434 (1977).

172. J. W. Cleland, R. D. Westbrook, R. F. Wood, and R. T. Young, Proc. Natl. Wksp. on Low—Cost Polycrystalline Silicon Solar Cells, Dallas, 1977, pp. 113-117.

173. H. F. Matare, Defect Electronics in Semiconductors (Wiley—Interscience, N.Y.; 1971).

174. F. L. Vogel, W. T. Read, and L. C. Lovell, Phys. Rev. 94, 1791 (1954).

175. J. P. McKelvey, Phys. Rev. 106, 910 (1957).

176. E. I. Goldman, I. B. Gulyaev, A. G. Zhdan, V. B. Sandomirskii, and V. P. Khrenov, Sov. Phys.—Semicond. 9, 905 (1976).

177. R. A. Brown, J. Phys. F. 7, 1477 (1977).

178. P. Guyot, Phys. Stat. Solidi 38, 409 (1970).

179. G. Landwehr and P. Handler, J. Phys. Chem. Solids 23, 891 (1962).

180. Y. Makukura, J. Phys. Soc. Jap. 16, 842 (1961).

181. P. D. Maycock, Proc. 13th IEEE Photovoltaics Spec. Conf., Wash. (IEEE, N.Y.; 1978), pp. 5-8.

182. J. C. Anderson, Thin Solid Films 50, 25 (1978). Also, H. Koelmans, Thin Solid Films 8, 19 (1971).

183. M. J. Cohen, J. S. Harris, and J. R. Waldrop, Proc. GaAs Conference (St. Louis) Institute of Physics Conf. Series 45, 263 (1979).

184. See, for example, L. E. Davis, N. C. MacDonald, P. W. Palmberg, G. E. Riach, and R. E. Weber, Handbook of Auger Electron Spectroscopy (Physical Electronics Industries, Minn.; 1976).

185. P. D. Dapkus, R. D. Dupuis, R. D. Yingling, J. J. Yang, L. A. Moudy, R. E. Johnson, A. G. Campbell, H. M. Manasevit, and R. P. Ruth, Proc. 13th IEEE Photovoltaics Spec. Conf., Wash. (IEEE, N.Y.; 1979), pp. 960-965.

186. J. Jerhot and V. Snejdar, Thin Solid Films 52, 379 (1978).

187. V. Snejdar and J. Jerhot, Thin Solid Films 37, 303 (1976).

188. H. C. Card and E. S. Yang, IEEE Trans. Electron Dev. ED-24, 397 (1977).

189. L. L. Kazmerski, Solid-State Electron. 21, 1545 (1978).

190. L. L. Kazmerski, P. Sheldon, and P. J. Ireland, Thin-Solid Films 57, ____ (1979).

191. L. L. Kazmerski, P. Sheldon, and P. J. Ireland, J. Vac. Sci. Technol. 13, ____ (1979).

192. P. T. Landsberg and C. M. Kimpke, Proc. 13th IEEE Photovoltaics Spec. Conf., Wash. (IEEE, N.Y.; 1978), pp. 665-666.

193. R. Singh, T. N. Bhar, J. Shewchun, and J. J. Loferski, J. Vac. Sci. Technol. 13, ____ (1979).

194. L. M. Fraas, J. Appl. Phys. 49, 871 (1978).

195. C. Feldman, N. A. Blum, H. K. Charles, and F. G. Satkiewicz, J. Electron. Mat. 7, 309 (1978).

196. S. M. Sze, Physics of Semiconductor Devices (J. Wiley and Sons, N.Y.; 1969), pp. 22-149, 640-653.

197. A. G. Milnes and D. L. Feucht, Heterojunctions and Metal-Semiconductor Junctions (Academic Press, N.Y.; 1972), pp. 3-29, 51-57, 125-142.

198. L. L. Kazmerski, P. J. Ireland, F. R. White, and R. B. Cooper, Proc. 13th IEEE Photovoltaics Spec. Conf., Wash. (IEEE, N.Y.; 1978), pp. 184-189.

199. A. Rothwarf and A. M. Barnett, IEEE Trans. Electron Dev. ED-24, 381 (1977).

200. J. Y. Leong and J. H. Yee, Appl. Phys. Lett. (to appear 1979).

201. S. Wang and G. Wallis, Phys. Rev. 105, 1459 (1957).

202. J. H. Yee, The Systematic Computation of the Performance of Photovoltaic Cells Based on First Principles (DOE Report W-7405-ENG-48 (Modeling)), 1979.

203. J. L. Shay, S. Wagner, and J. C. Phillips, Appl. Phys. Lett. 28, 31 (1976).

204. S. Wagner, J. Cryst. Growth 31, 113 (1975).

205. Z. I. Alferov, Sov. Phys.--Semicond. 11, 1216 (1978).

206. K. A. Jones, C. H. Chang, and B. F. Shirreffs, Proc. 13th IEEE Photovoltaics Spec. Conf., Wash. (IEEE, N.Y.; 1978), pp. 513-518.

207. R. A. Logan, G. L. Pearson, and D. A. Kleinman, J. Appl. Phys. 30, 885 (1959).

208. P. Chaudhari, J. Vac. Sci. Technol. 9, 520 (1972).

209. O. Simpson, Nature 160, 791 (1947).

210. R. W. Hoffman, Thin Solid Films 34, 185 (1976).

211. See, for example, S. Amelinckx, The Direct Observation of Dislocations (Academic Press, N.Y.; 1964).

212. R. M. Broudy, Advances in Physics 12, 135 (1963).

213. W. T. Read, Phil. Mag. 45, 775 (1954).

214. D. L. Dexter and F. Seitz, Phys. Rev. 86, 964 (1952).

215. See, for example, W. Bollmann, Crystal Defects and Crystalline Interfaces (Springer-Verlag, Berlin-Heidelberg; 1970), pp. 78-97.

216. R. A. Brown, Phys. Rev. 156, 692 (1967).

217. A. Howie, Phil. Mag. 5, 251 (1960).

218. H. Blank, P. Delavignette, and S. Amelinckx, Phys. Stat. Solidi 2, 1660 (1964).

219. R. H. Bube, Photoconductivity of Solids (J. Wiley and Sons, N.Y.; 1960), pp. 417-420.

220. L. L. Kazmerski, W. B. Berry, and C. W. Allen, Proc. Natl. Elect. Conf. 26, 202 (1970).

211. L. L. Kazmerski, W. B. Berry, and C. W. Allen, J. Appl. Phys. 43, 3521 (1972).

222. L. L. Kazmerski, W. B. Berry and C. W. Allen, Solar Cells (Gordon and Breach, London; 1971), pp. 141-154.

$d_G = \ell_1$ = grain size

$d_B = \ell_2$ = grain boundary width

R_N = resistance of one current path formed by interconnected grains and grain boundary regions (see Fig. 3-48).

L_{DB} = effective Debye length in grain boundary region

σ_p = conductivity of polycrystalline semiconductor

σ_{Bb} = bulk conductivity of grain boundary region

$$J_i(V_1, V_2) = -(q/kT) \int_{V_1}^{V_2} [\exp(qV/kT)/F_1(V, V_{OB})] dV \qquad (i = 1 \text{ or } 2)$$

$$F_1(V, V_{OB}) = \pm \left\{ 2[\exp(qV/kT) - \exp(qV_{OB}/kT) + (q/kT)(V_{OB}-V)] \right\}^{\frac{1}{2}}$$

where + corresponds to V<0
       − corresponds to V>0

$D = D_u/D_s$

$D_u = \det(A_{1n}; R_{m,n})$ 	$m = 2,3,4$ 	$n = 1,2,3,4$

$D_s = \det(R_{m,n})$ 	$m = 1,2,3,4$ 	$n = 1,2,3,4$

$R_{m,n}$ is a symmetrical square matrix with:

$R_{1,1} = R_G + 2(R_{GBOG} + R_{GBOB}) + R_{B1} + R_{B2}$; $R_{1,2} = R_{2,1} = R_{1,3} = R_{3,1} = -(R_{GBOG} = R_{GBOB})$

$R_{1,4} = R_{4,1} = -(R_{B1} + 2R_{GBOB})$; 	$R_{2,2} = R_{2,3} = R_{GBOG} + R_{GBOB} + R_{GBD}$

$R_{2,3} = R_{3,2} = 0$; $R_{2,4} = R_{4,2} = R_{3,4} = R_{4,3} = R_{GBOB}$; $R_{4,4} = R_T + R_{B1} + 2R_{GBOB}$

$A_{1,n}$ elements are:

$$A_{1,1} = R_{HGb}[2L_{DG}(d_G + d_B)/R_N d_G^2] J_{1G}(V_{DG}, V_{OG}) + R_{HBb}\sigma_{Bb}d_B \cdot$$
$$[(2L_{DB}/d_B)^2 J_{1B}(V_{DB}, V_{OB}) J_2(V_{DB}, V_{OB}) - (d_G + d_B)/(2L_{DB}R_N\sigma_{Bb}d_G J_2(V_{DB}, V_{OB})) -1]$$

$$A_{1,2} = A_{1,3} = -\tfrac{1}{2} R_{HBb} \sigma_{Bb} d_B \ (2L_{DB}/d_B)^2 \ J_{1B}(V_{DB}, V_{XB}) \ J_2 \ (V_{DB}, V_{OB}) -$$

$$R_{HGb} \ [\ (d_B + d_B) \ L_{DG}/R_N d_G^2] \ J_{1G} \ (V_{DG}, \ V_{XG})$$

$$A_{1,4} = -R_{HBb} \sigma_{Bb} d_B \ (2L_{DB}/d_B)^2 \ J_{1B} \ (V_{DB}, V_{OB}) \ J_2 \ (V_{DB}, \ V_{OB})$$

where subscripts B and G on current densities refer to grain boundary and grain respectively. V_{XG} and V_{XB} are the diffusion potentials at the edge of the space-charge layers in the grain and grain boundary regions, respectively.
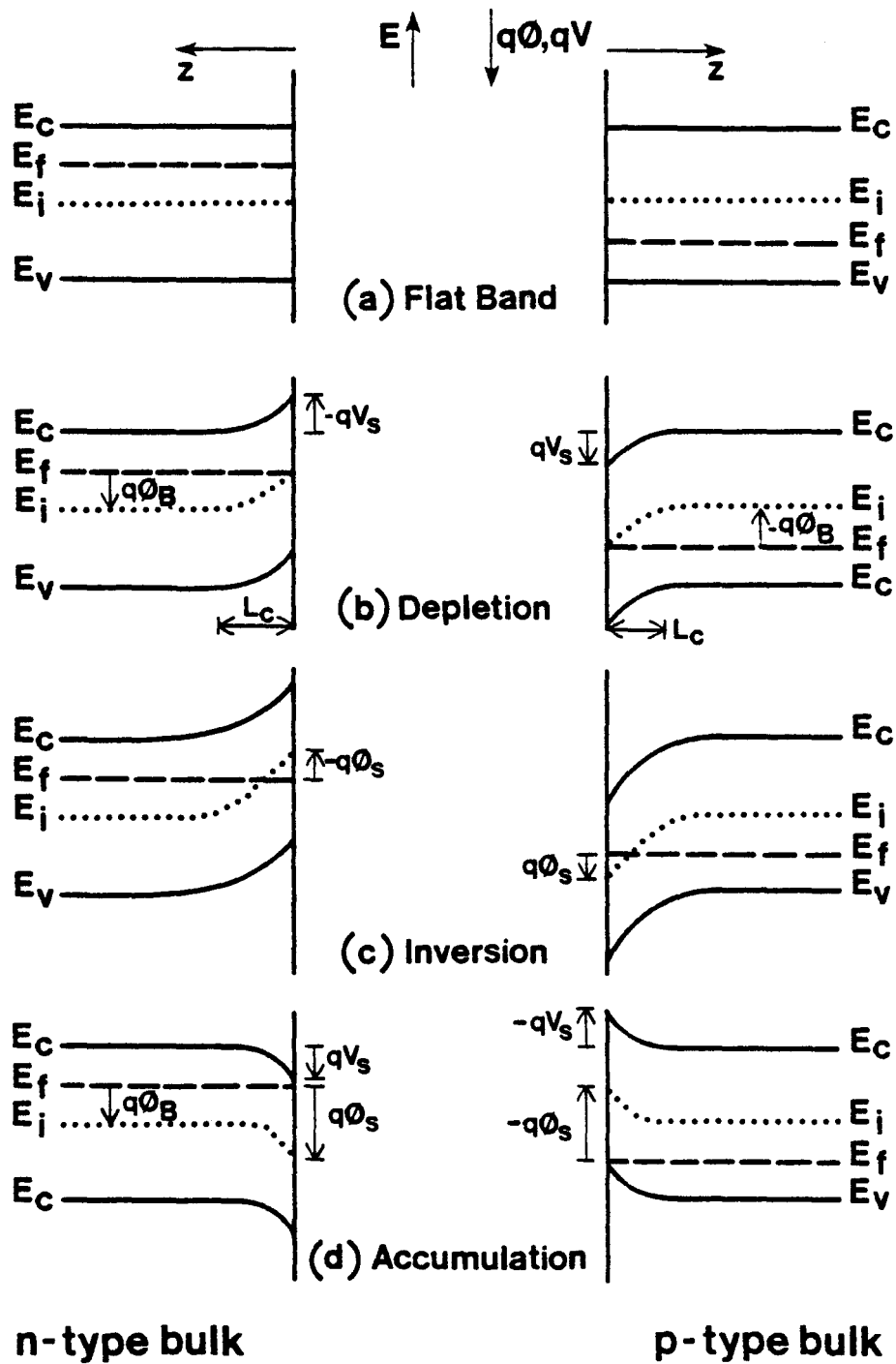
Fig. 3-1   Band structure near the semiconductor surface for: (a) flatband,
(b) depletion, (c) inversion, and (d) accumulation conditions.
Both n- and p-type bulk semiconductors are represented.
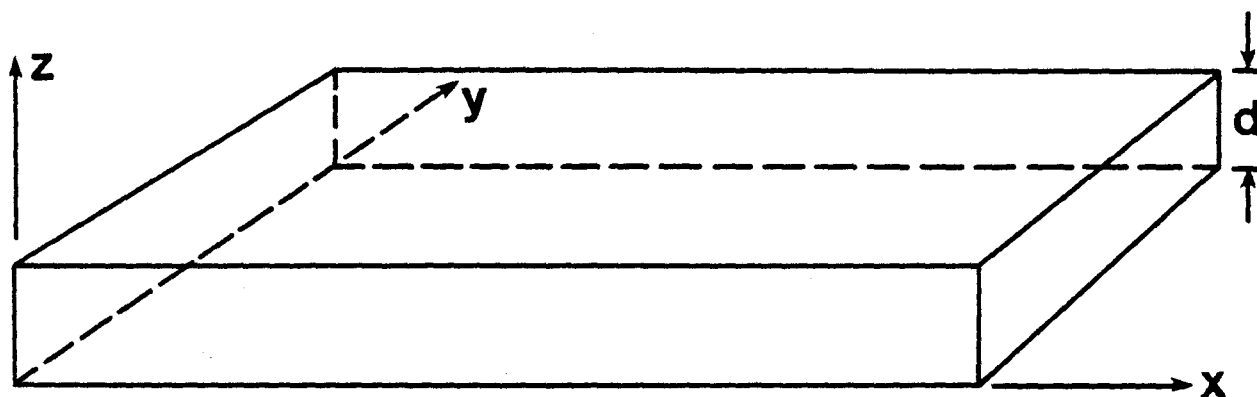
Fig. 3-2   Thin film geometry and coordinate system.
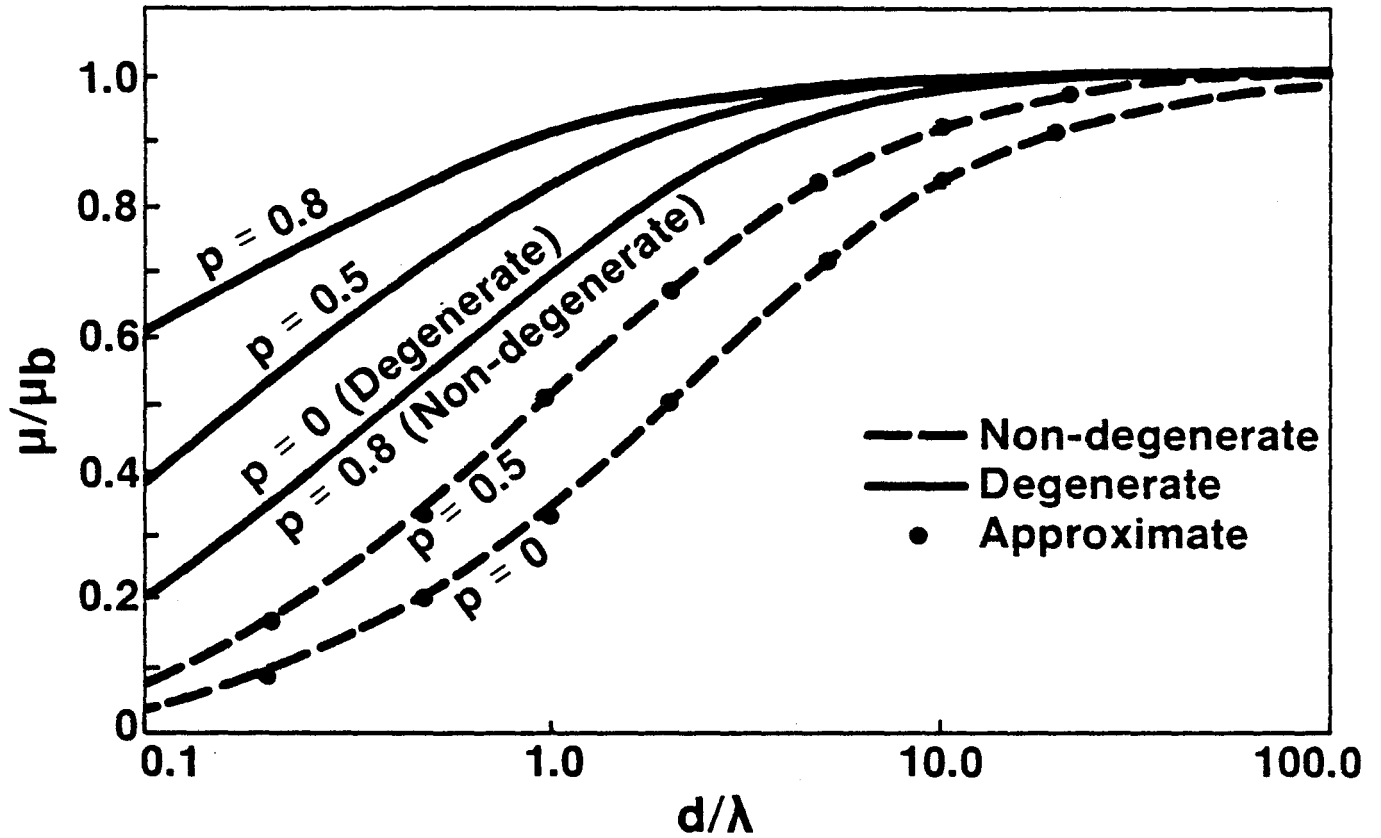
Fig. 3-3 Ratio of average film mobility to bulk mobility as a function of the ratio of film thickness to mean surface scattering length using both Fermi statistics (solid lines, representing degenerate semiconductor case of Eq. 3.21) and Boltzmann statistics (broken lines, representing nondegenerate semiconductor case of Eq. 3.22). The effects of specular and diffuse scattering are shown by the difference in the specularity factor, p. The dots represent the approximate solution given by Eq. 3.29 (from Anderson [6]).
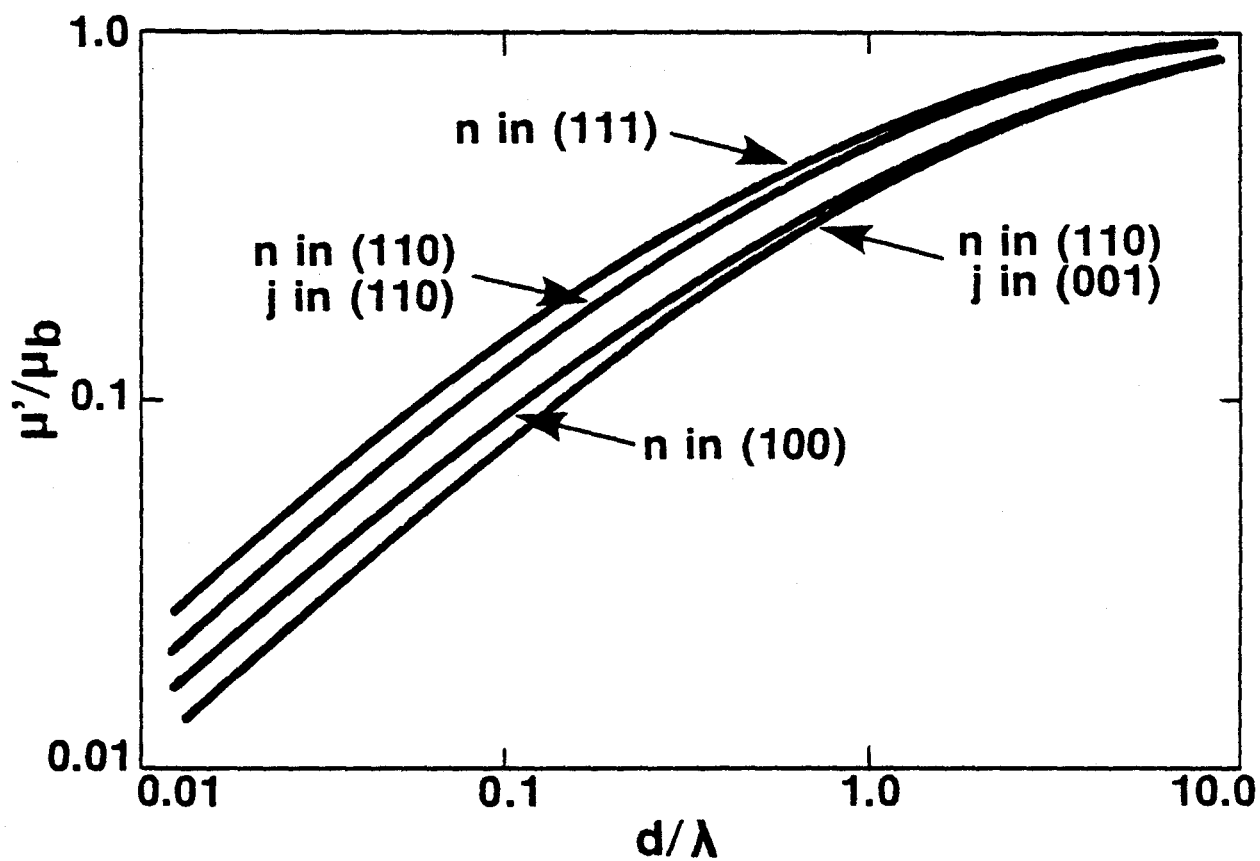
Fig. 3-4   Ratio of effective film mobility to bulk mobility as a function of
the ratio of film thickness to mean surface scattering length for
the case of ellipsoidal energy surfaces, indicating the anisotropy
of the electrical properties (from Ham and Mattis [28]).
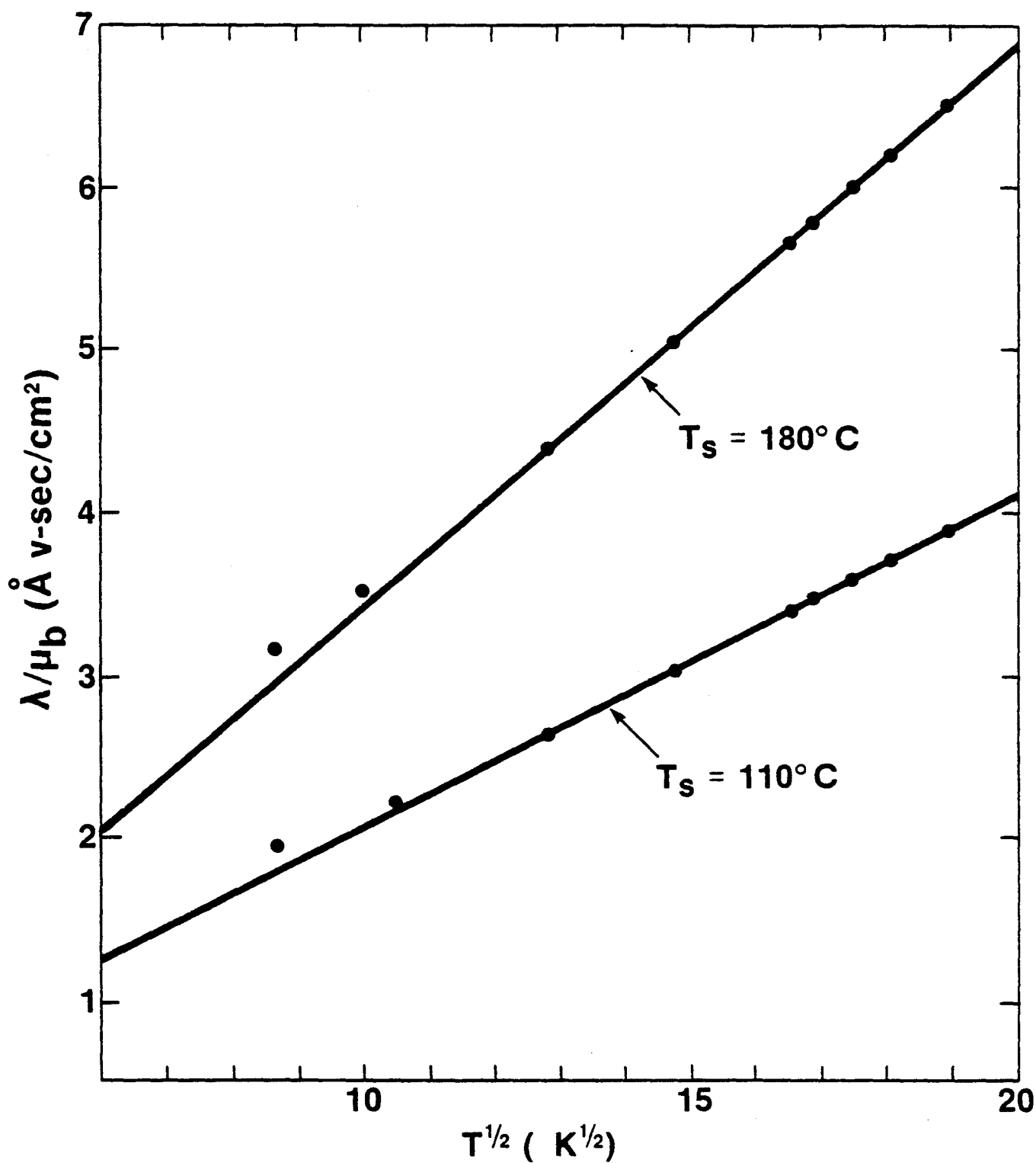
Fig. 3-5 Dependence of the ratio of the mean surface scattering length to bulk mobility upon film temperature, for substrate temperatures T_s = 110 C (383 K) and 180 C (453 K), indicating a $T^{1/2}$ relationship for CdS thin films (from Kazmerski [30]).
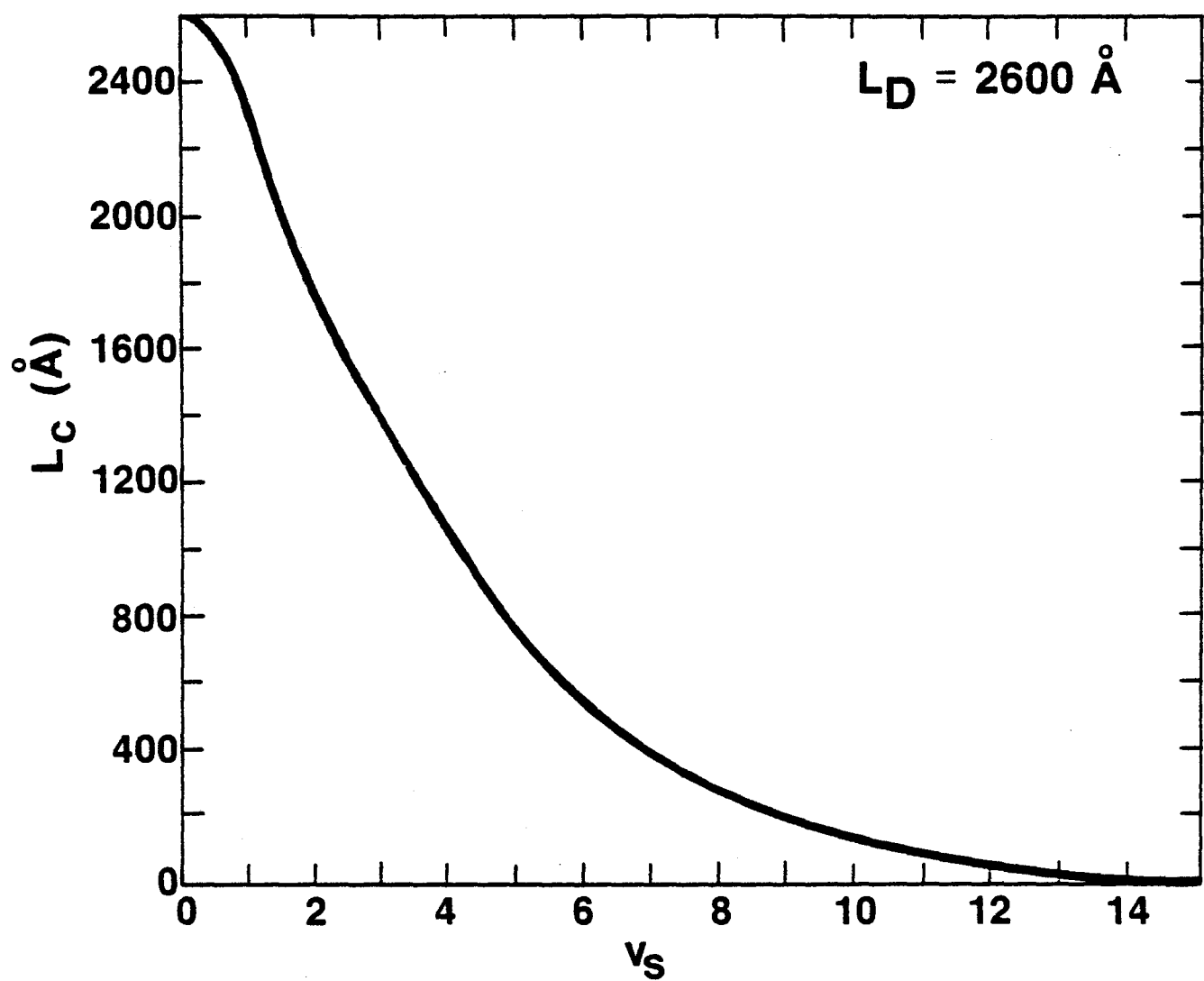
Fig. 3-6. Calculated surface layer thickness as a function of surface potential for CdS film with bulk concentration of $10^{14}/cm^3$. L_D is the Debye length (from Waxman et al. [32]).
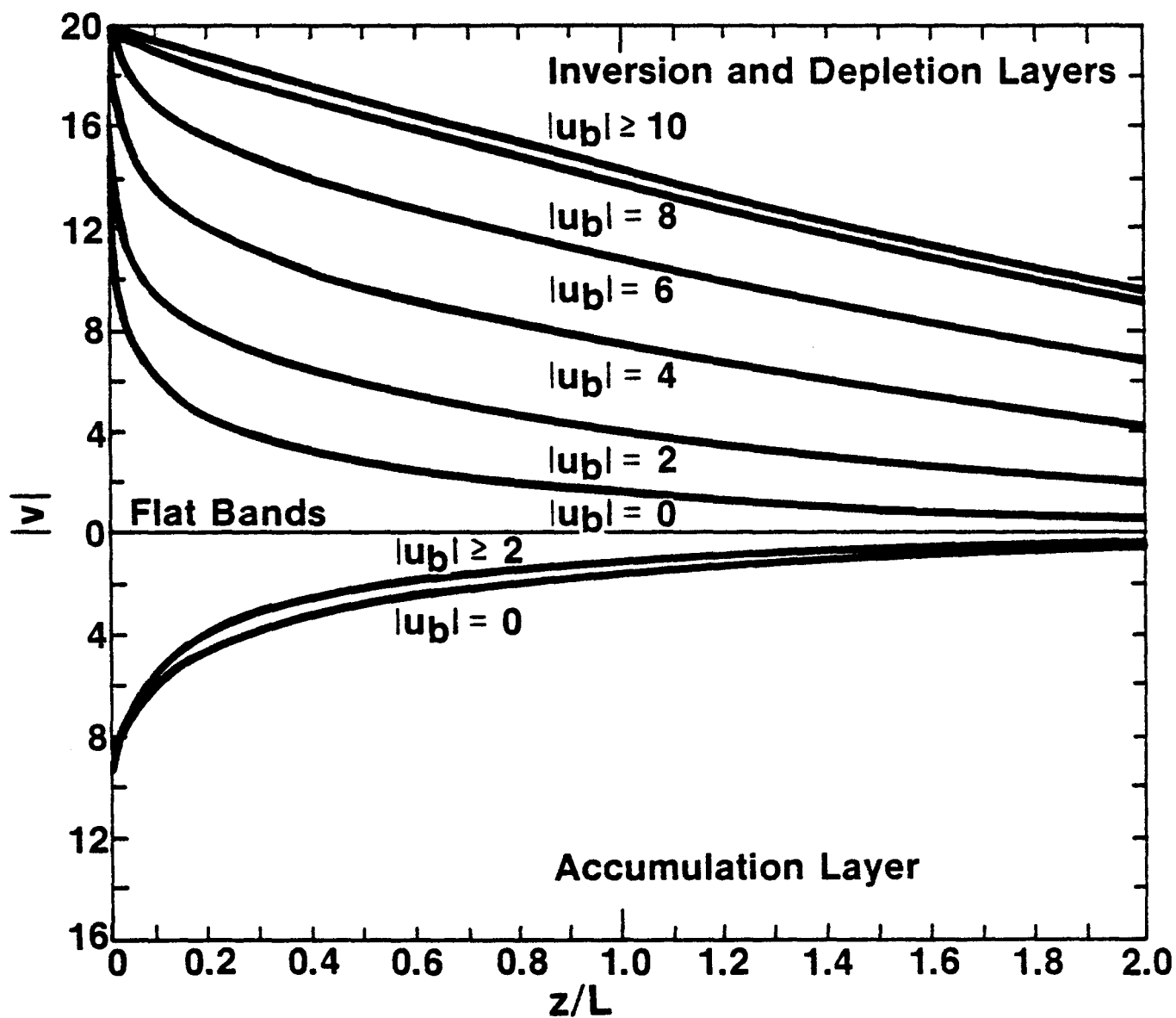
Fig. 3-7   The shape of the barrier potential as a function of the normalized distance from the surface (L is the Debye length) for various values of the bulk potential. The magnitude of $|v_s|$ is taken to be 20 (from Many et al. [27]).
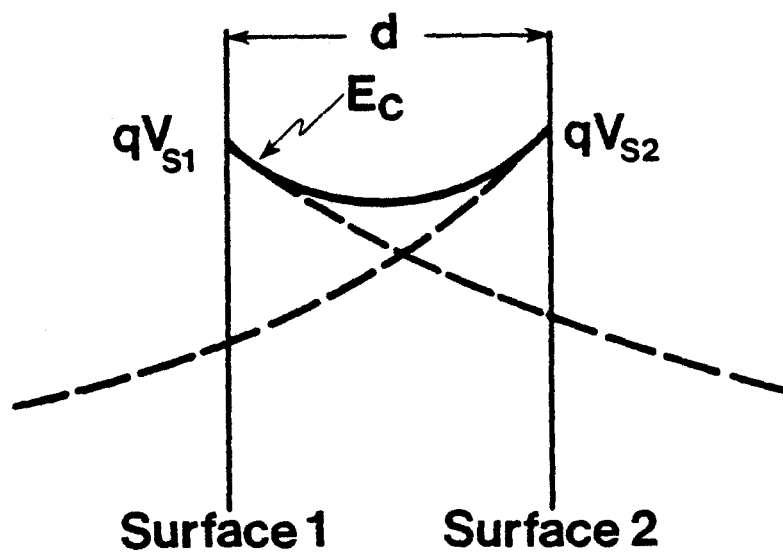
Fig. 3-8   Effective band structure resulting from band bending at surfaces in
            a very thin semiconductor film.
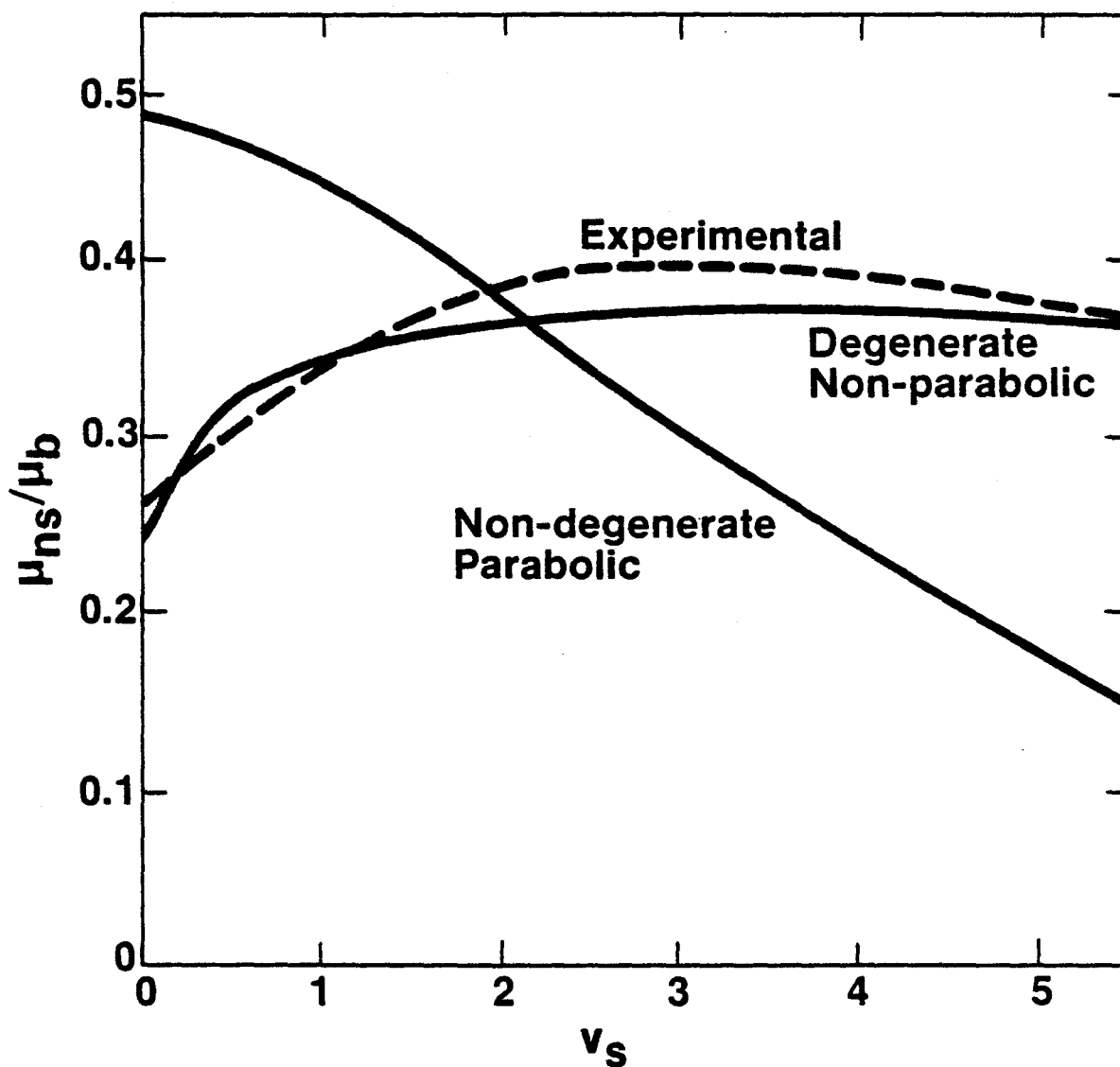
Fig. 3-9 Normalized surface mobility (to bulk value) as a function of surface potential for degenerate and nondegenerate cases. Data for degenerate InSb thin film are included (from Juhasz [35]).
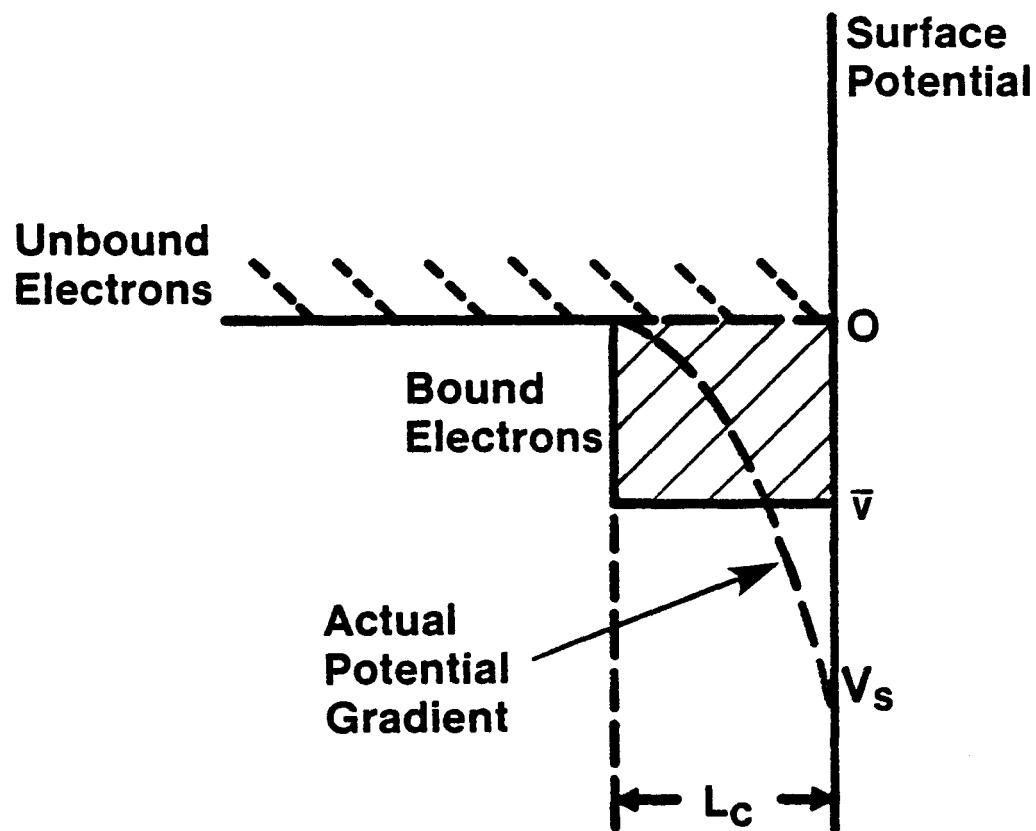
Fig. 3-10 Potential well model for calculating scattering at a surface (from Anderson [6]).
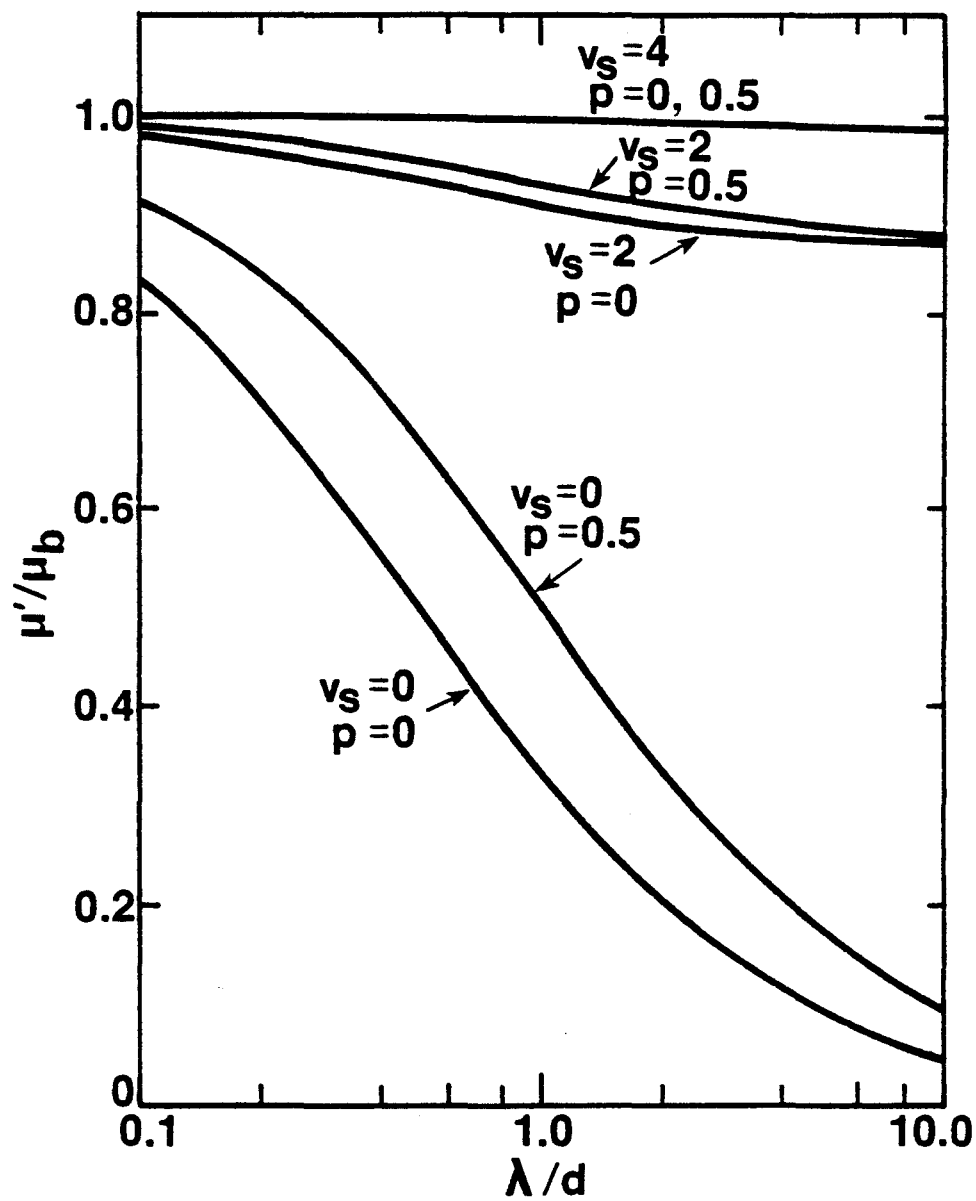
Fig. 3-11 Dependence of the ratio of film to bulk mobility upon the ratio of mean surface scattering length to film thickness for various surface potentials ($v_s = qV_s/kT$), using nondegenerate model given by Eq. 3.44. Effects of specular and diffuse scattering are also indicated.
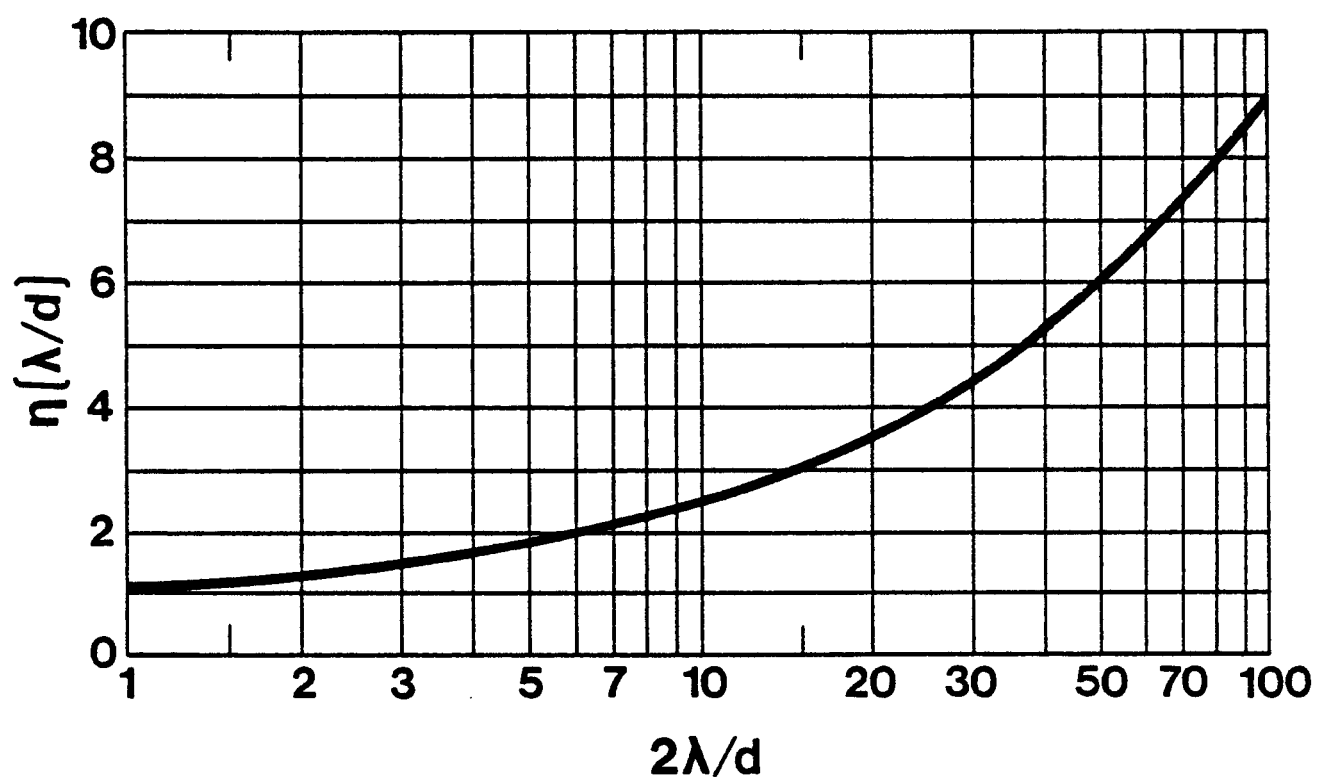
Fig. 3-12 The Hall coefficient correction factor as a function of the ratio
of mean surface scattering length to film half-thickness (from
Amith [37]).
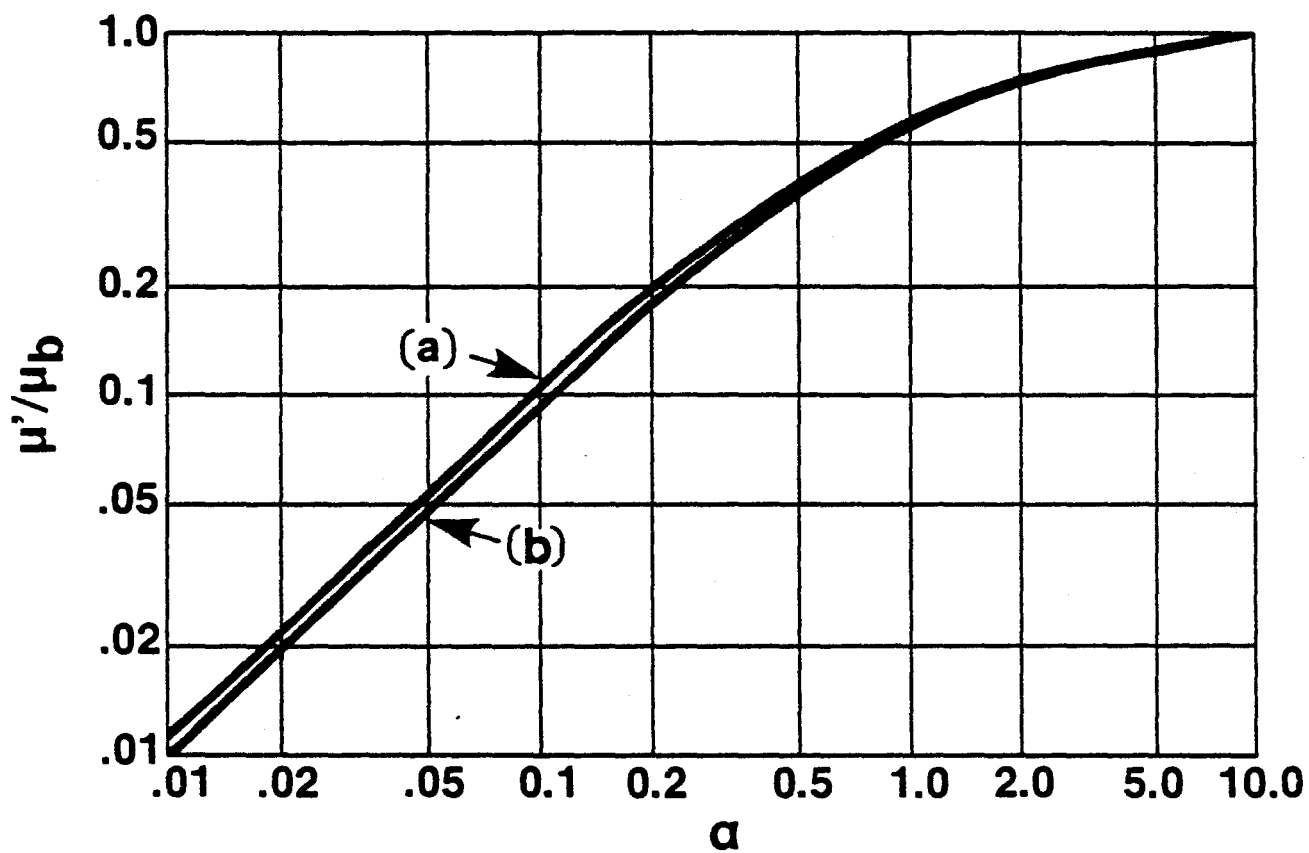
Fig. 3-13 The normalized film mobility (to the bulk value) as a function of the parameter α for (a) the effective conductivity mobility, and (b) the effective Hall mobility (from Zemel [21]).
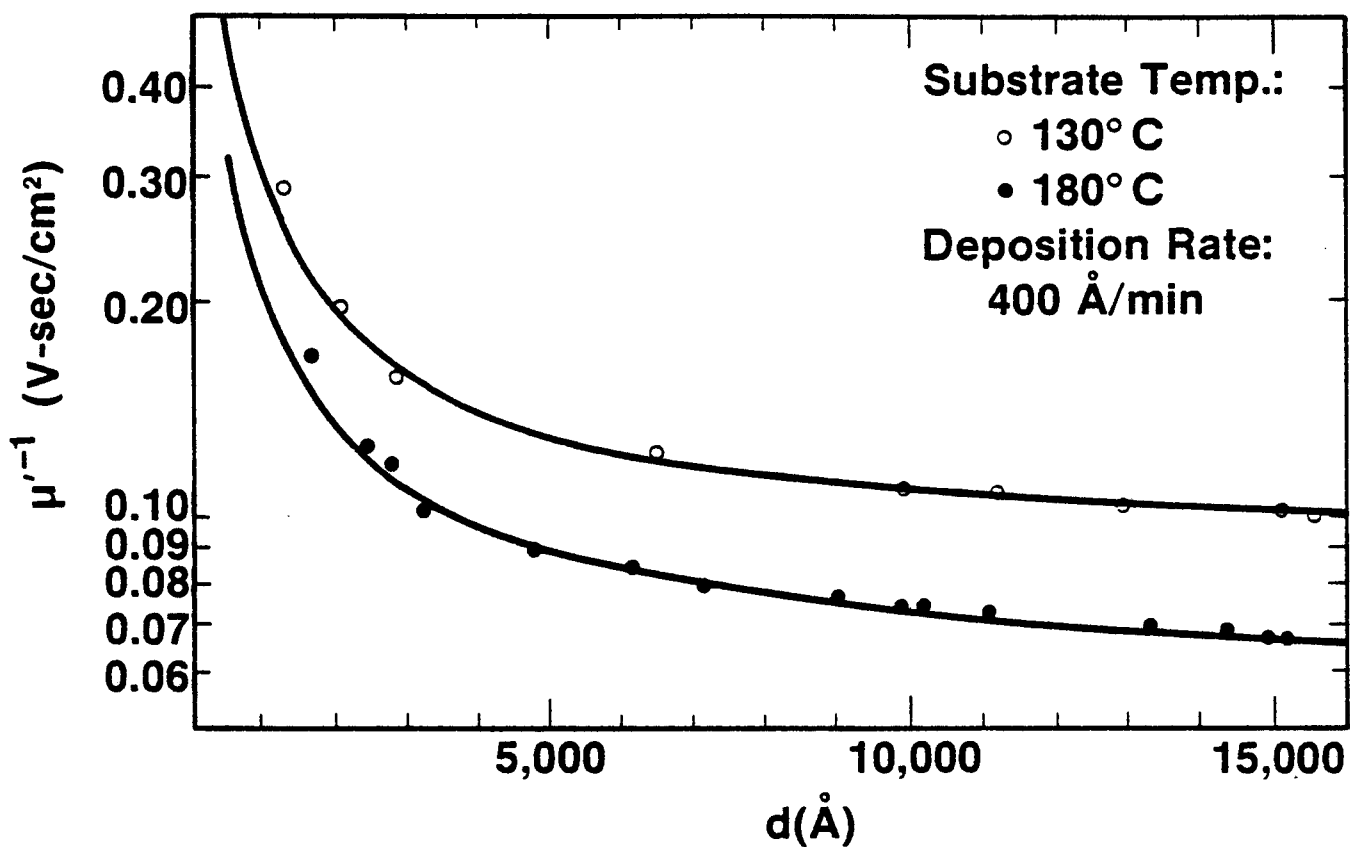
Fig. 3-14 Reciprocal film mobility dependence on thickness for substrate temperatures of 130 C (403 C) and 180 C (453 K). The solid lines indicate the model of Eq. 3.29 with $\lambda = 1100$ Å for the CdS films (from Kazmerski et al. [29]).
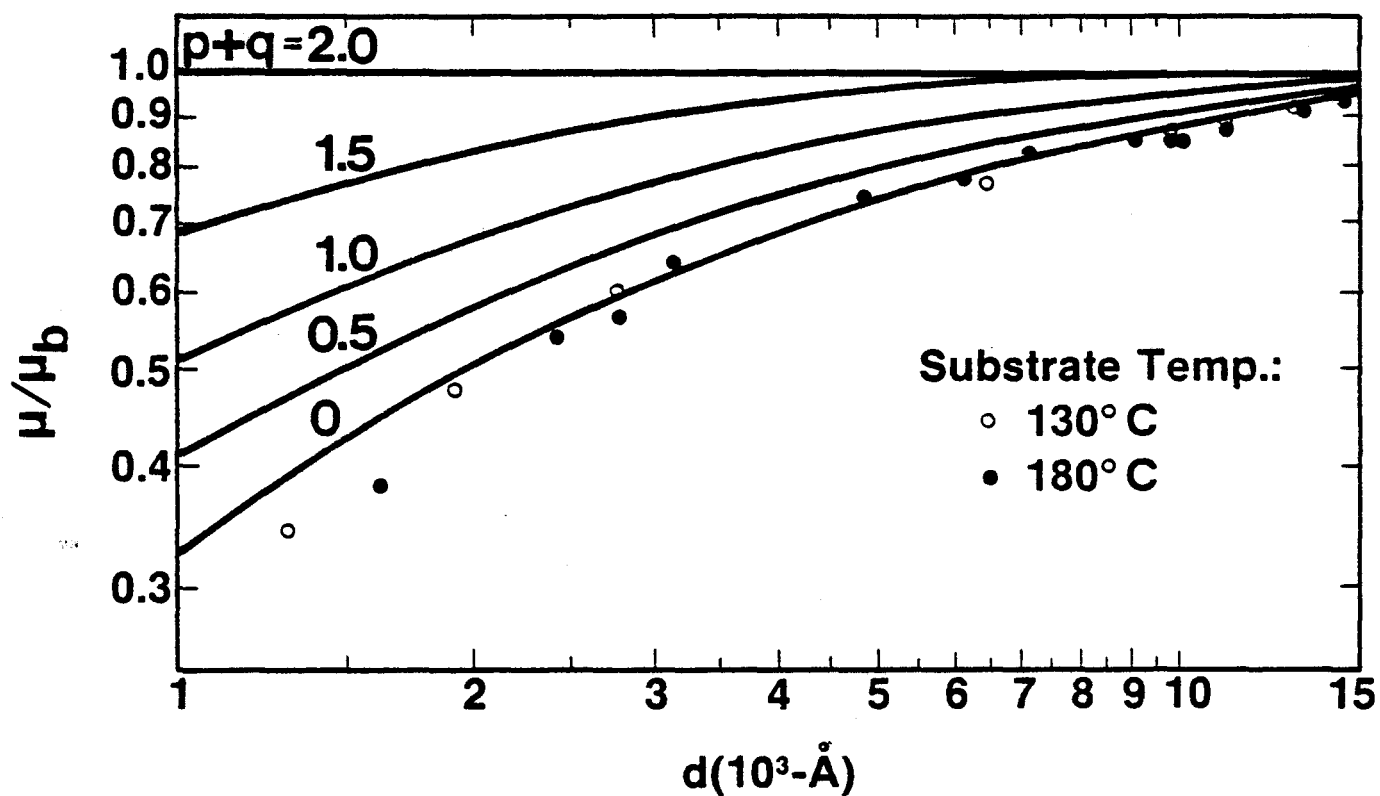
Fig. 3-15 Dependences of the film mobility on thickness for CdS thin films. The solid lines represent Eq. 3.30 for various values of the specular scattering parameters, p and q, with $\lambda = 1100$ Å. The experimental data indicate that the scattering is almost entirely diffuse (from Kazmerski et al. [29]).
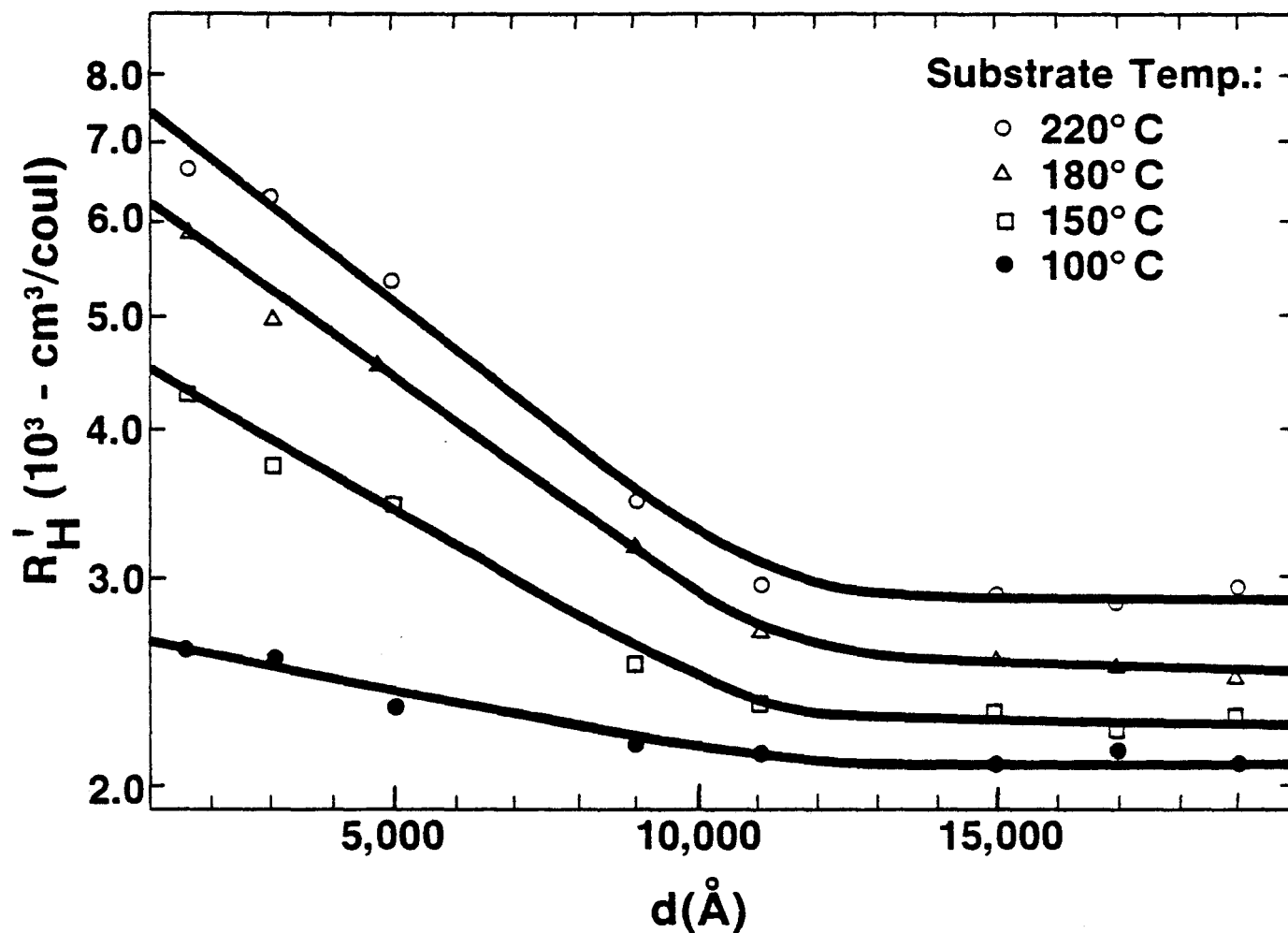
Fig. 3-16 Hall data dependence upon CdS film thickness for various substrate temperatures indicating variation of the mean surface scattering length with substrate temperature (from Kazmerski [30]).
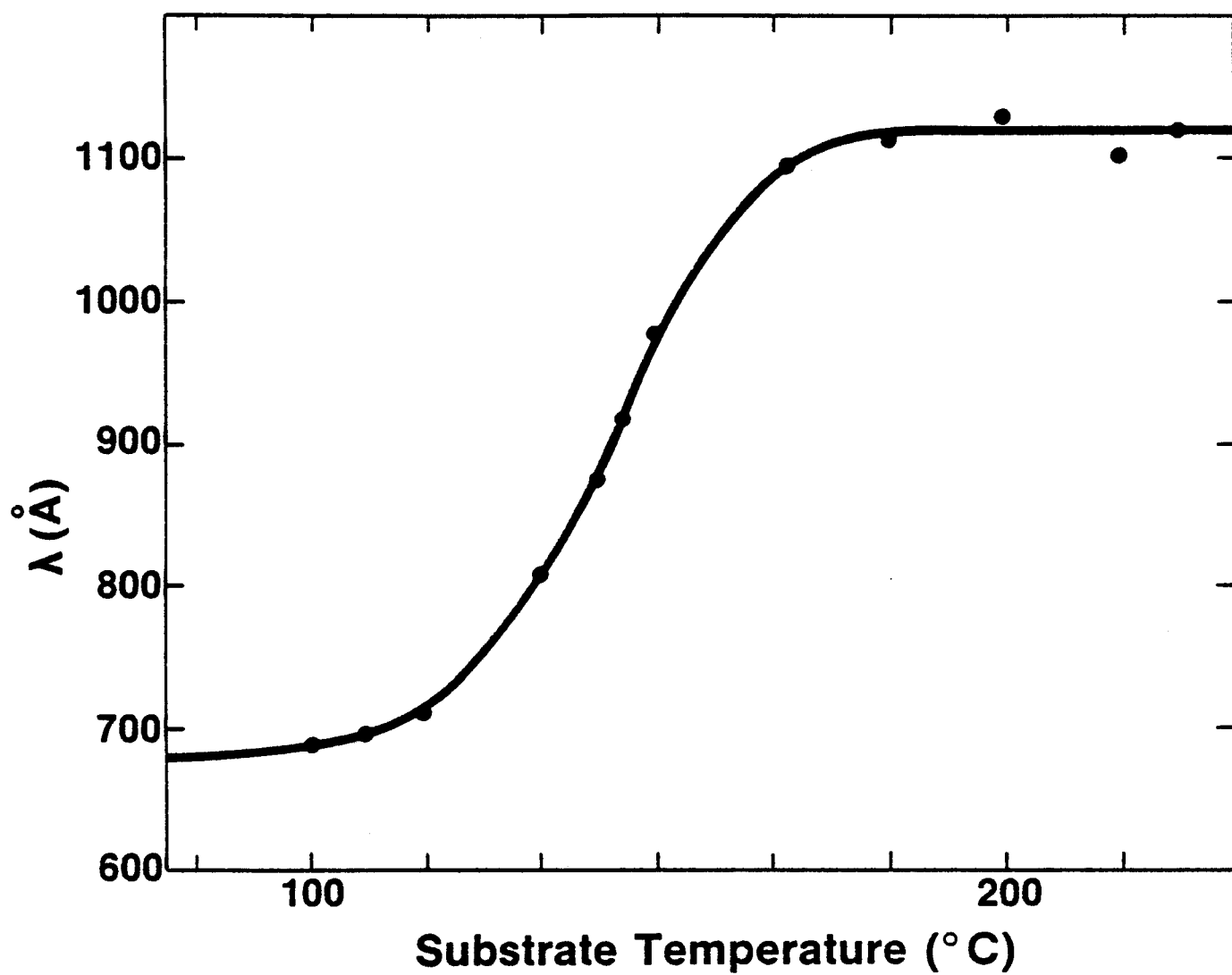
Fig. 3-17 Surface scattering length as a function of substrate temperature for CdS thin films (from Kazmerski [30]).
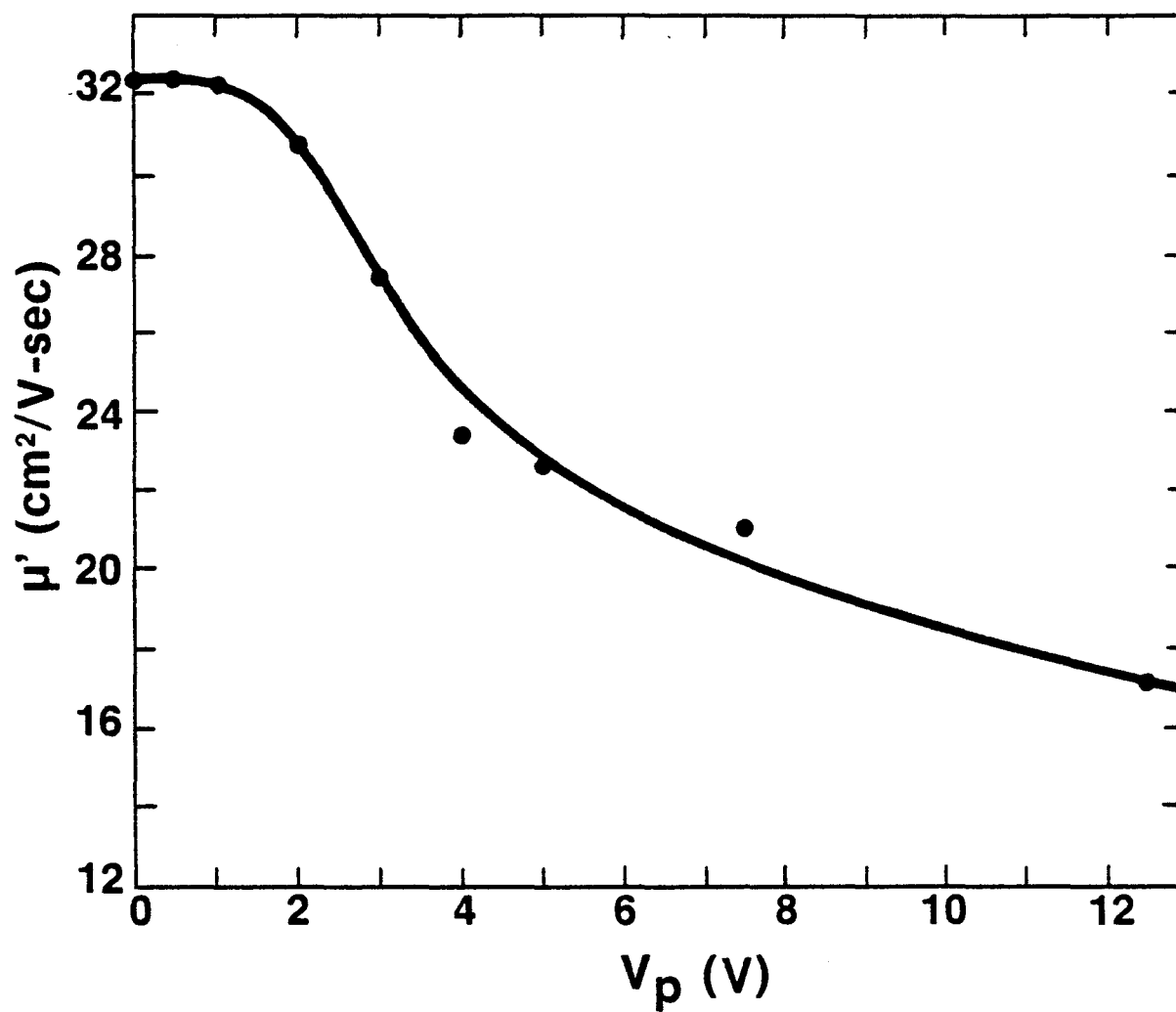
Fig. 3-18 Variation of Hall mobility with applied surface potential in field-
effect structure with 4000 Å CdS film and 600 Å thick CaF$_2$ surface
insulator layer (from Waxman et al. [32]).
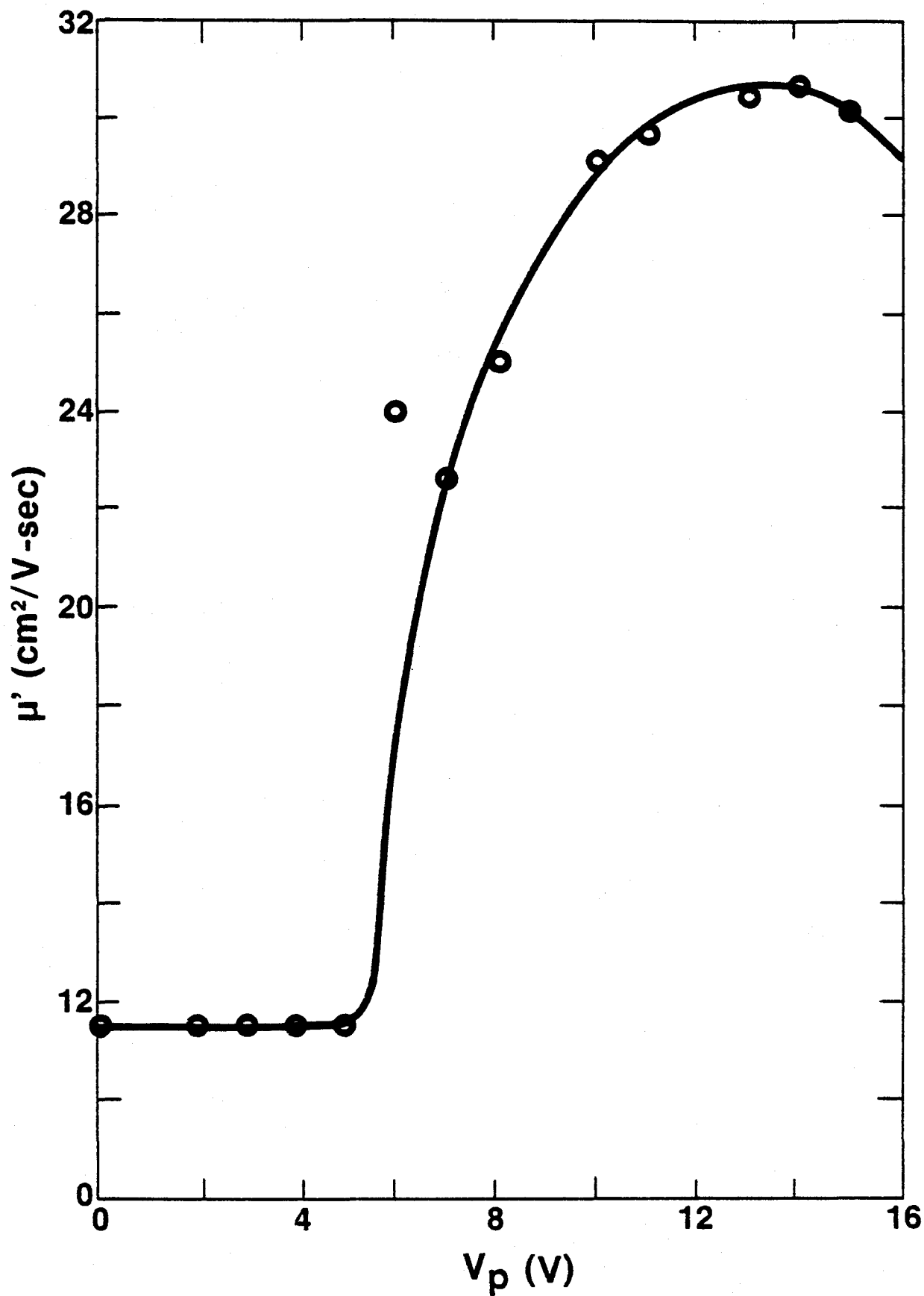
Fig. 3-19 Variation of Hall mobility with applied surface potential in field-
effect structure with 2000 Å CdS film and 600 Å thick SiO insulator
layer (from Waxman et al. [32]).
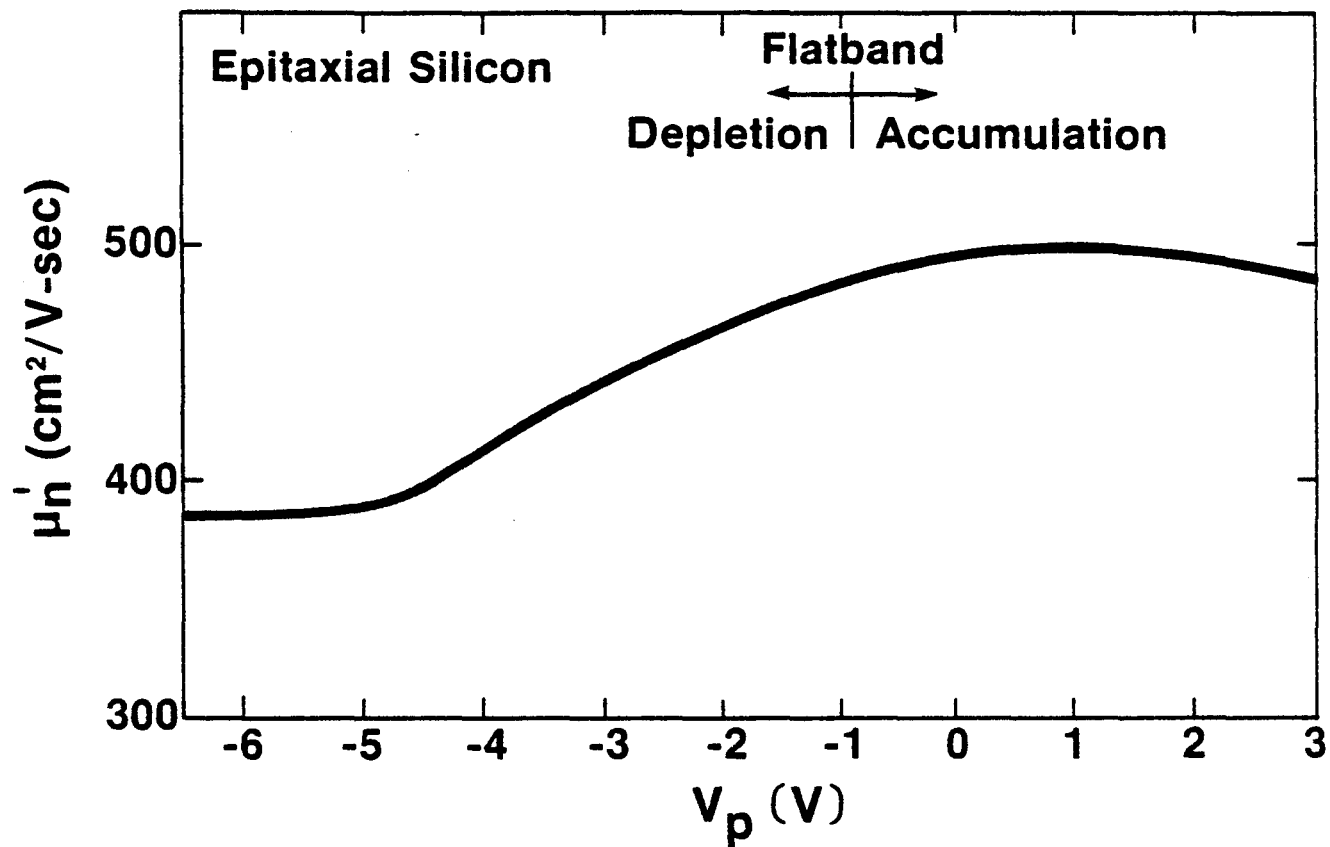
Fig. 3-20 Average film mobility as a function of applied surface potential for Si field effect structure (from Ypri [81]).
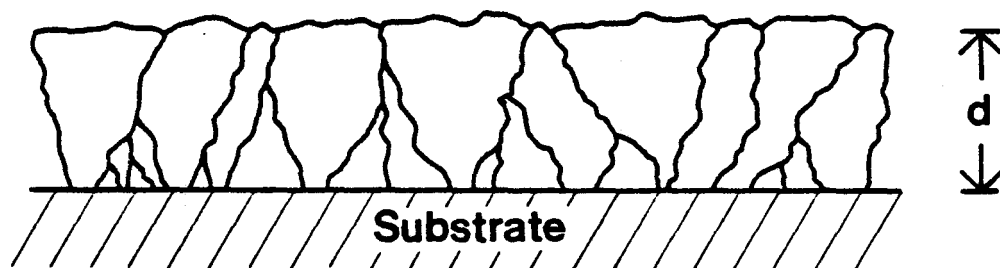
Fig. 3-21 Conceptual cross-sectional view of polycrystalline thin film
            indicating a degree of columnar growth.
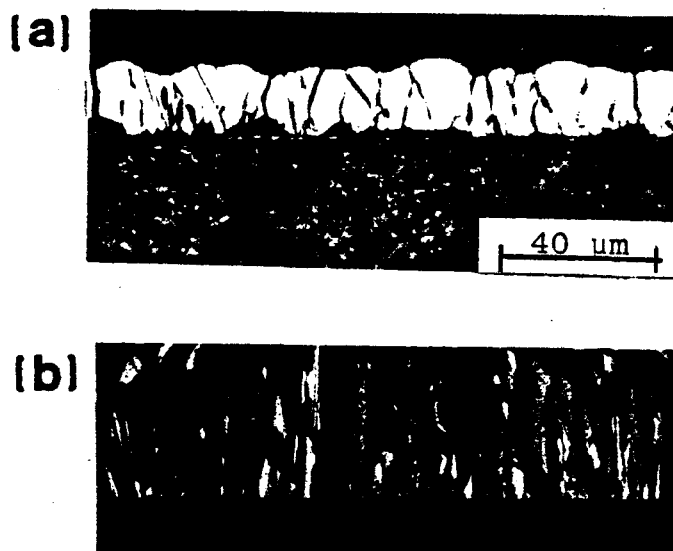
Fig. 3-22 Micrographs showing columnar growth in silicon: (a) Polycrystalline silicon film grown by chemical vapor deposition (from Chu et al. [84]); (b) multicrystalline silicon produced by casting (from Helmreich [85]).
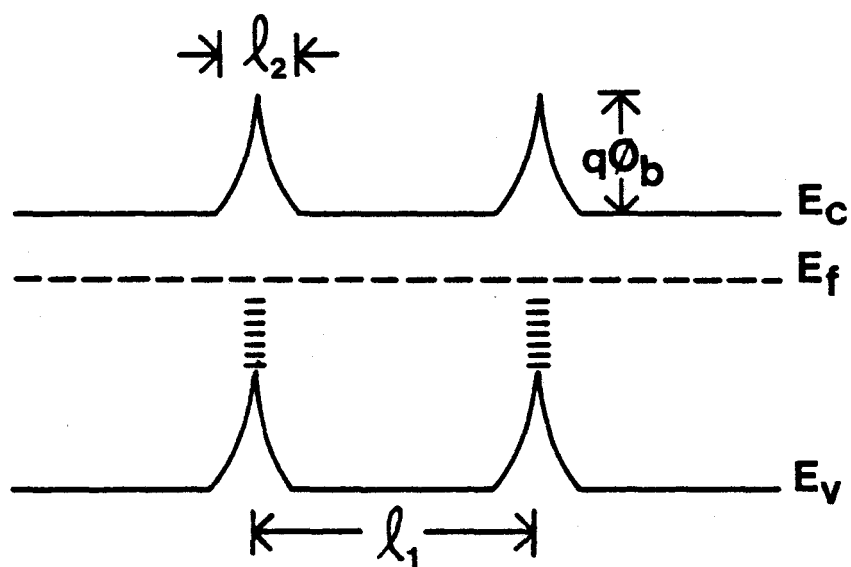
Fig. 3-23 Energy band representation of n-type polycrystalline semiconductor thin film with grain size ℓ_1 and grain boundary width ℓ_2. Grain boundary barrier potential is $q\phi_b$.
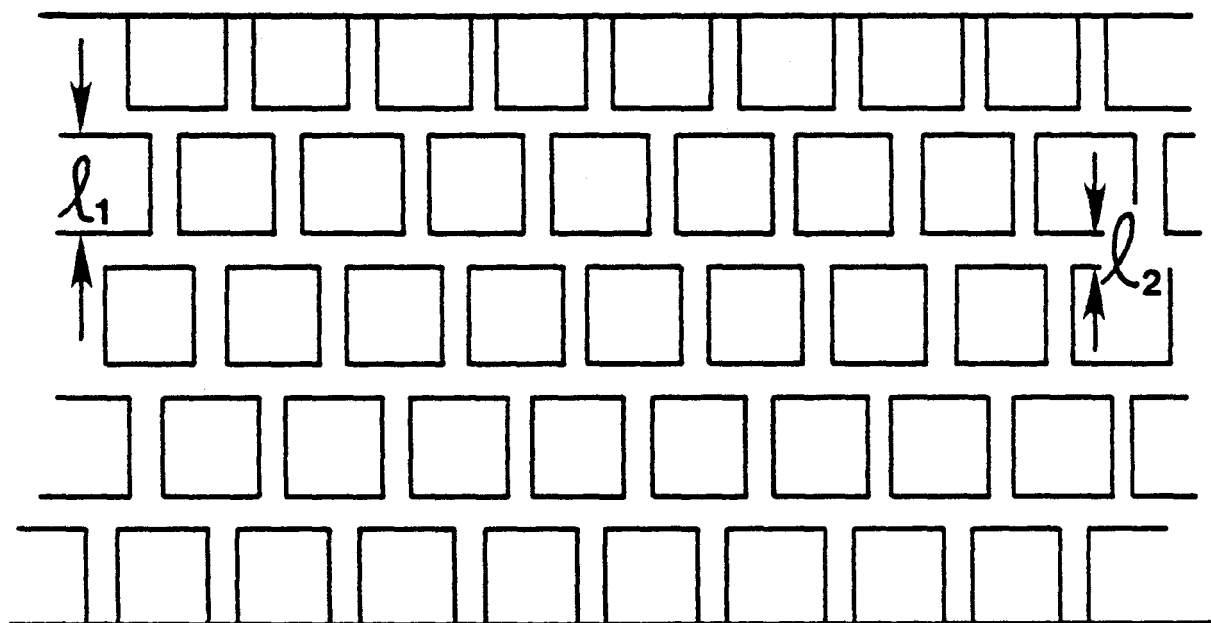
Fig. 3-24 Model of thin polycrystalline film proposed by Berger [89]. ℓ_1 represents the grain size and ℓ_2, the grain boundary width.
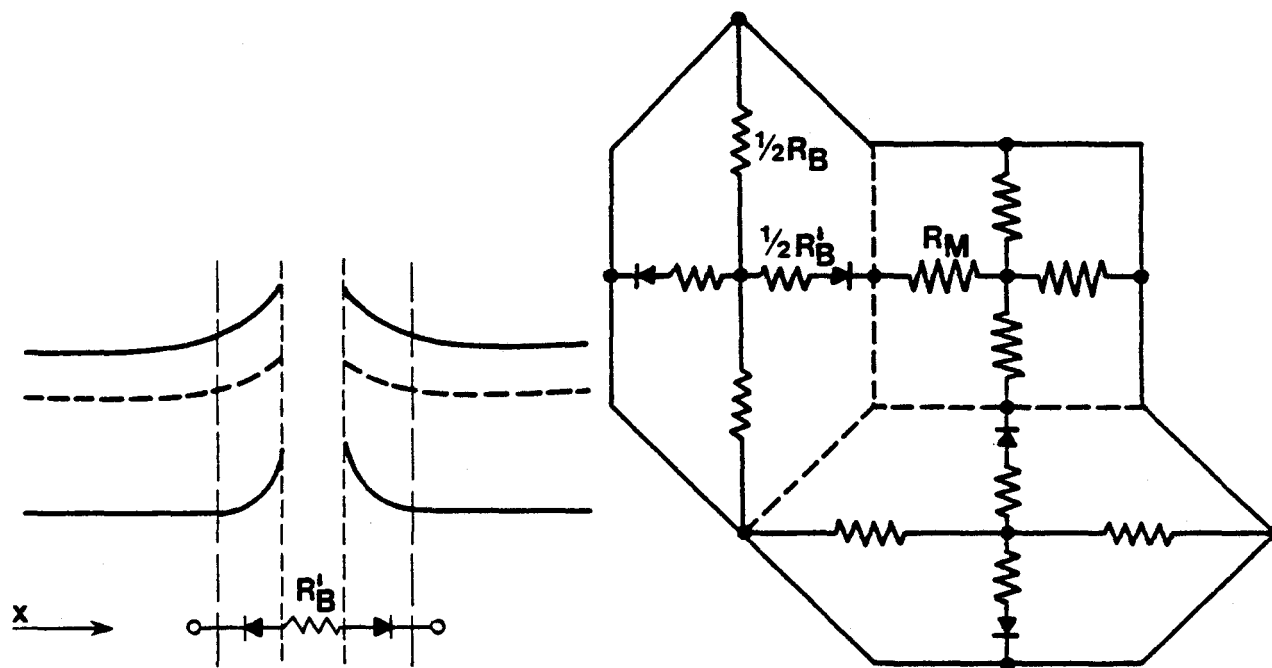
Fig. 3-25 Electrical model of polycrystalline thin film. R_B' and R_M are the resistances of the grain boundary and grain regions, respectively (from Kuznicki [96]).
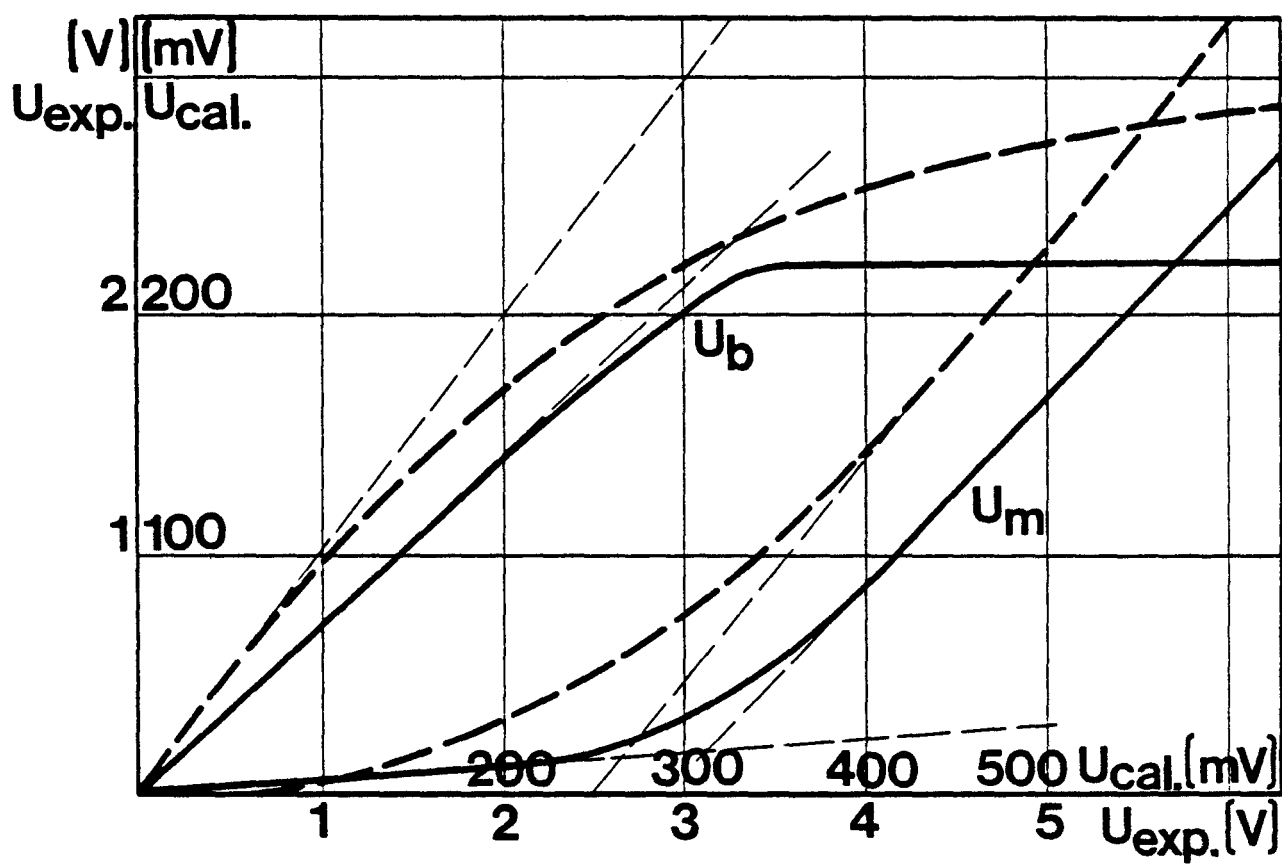
Fig. 3-26 The comparison of the experimental and calculated (using the model of Fig. 3-25) barrier voltage, U_b, and grain voltage, U_M, as a function of the total voltage, V. Solid line indicates experimental data for CdSe and broken line, the calculated values (from Kuznicki [96]).
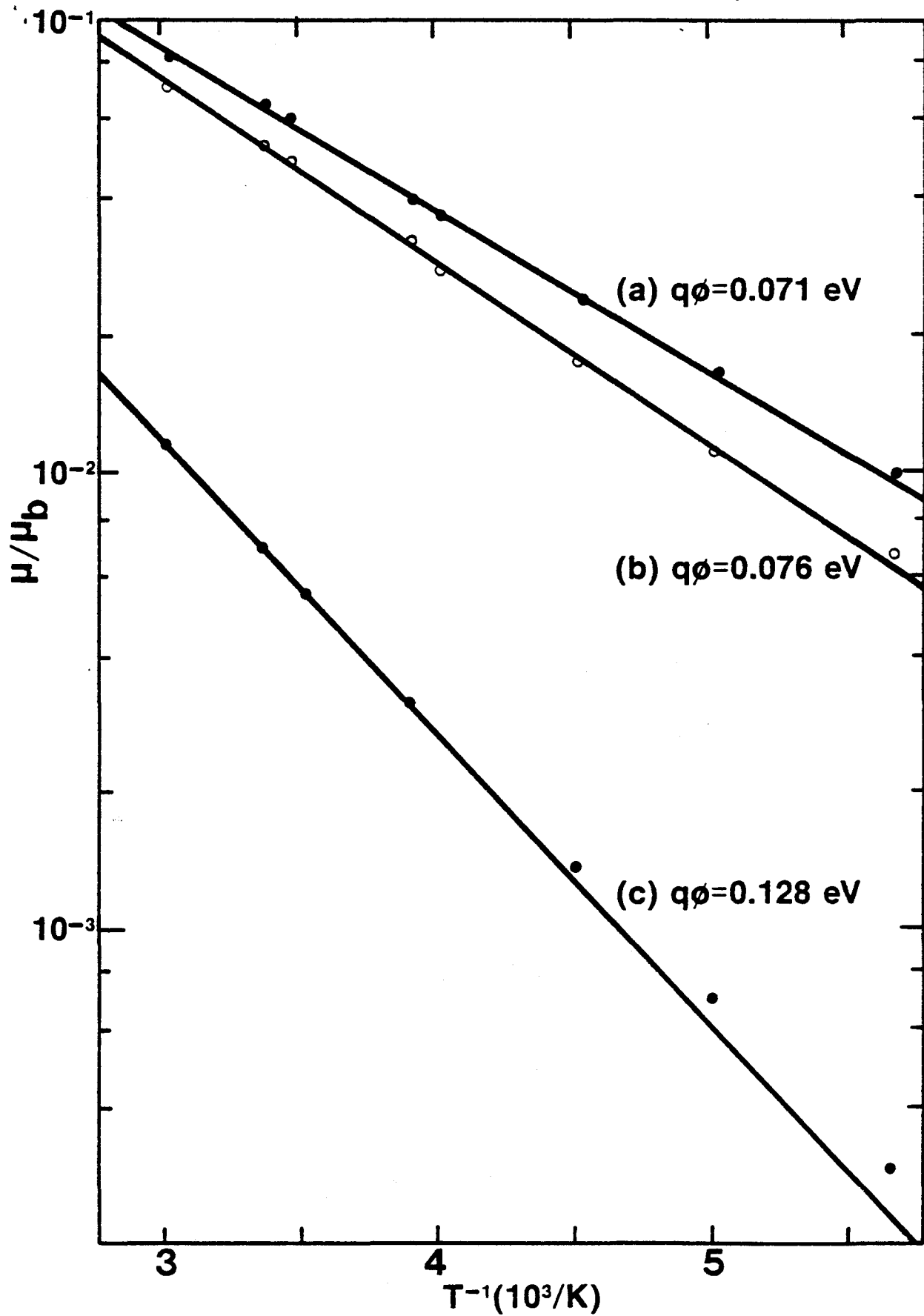
Fig. 3-27 Mobility-inverse film temperature dependence for CdS thin films. (a) 180 C (453 K), and (b) 130 C (403 K) substrate temperatures. (c) is identical to (a) but at a high deposition rate (from Kazmerski et al. [29]).
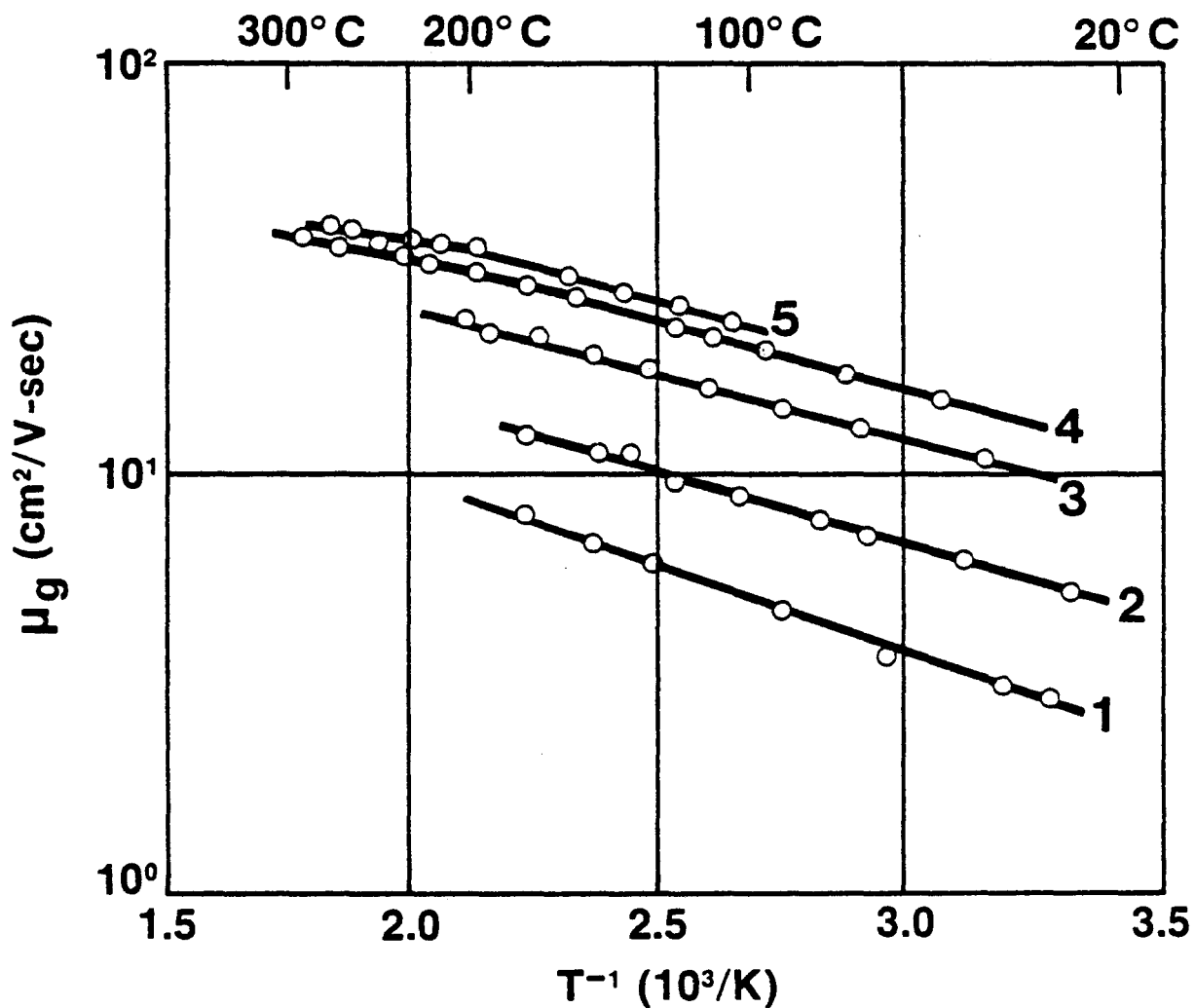
Fig. 3-28 Dependence of film Hall mobility upon inverse temperature for CdS thin films for various substrate temperatures: (1) 24 C (297 K), (2) 174 C (447 K), (3) 216 C (489 K), (4) 305 C (578 K), and (5) 330 C (603 K) (from Berger [89]).
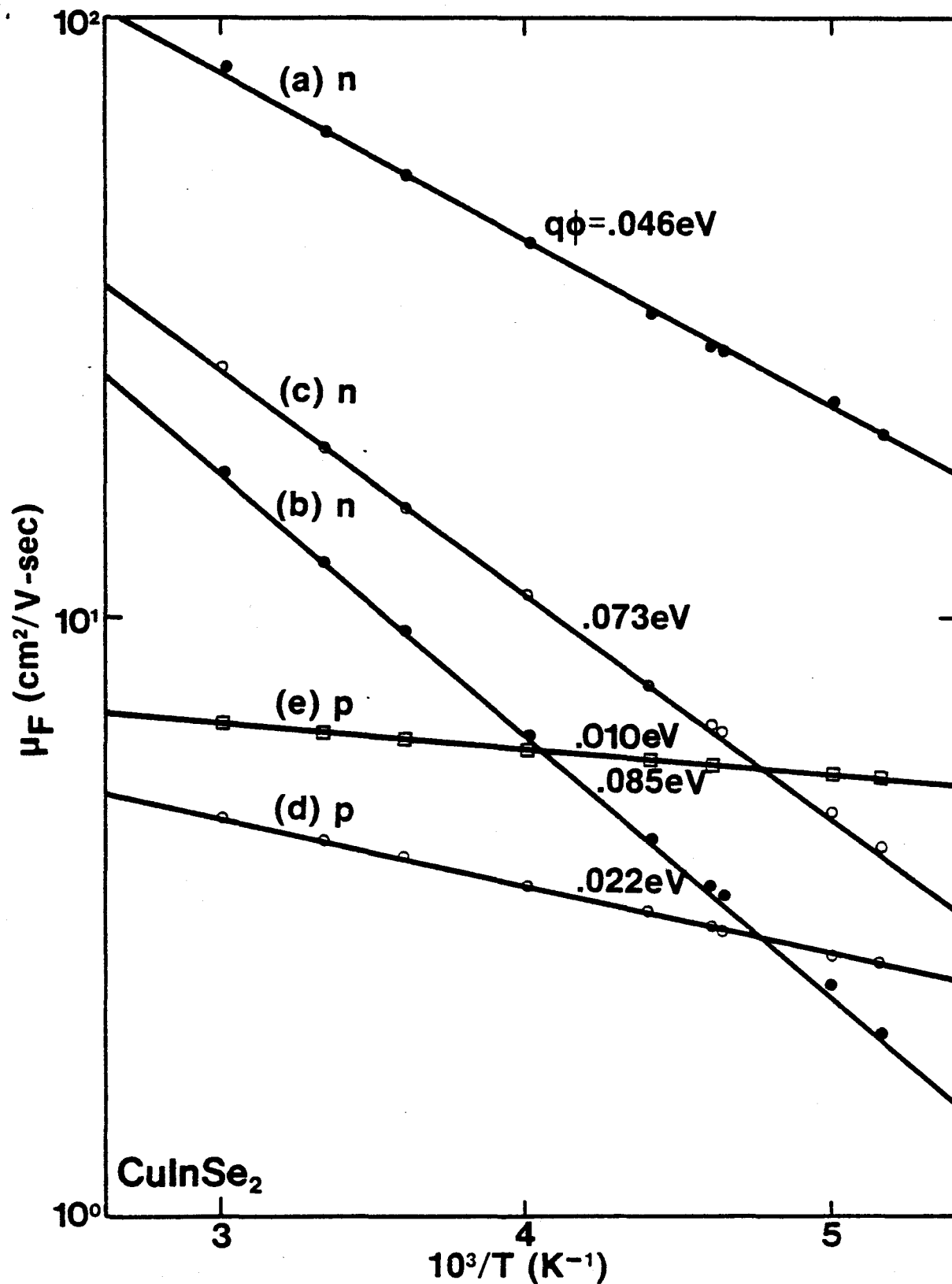
Fig. 3-29 Hall mobility of CuInSe$_2$ films dependence on inverse temperature for various substrate temperatures: (a) 500 K, annealed 15 min. in Ar; (b) as-deposited film, processed as in (a); (c) 520 K, as-deposited; (d) 520 K, annealed 15 min. in Ar/H$_2$Se; (e) 520 K, annealed 80 min. in Ar/H$_2$Se. Annealing temperature, 700 K (from Kazmerski et al. [91]).
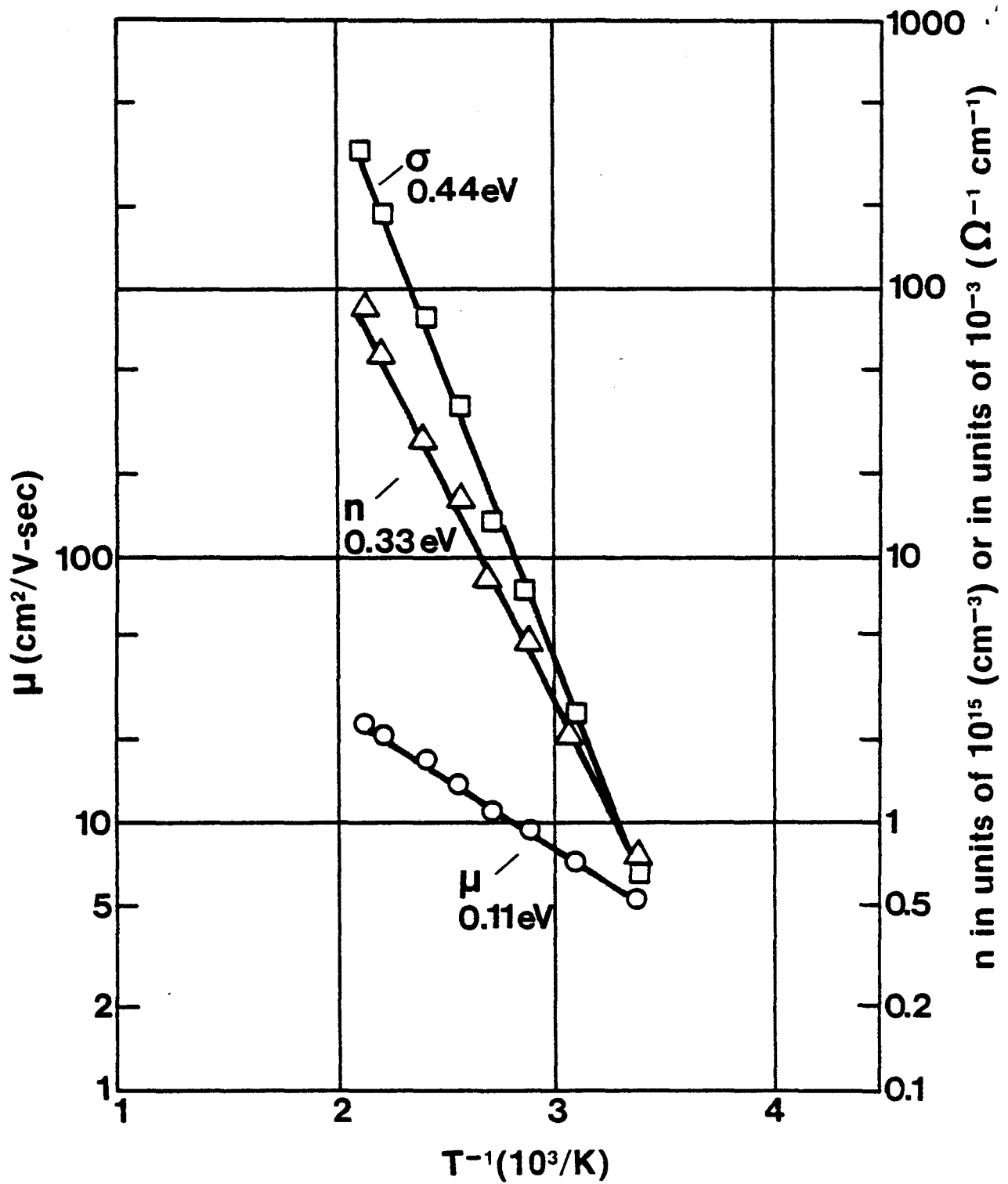
Fig. 3-30 Effective Hall mobility, free carrier concentration and conductivity of a CdS film as a function of reciprocal temperature (from Mankarious [90]).
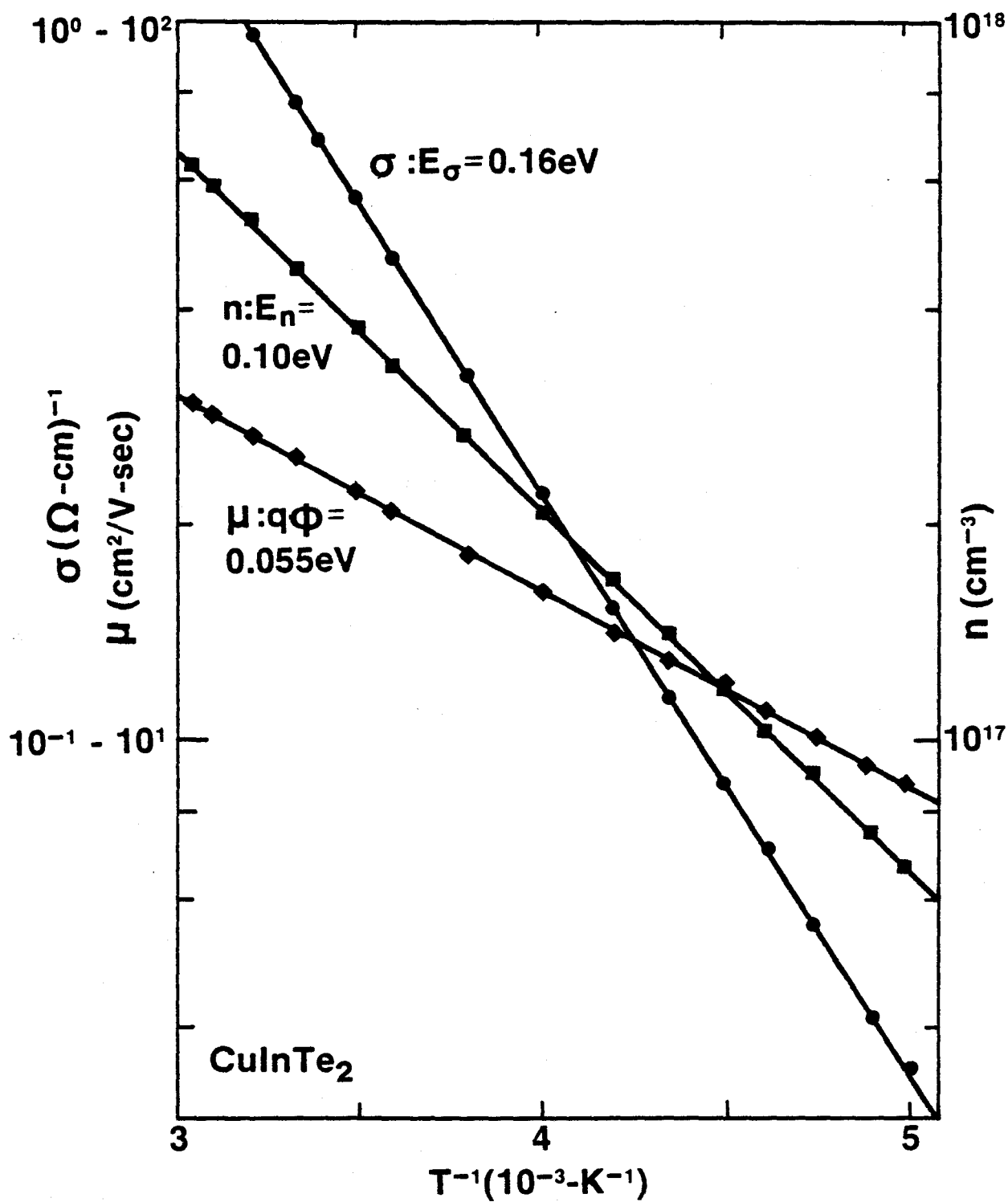
Fig. 3-31 Inverse temperature dependence of Hall mobility, conductivity, and carrier concentration for a p-type, annealed CuInTe$_2$ thin film. Substrate temperature is 473 K; thickness, 0.5 μm (from Kazmerski and Juang [93]).
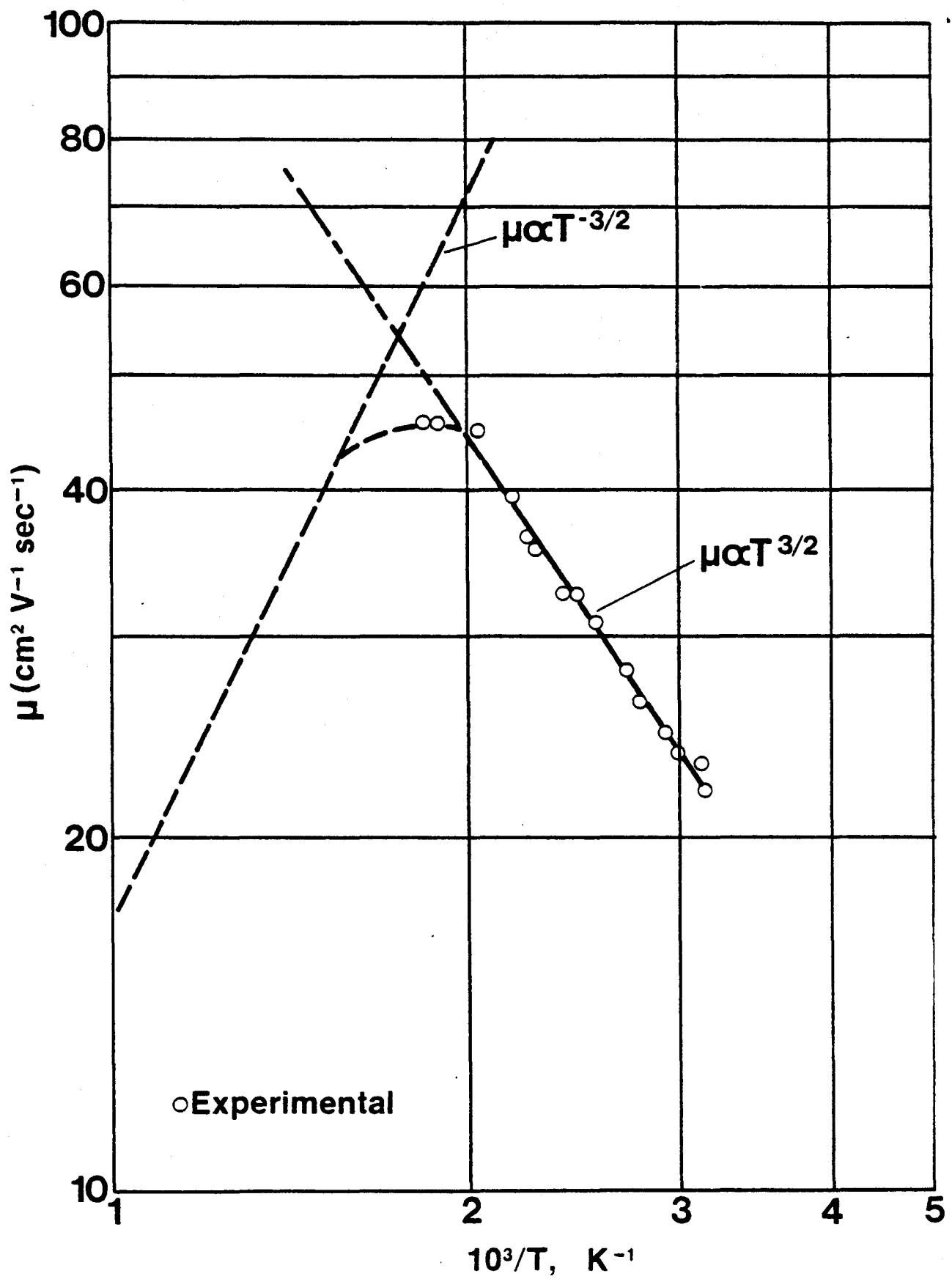
Fig. 3-32 Mobility variation as a function of temperature for CdS thin film at elevated temperatures, indicating lattice scattering ($\sim T^{-3/2}$) and impurity scattering ($\sim T^{3/2}$) regimes (from Mankarious [90]).
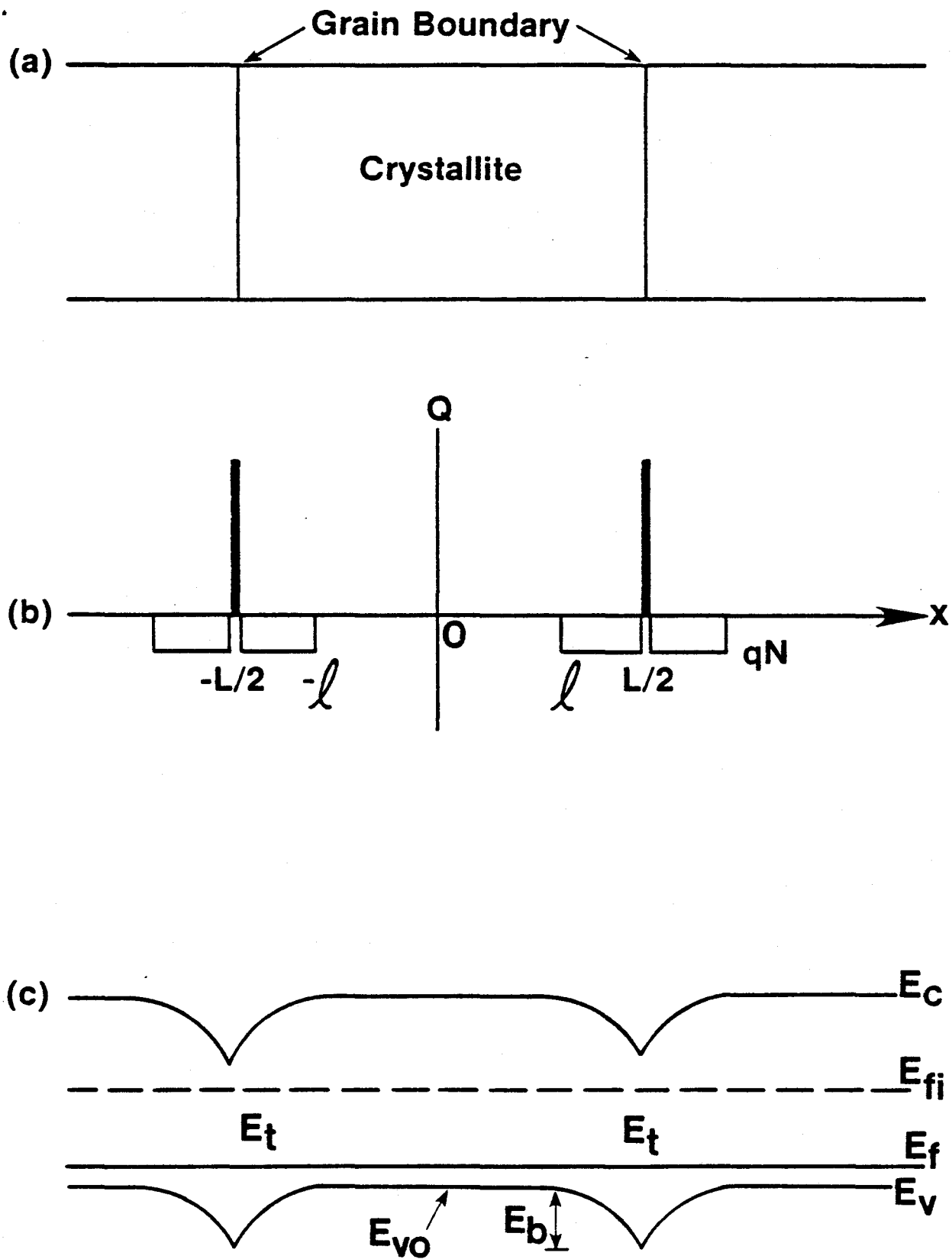
Fig. 3-33 Model for structure of polycrystalline film: (a) generalized structure, (b) charge distribution, and (c) energy band structure (from Seto [160]).
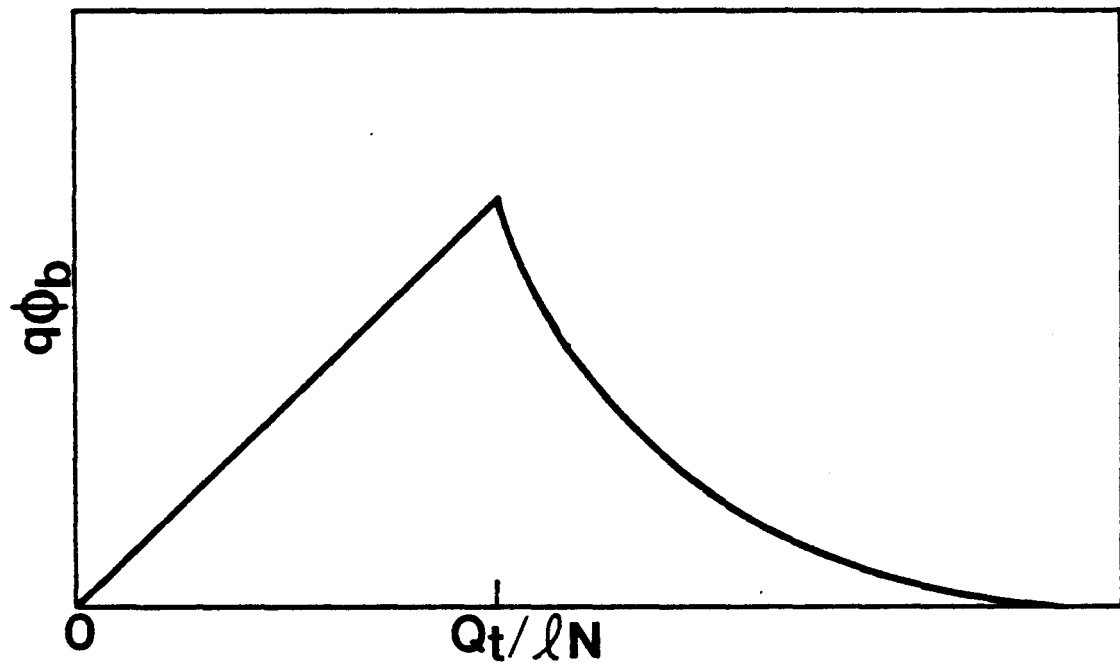
Fig. 3-34 Functional dependence of the potential barrier height on doping
concentration (from Seto [160]).
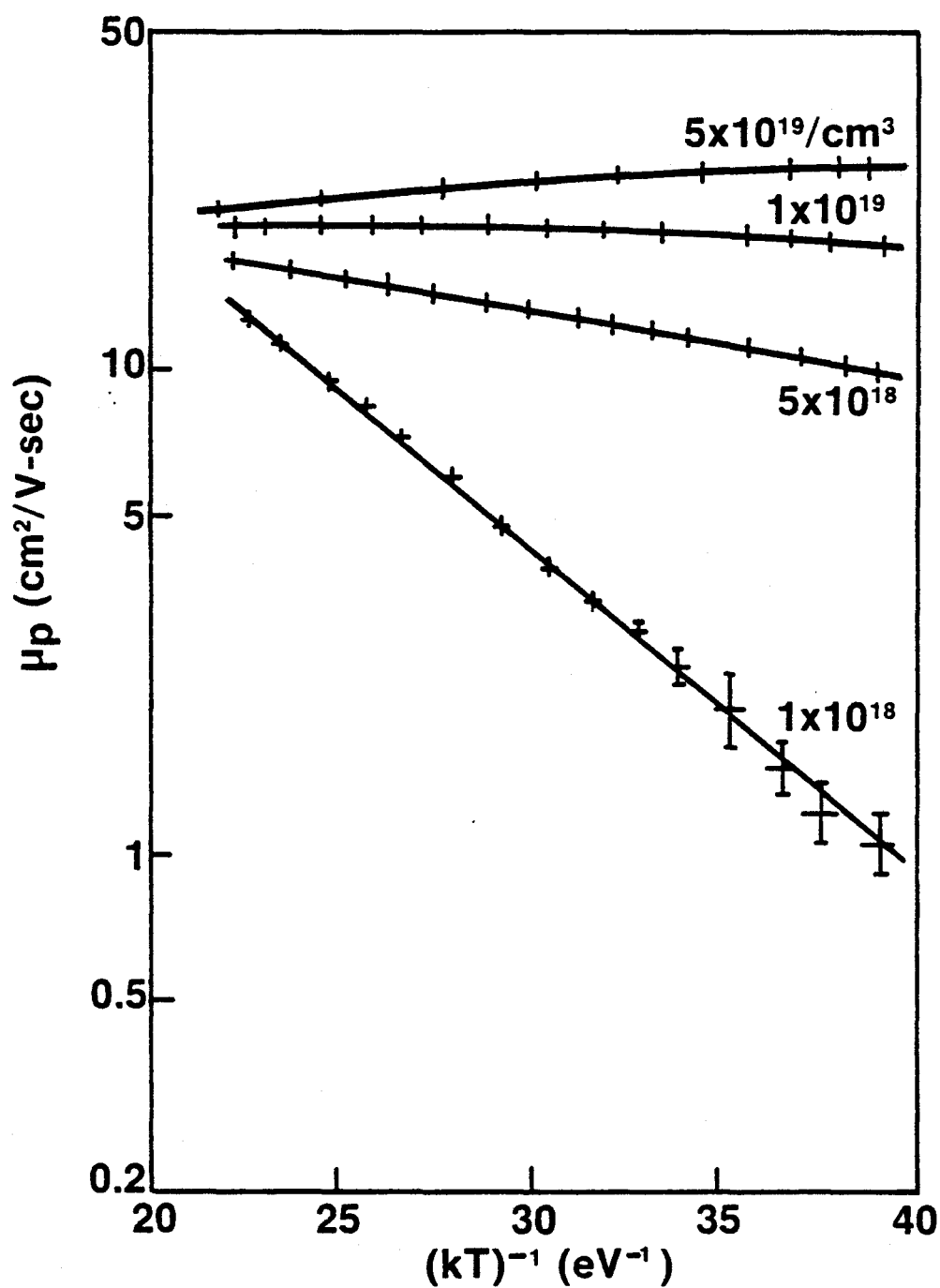
Fig. 3-35 Film Hall mobility as a function of inverse temperature for various doping concentrations in polycrystalline Si (from Seto [160]).
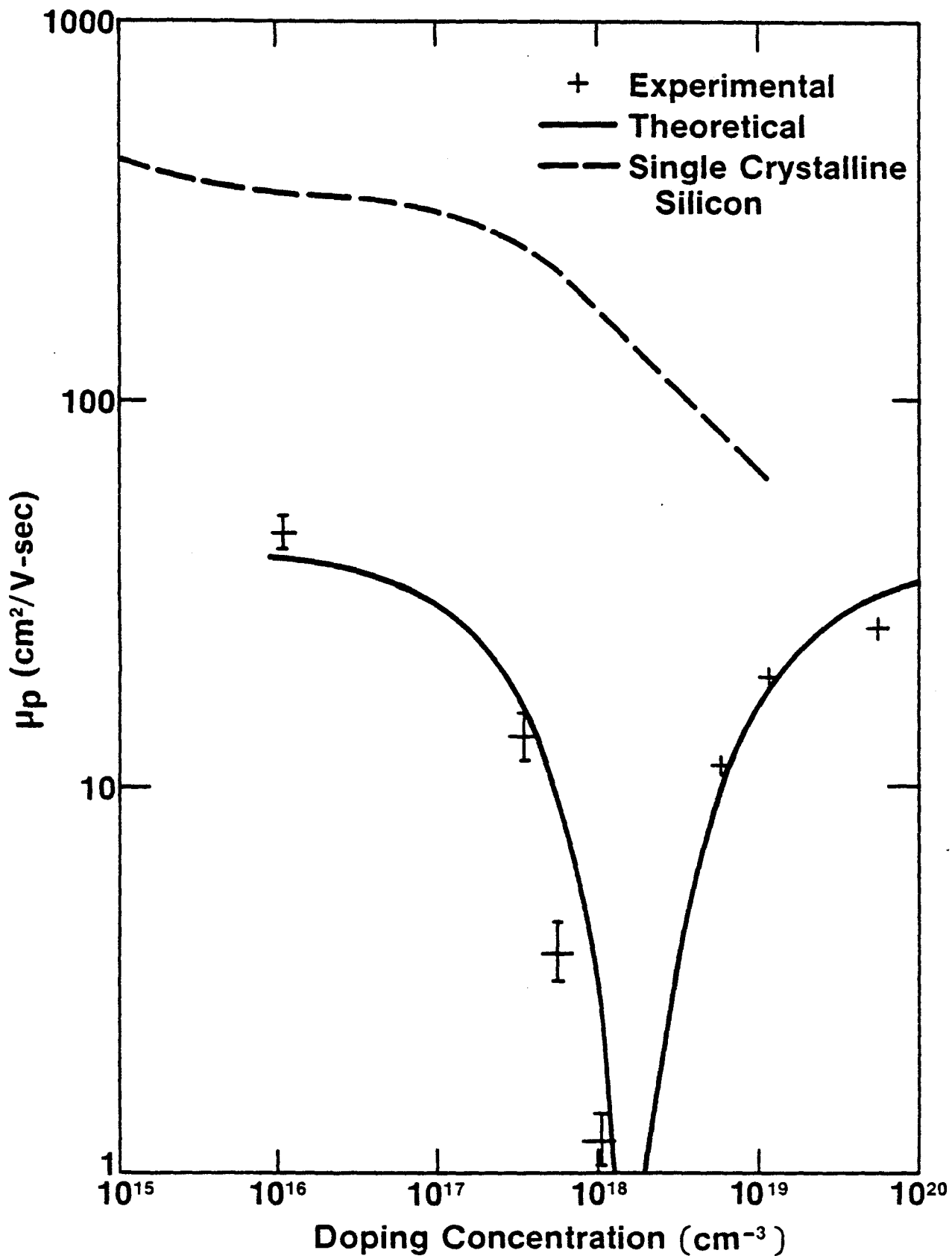
Fig. 3-36 Room-temperature Hall mobility versus doping concentration for p-type polycrystalline Si. The experimental results are compared with the theoretical solid curve. The broken line is for single crystal silicon (from Seto [160]).
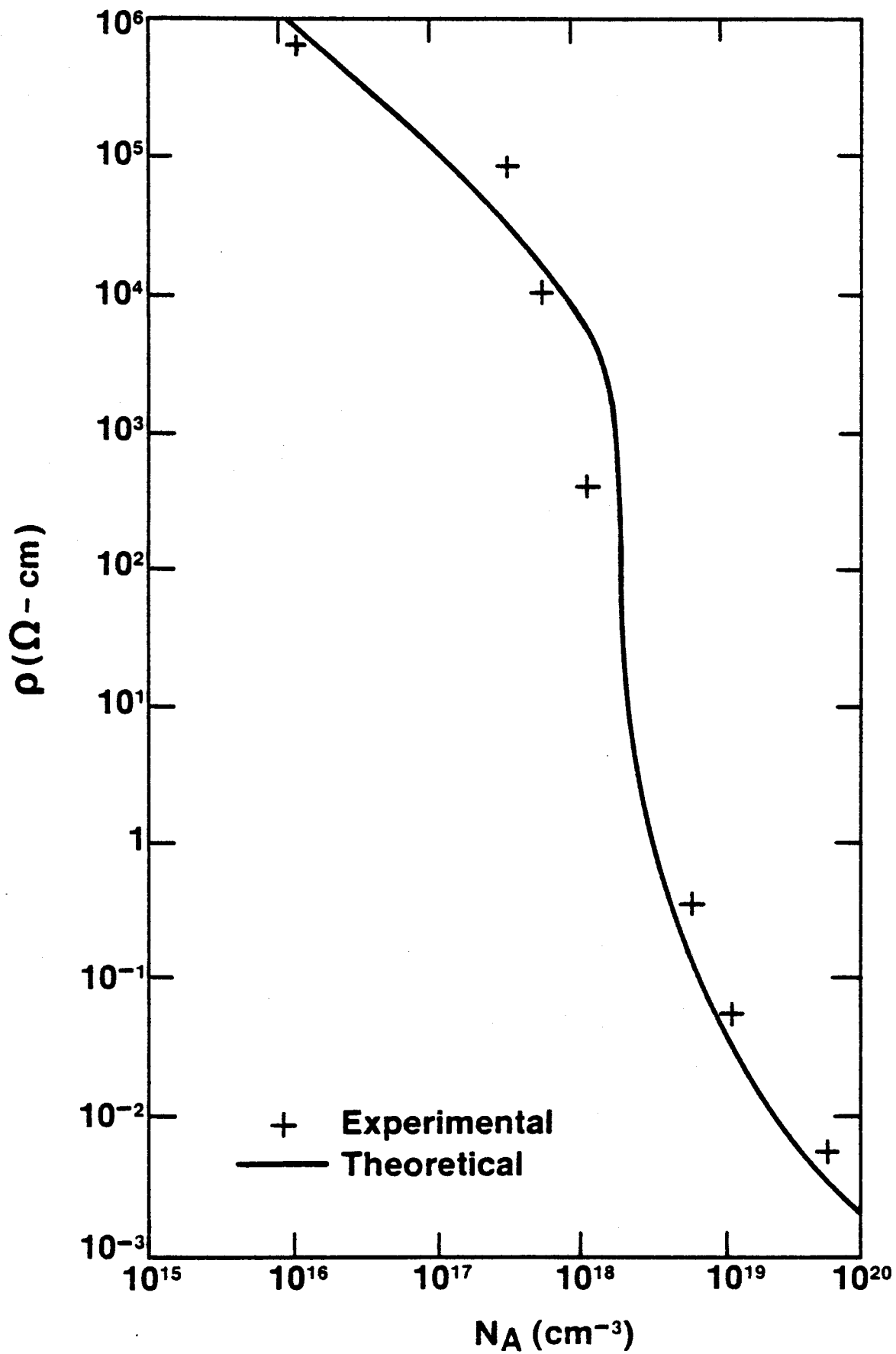
Fig. 3-38 Room-temperature resistivity as a function of doping concentration for polycrystalline Si. The solid line represents the theoretical analysis (from Seto [160]).
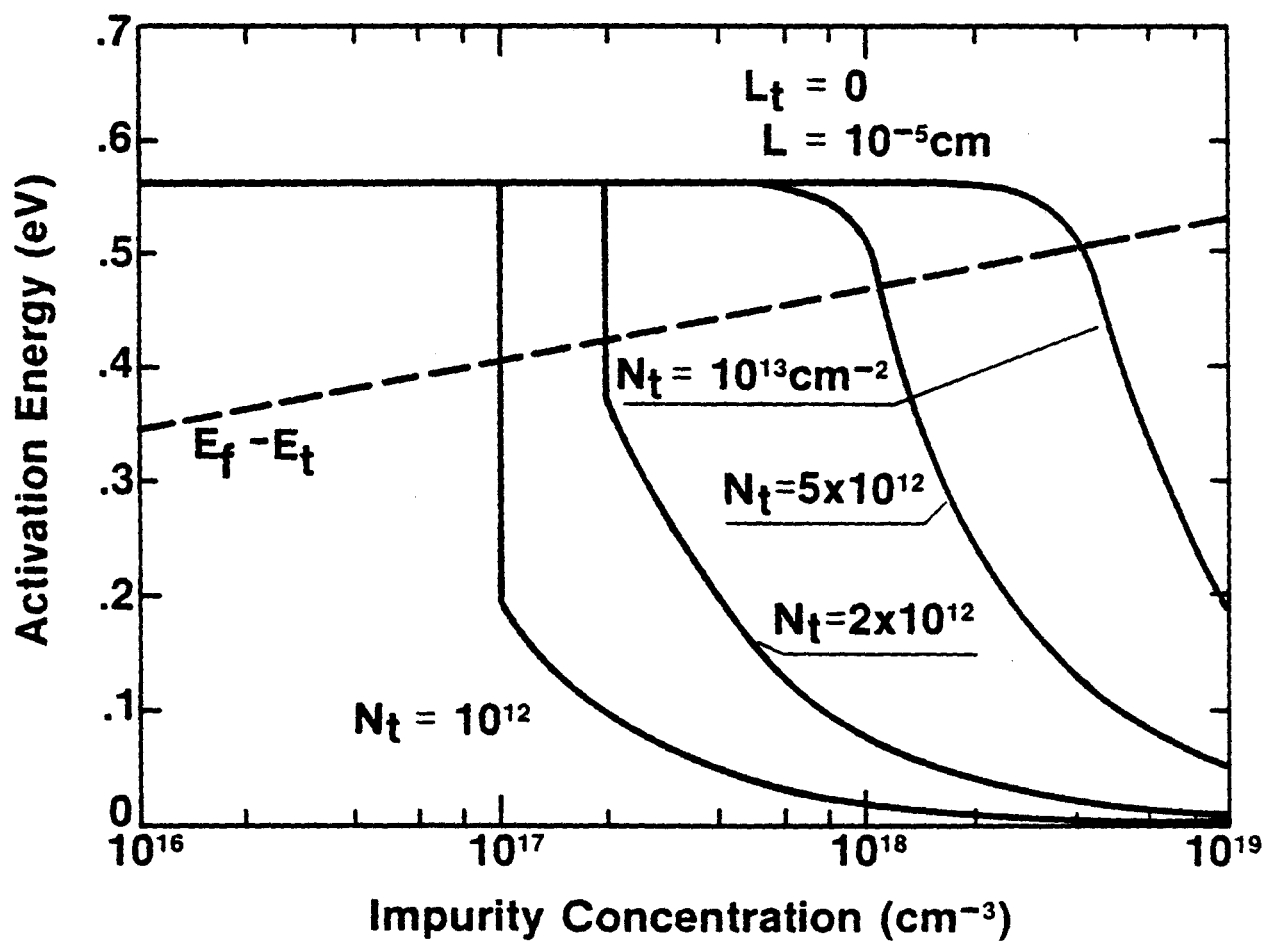
Fig. 3-39 Activation energy as a function of impurity concentration for polycrystalline Si (grain size = 10^{-5} cm). Reference is made to monovalent trapping states at midgap (from Baccarani et al. [164]).
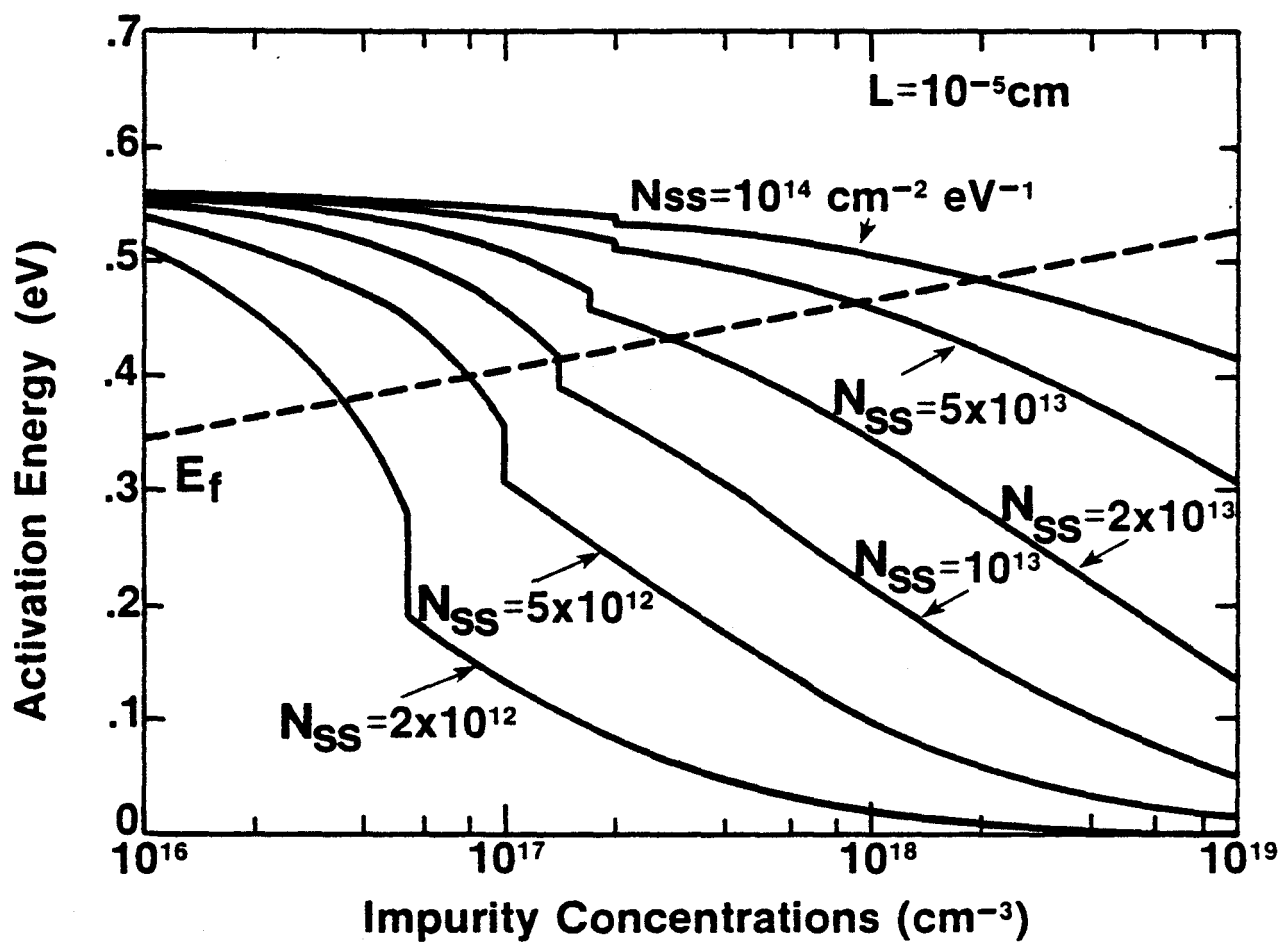
Fig. 3-40 Activation energy as a function of impurity concentration for polycrystalline Si (grain size = 10^{-5} cm). Reference is made to a distribution of interface states (from Baccarani et al. [164]).
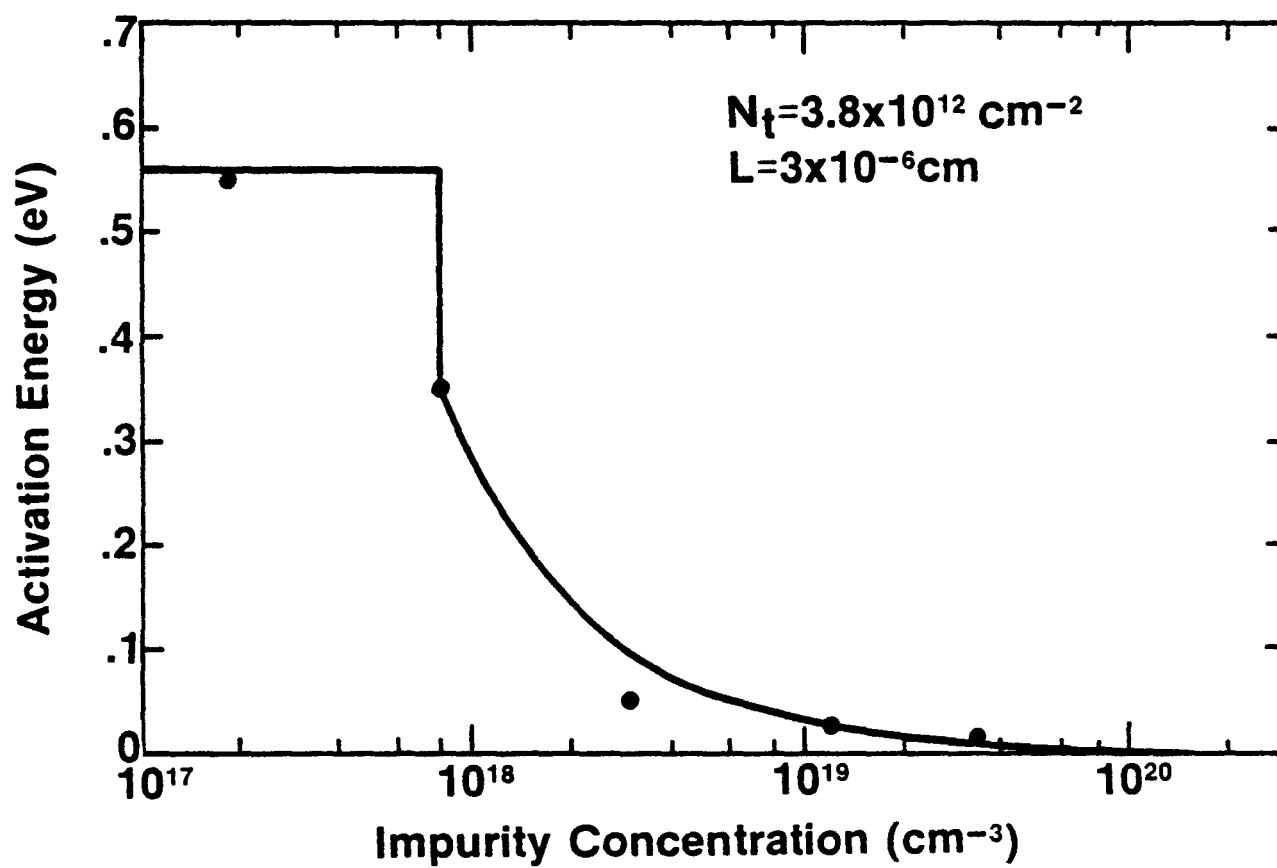
Fig. 3-41   Theoretical and experimental activation energy as a function of impurity concentration in polycrystalline Si (from Baccarani et al. [164]).
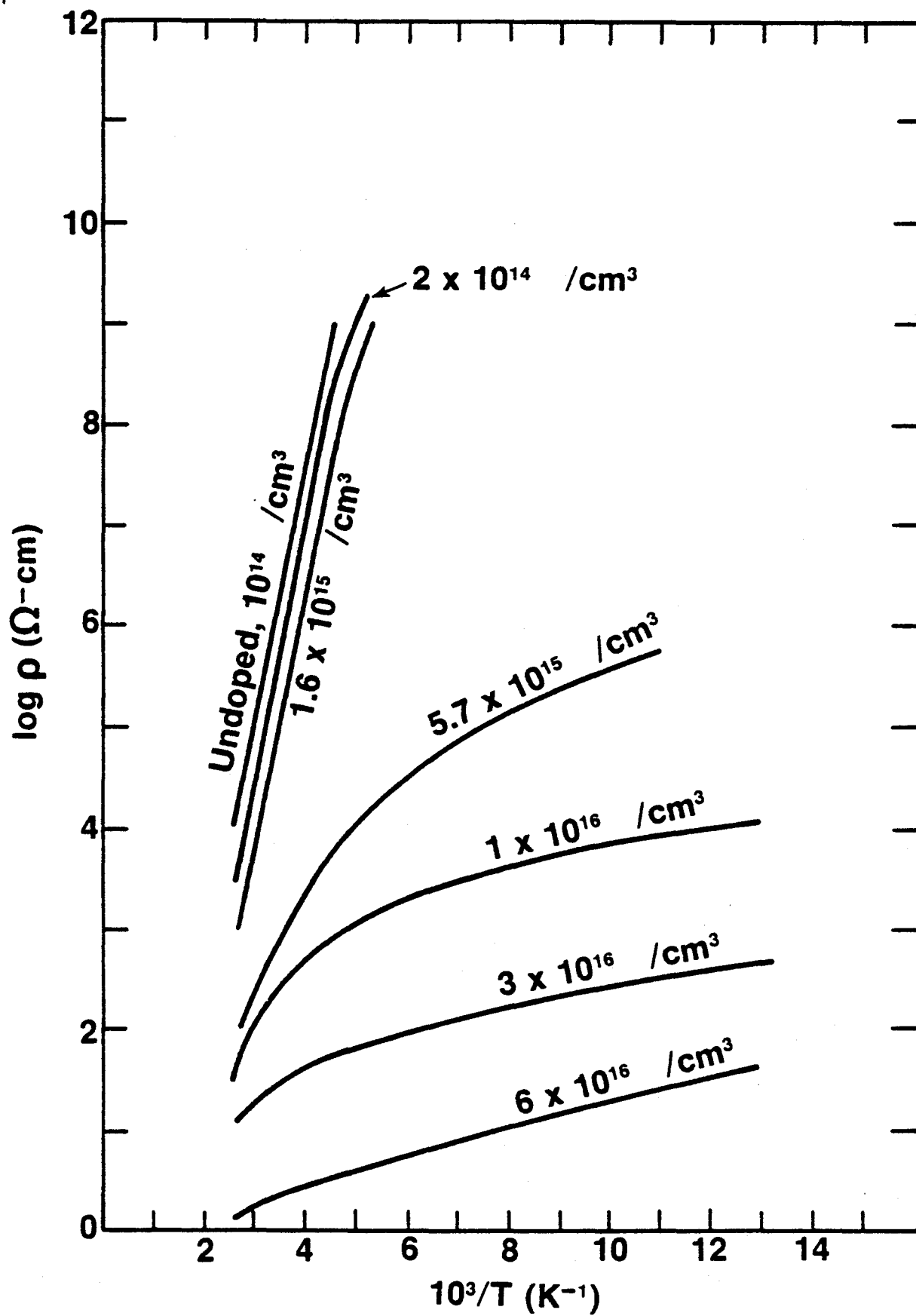
Fig. 3-42 Log resistivity versus inverse temperature for neutron transmutation doped polycrystalline silicon (from Seager and Castner [165]).
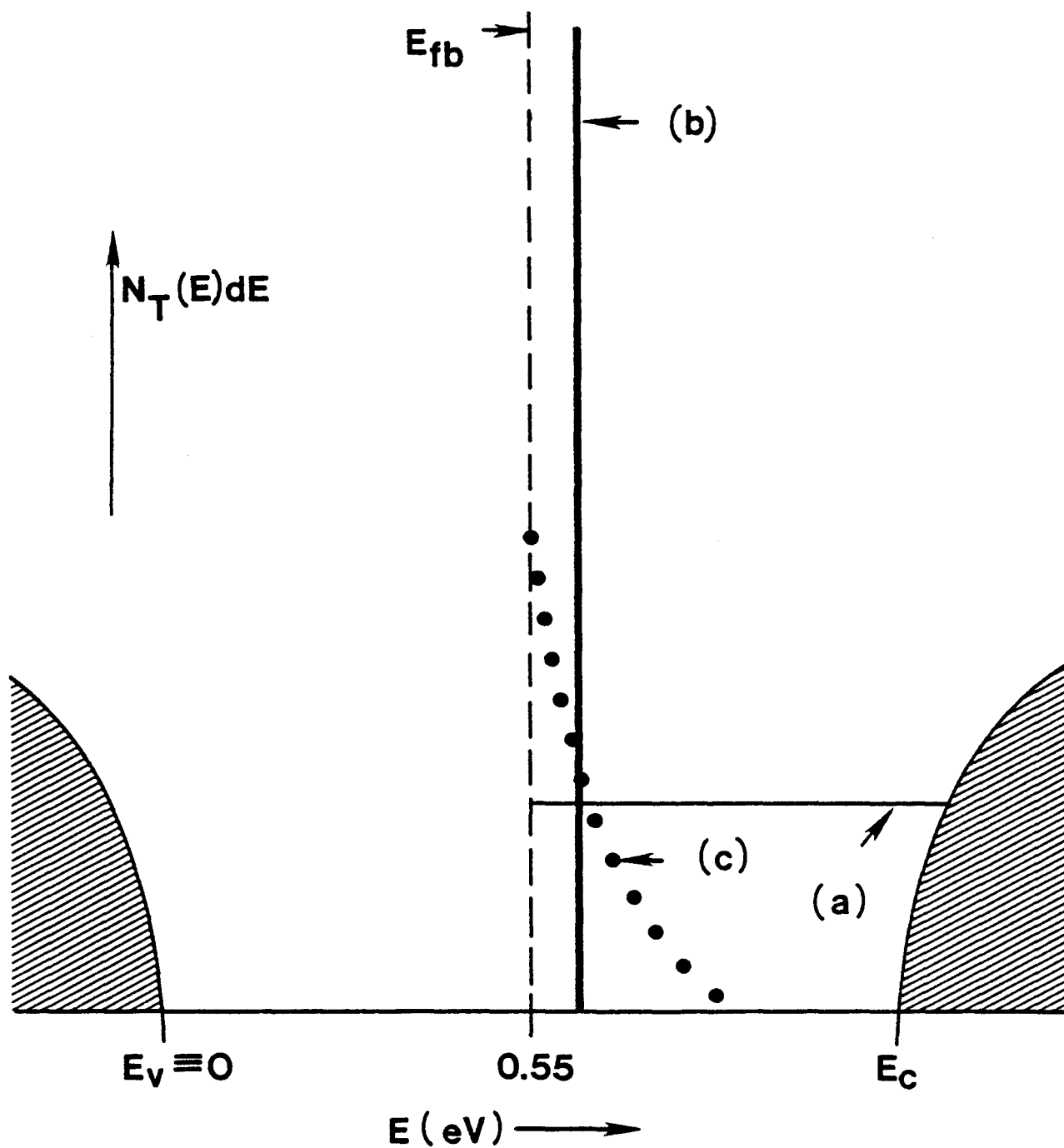
Fig. 3-43   The densities of states and Fermi level in barrier region for polycrystalline Si: (a) $N_t = 3.3 \times 10^{12}/cm^2$-eV;   (b) $N_t = 5.4 \times 10^{11}/cm^2$-eV at 0.626 eV above E_v and zero elsewhere;   (c) $N_t = (1.89 \times 10^{15}/cm^2$-eV) exp(-E/0.099eV) (from Seager and Castner [165]).
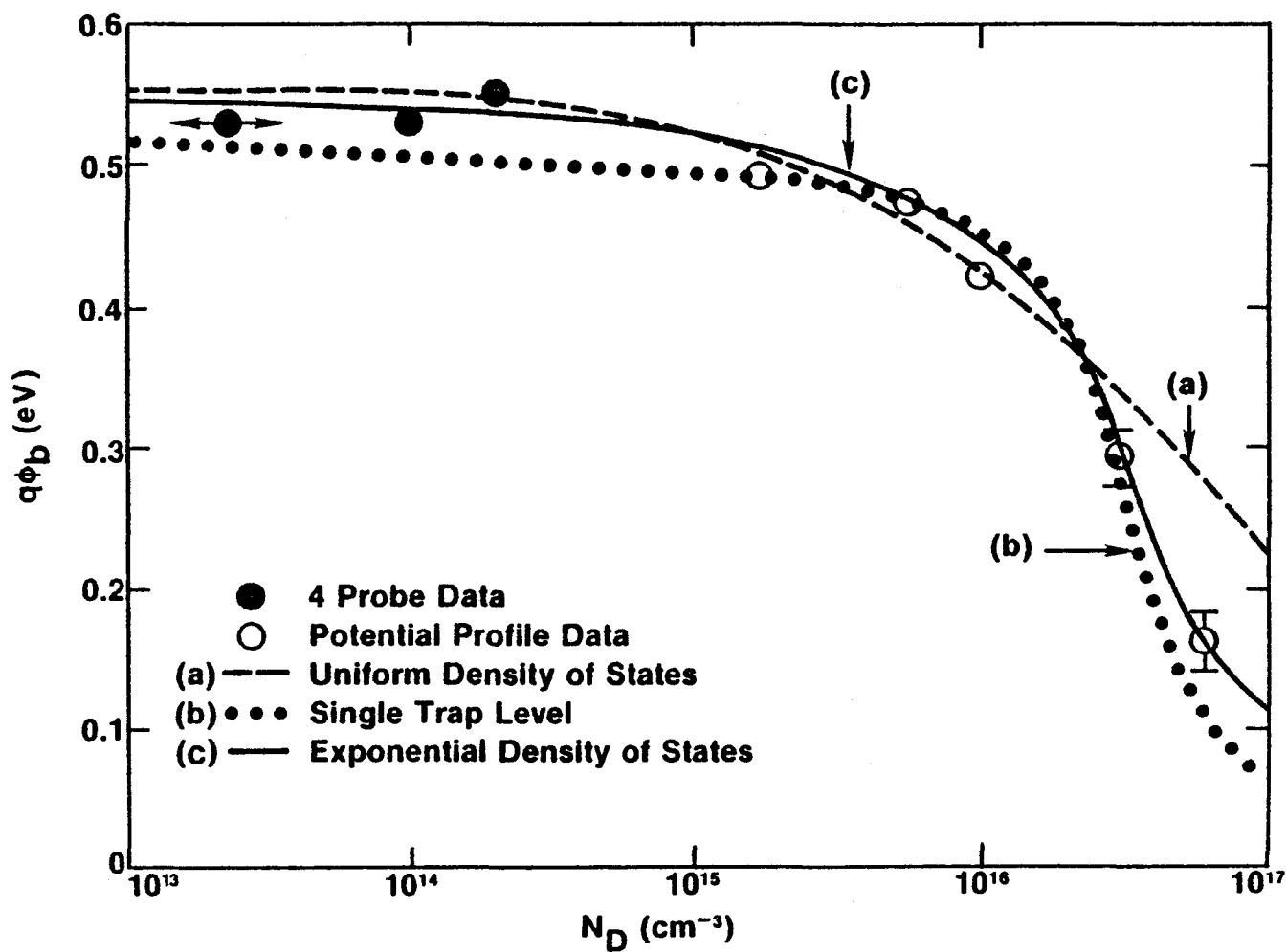
Fig. 3-44 The largest grain boundary barrier heights (T=0) as a function of doping density for neutron transmutation doped polycrystalline silicon. Open circles are data from small-area potential profile experiments and solid circles are four-probe resistivity data (from Seager and Castner [165]).
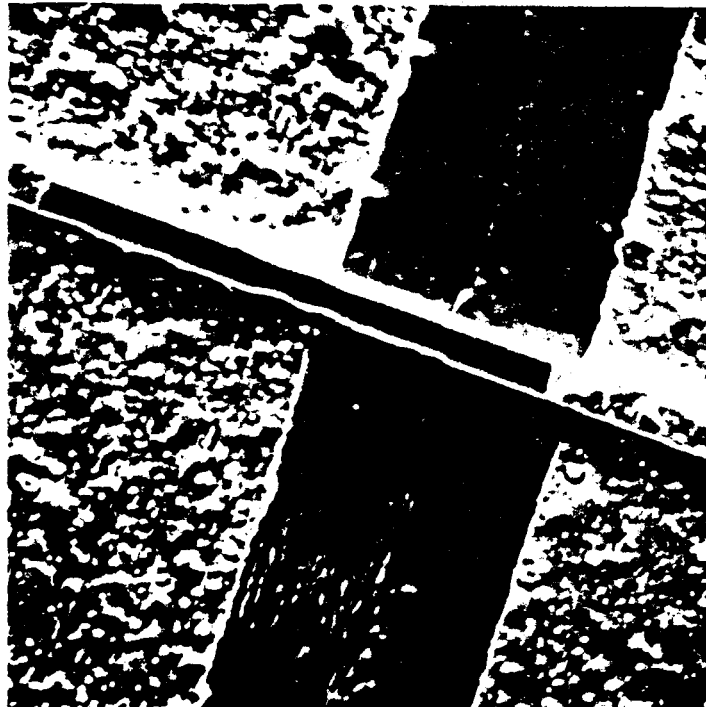
Fig. 3-45 Electron micrograph of a 20 μm long GaAs sample containing a single grain boundary (from Cohen et al. [183]).
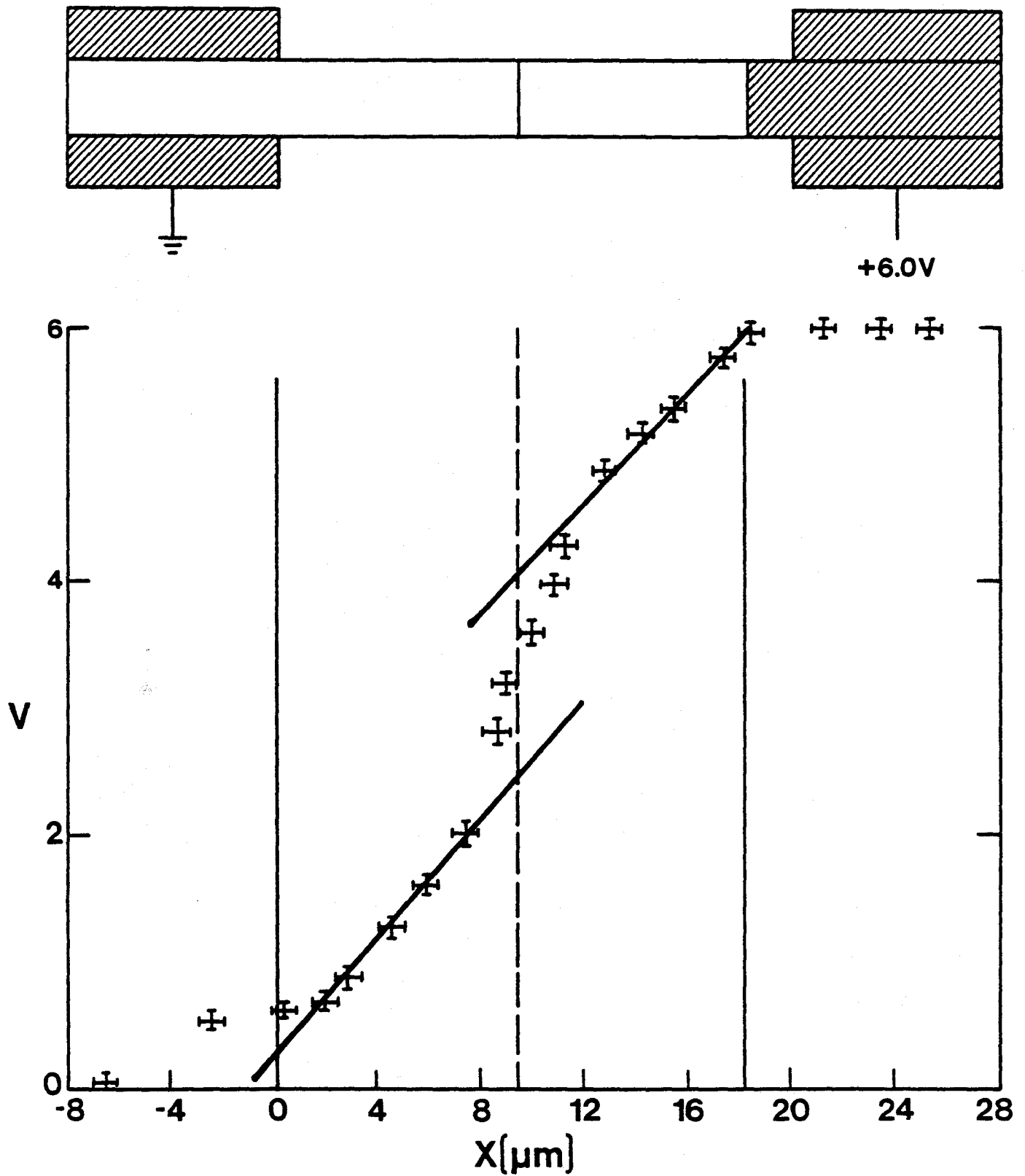
Fig. 3-46 Auger potential profile of a lightly-doped GaAs sample containing a single grain boundary (from Cohen et al. [183]).
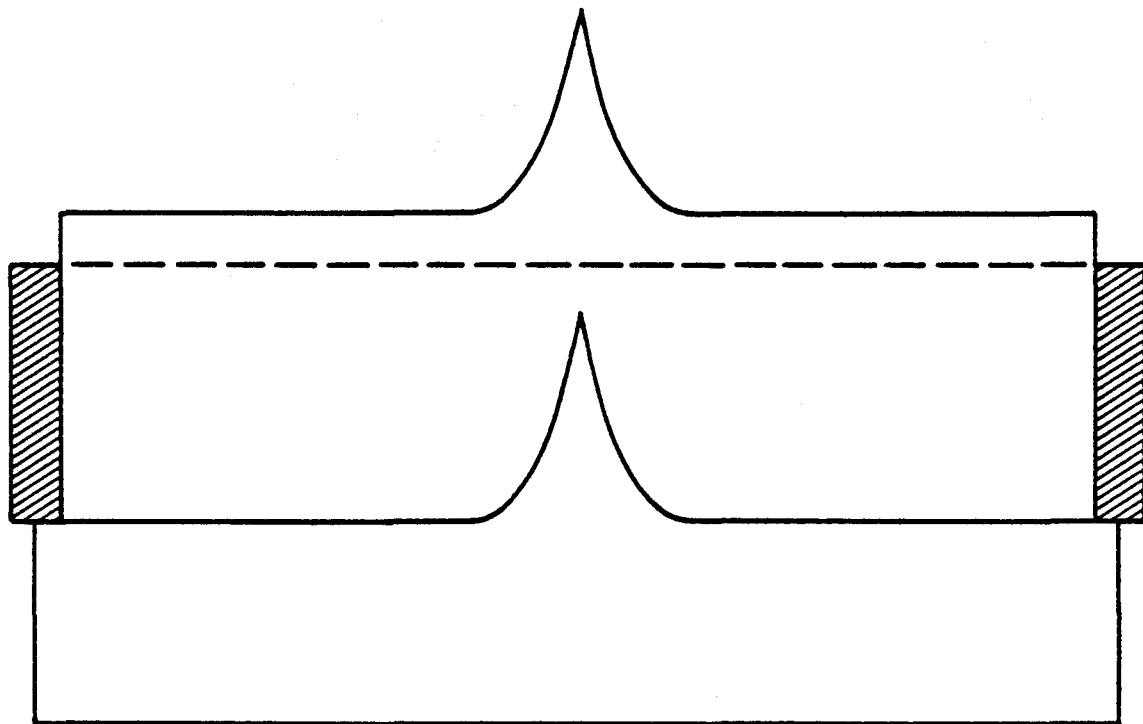
(a)
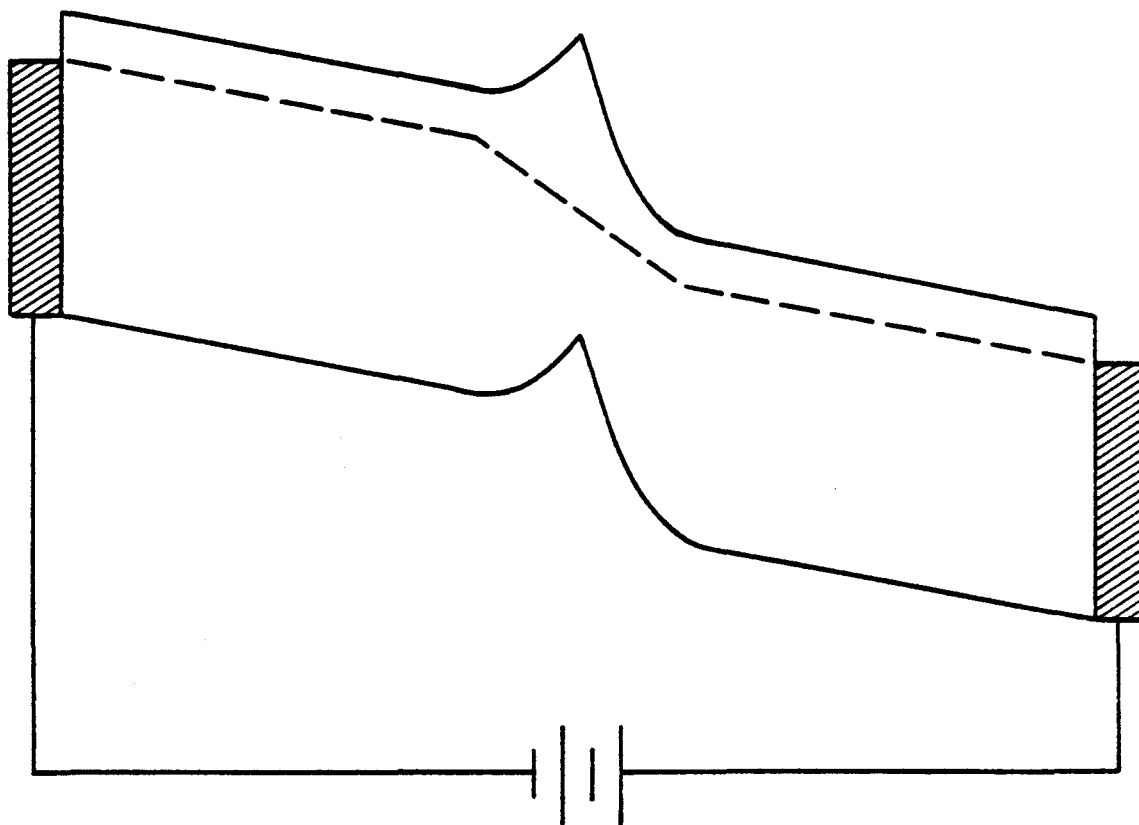
(b)

Fig. 3-47 Band diagram illustrating band-bending at grain boundary in GaAs:
(a) in equilibrium; (b) with applied voltage (from Cohen et al.
[183]).
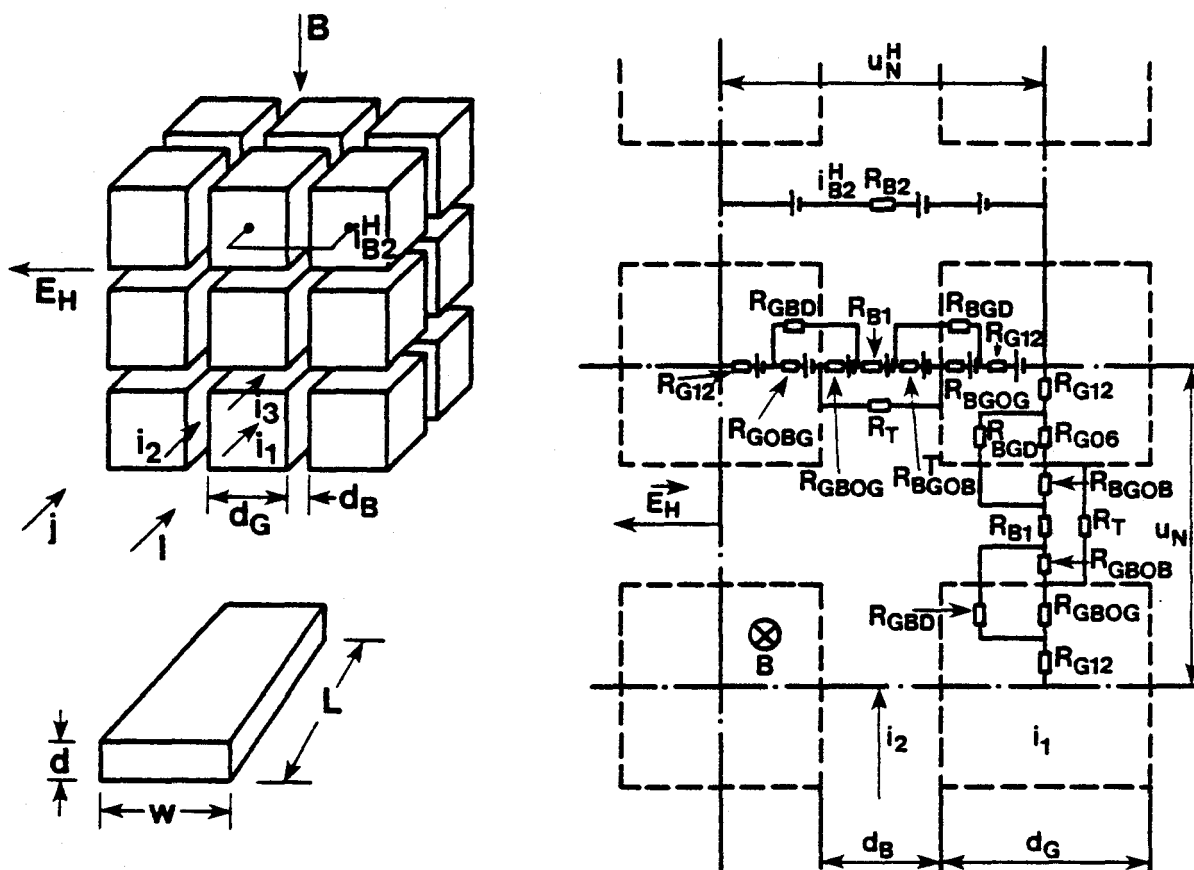
Fig. 3-48   Assumed structure of polycrystalline semiconductor for generalized
            Hall effect analysis and equivalent electrical circuits. Subscripts
            G, B, and b refer to grain, grain boundary and bulk, respectively (from
            Jerhot and Snejdar [187]).
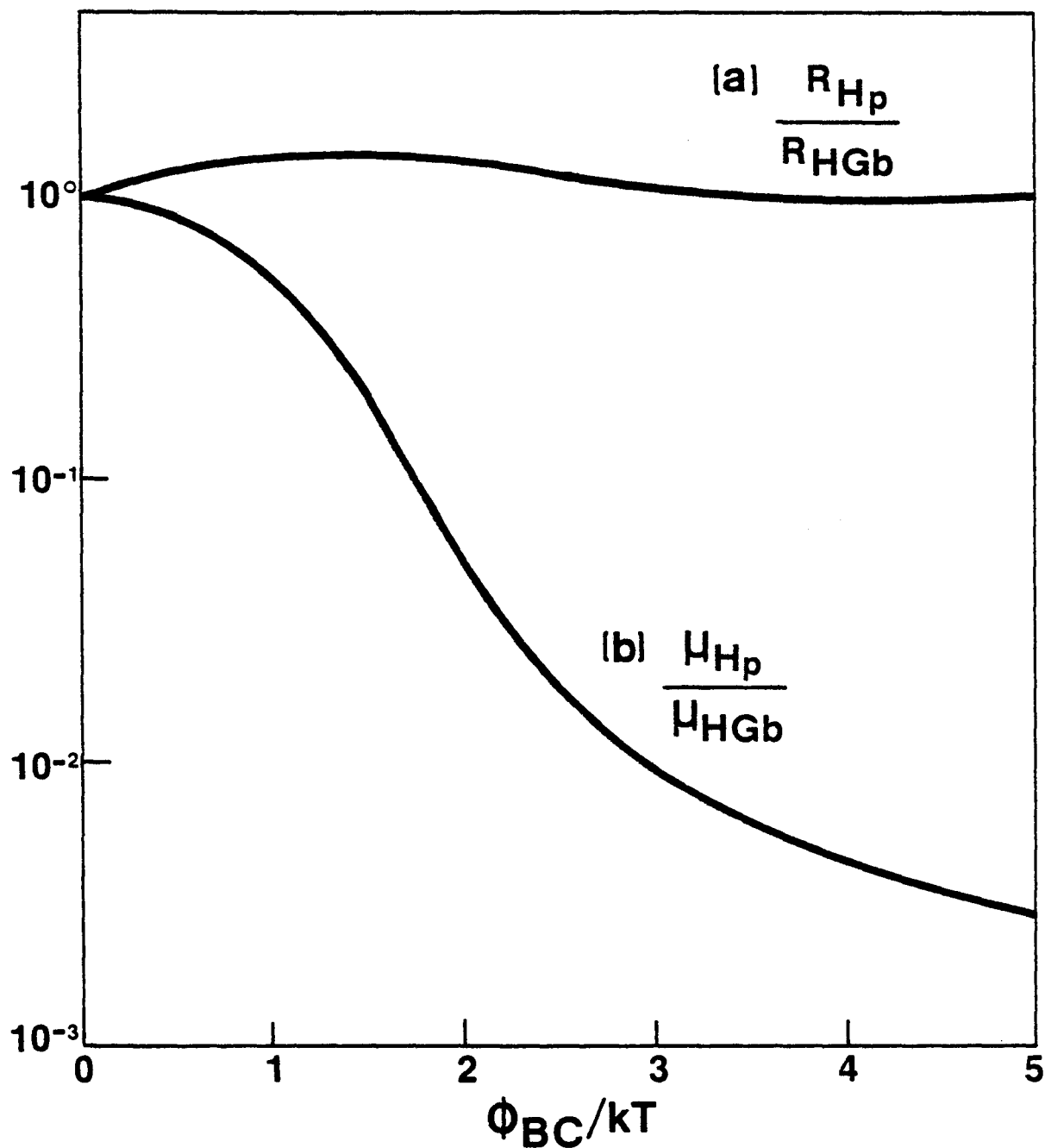
Fig. 3-49 Effect of barrier height on: (a) Hall coefficient, and (b) Hall mobility in polycrystalline semiconductor with n_b = $10^{16}/cm^3$, $\ell_1(=d_g)$ = 10^{-5} cm, $\ell_2(=d_b)$ = 10^{-7} cm, and μ_b = 10 cm^2/v-sec (from Jerhot and Snejdar [187]).
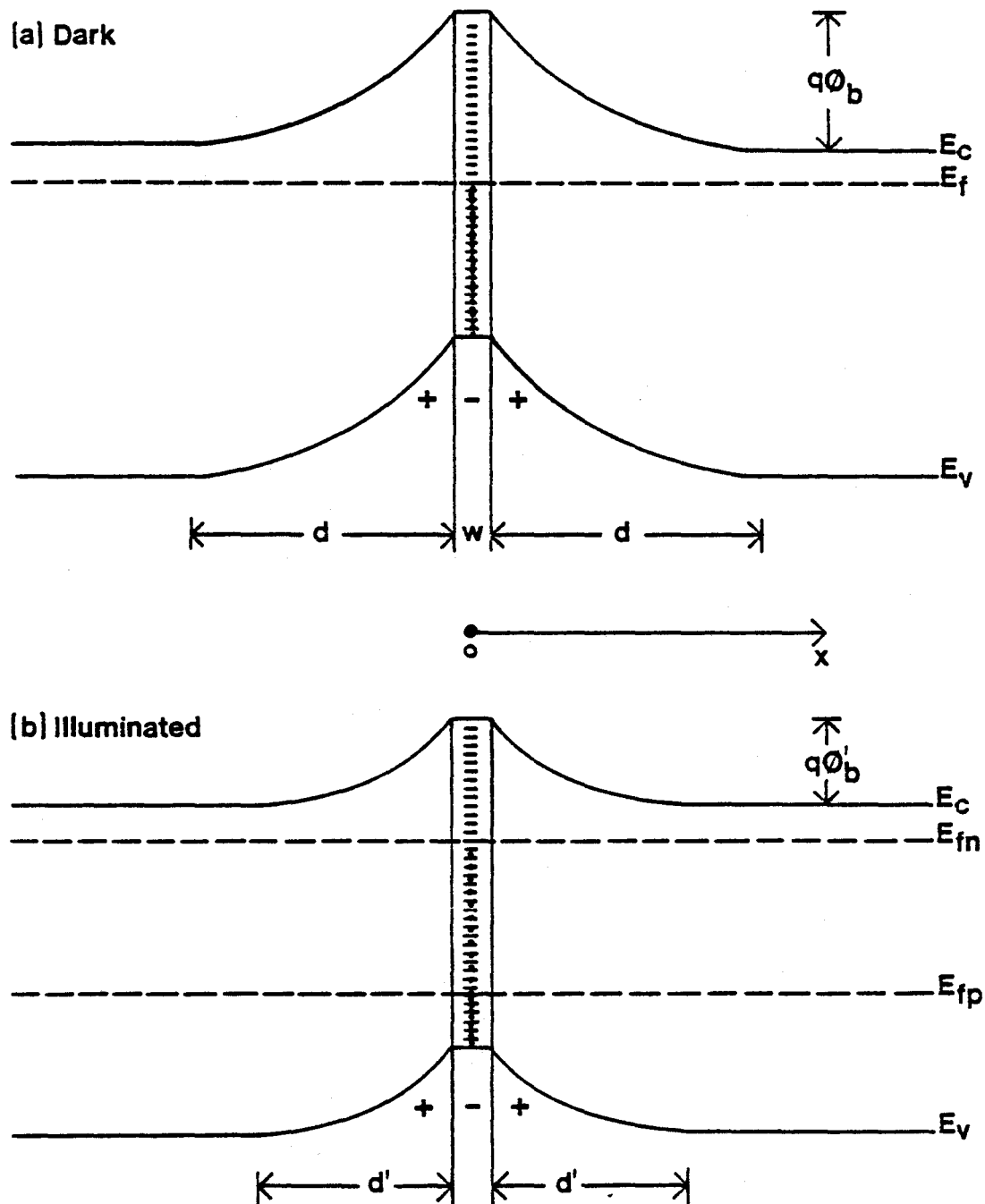
Fig. 3-50 Energy band diagram of the grain boundary region for an n-type semiconductor. (a) Dark case and (b) illuminated case. $q\phi_b$ and $q\phi_b'$ are the dark and light diffusion potentials, respectively (from Kazmerski [189]).
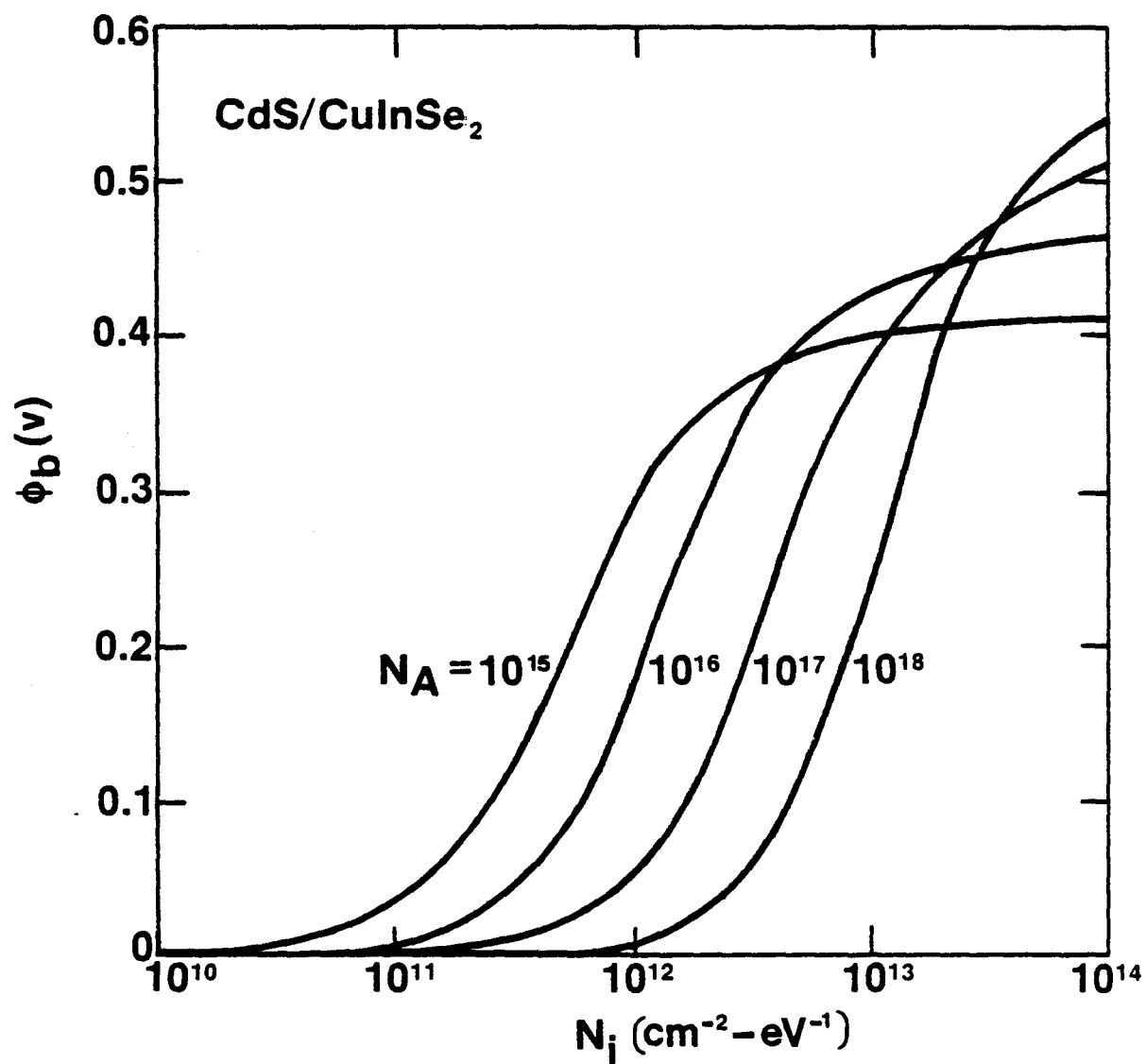
Fig. 3-51 Dark diffusion potential dependence on interface state density for various carrier concentrations in p-type CuInSe$_2$ (from Kazmerski [189]).
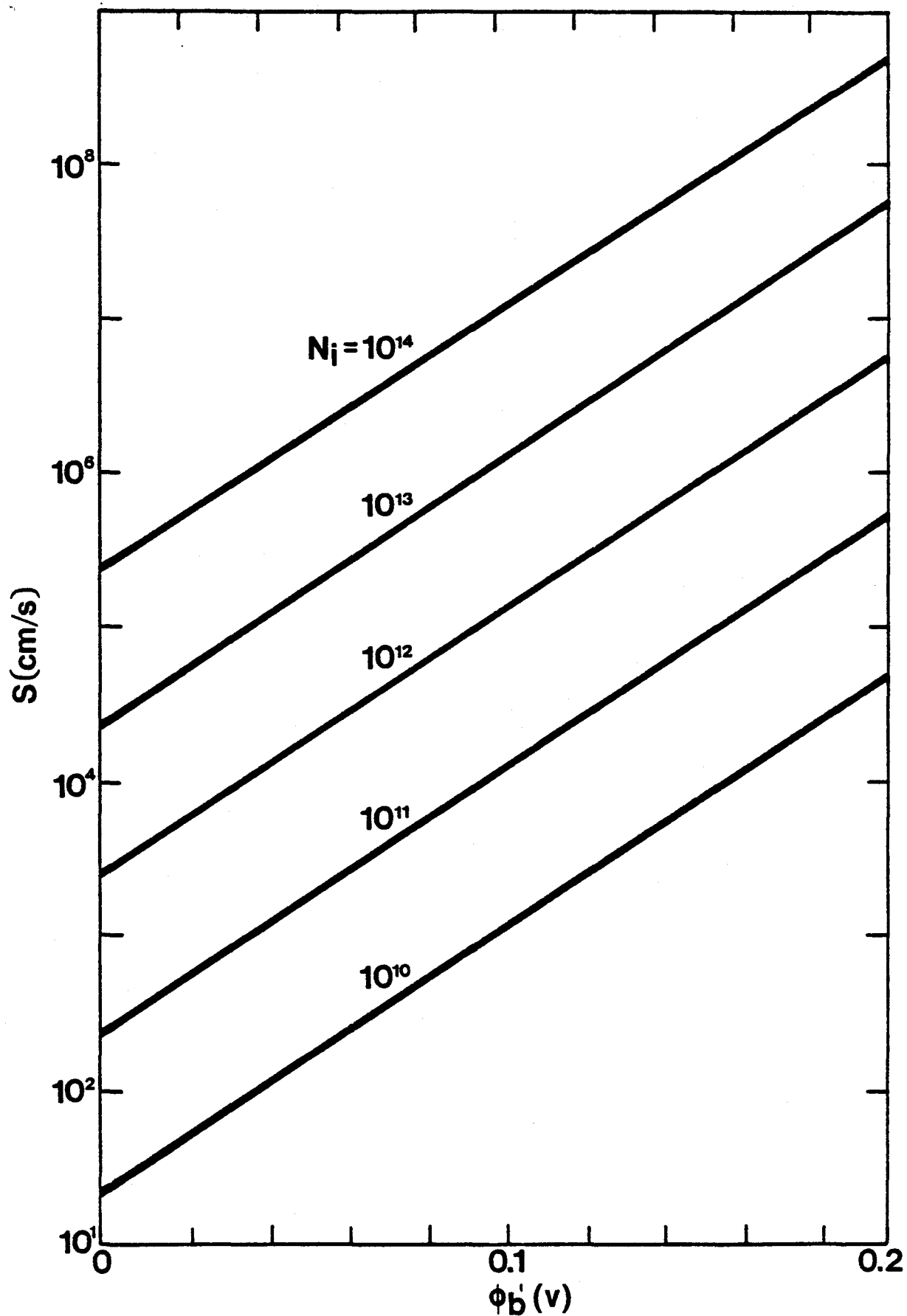
Fig. 3-52 Dependence of the recombination velocity upon the illuminated diffusion potential and interface state density in CuInSe$_2$ under 100 mW/cm^2 illumination (from Kazmerski [189]).
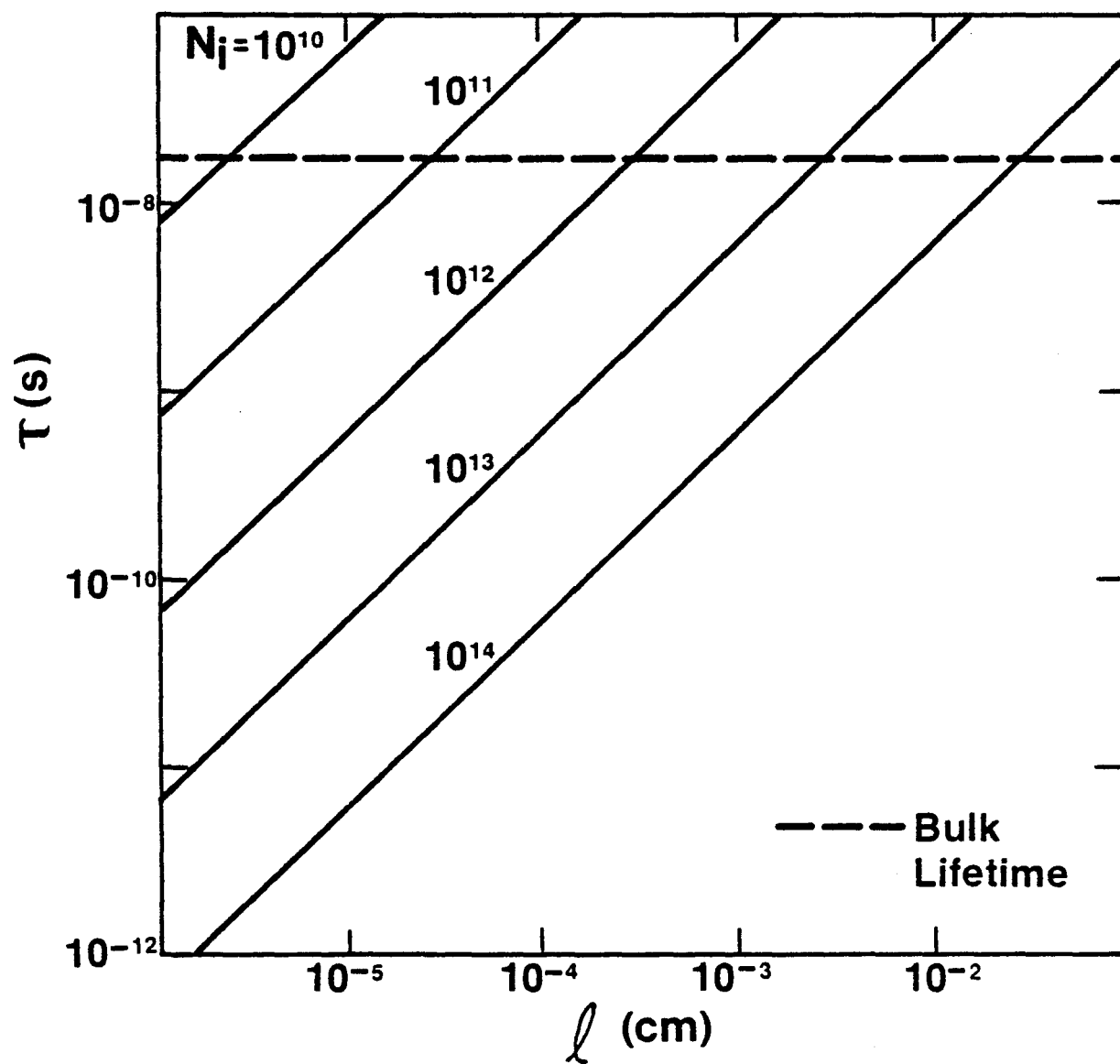
Fig. 3-53 Dependence of minority carrier lifetime on grain diameter for various interface state densities in $CuInSe_2$. Dashed line indicates single-crystal value of lifetime (from Kazmerski et al. [190]).
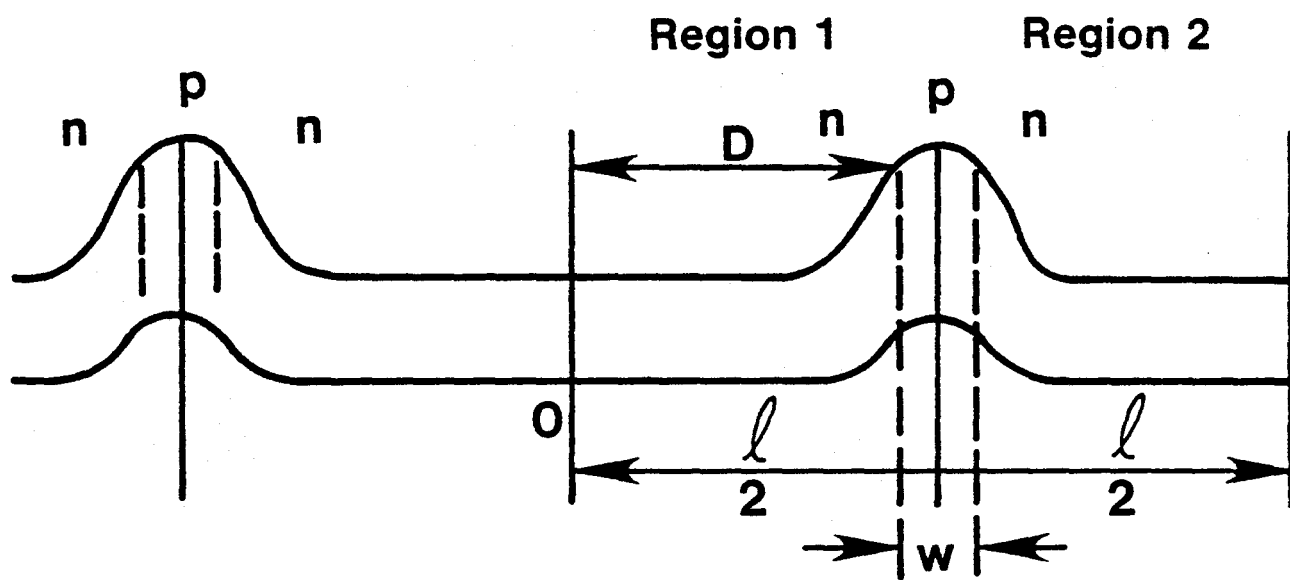
Fig. 3-54   Energy band model used in calculating minority carrier mobility for
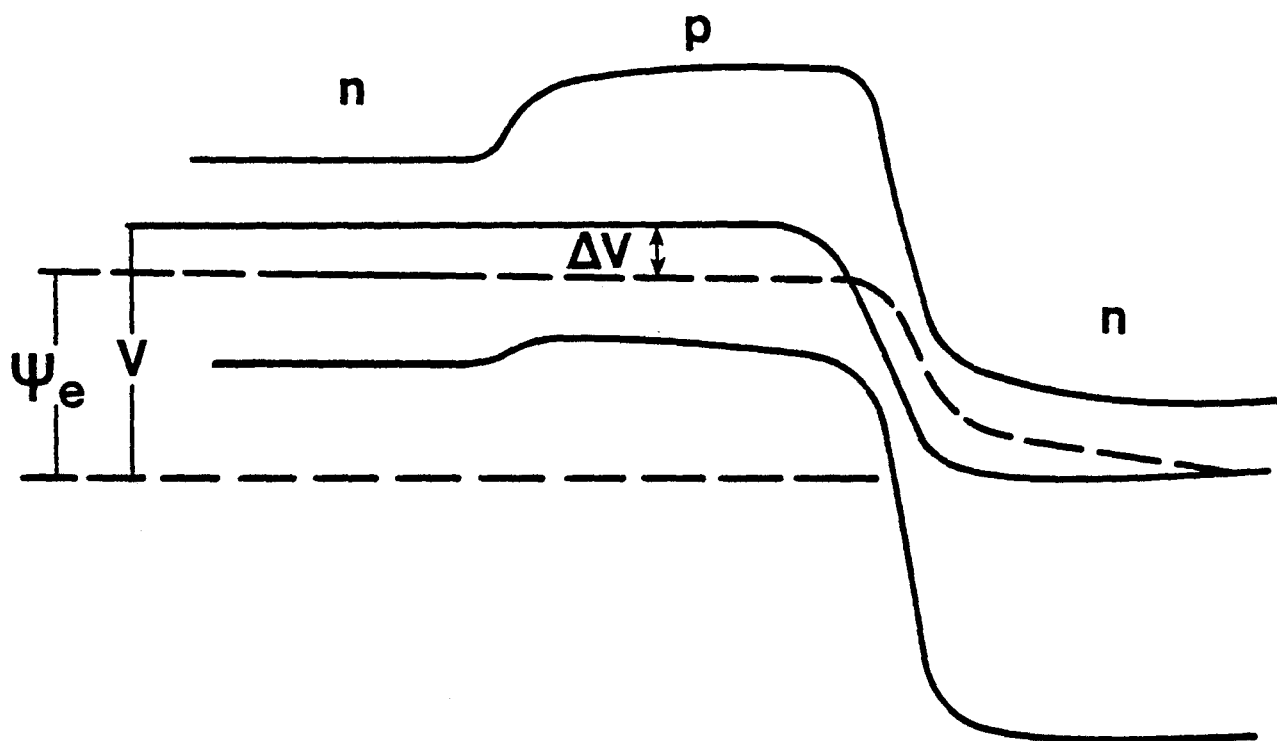an n-type polycrystalline thin film (from Yee [202]).

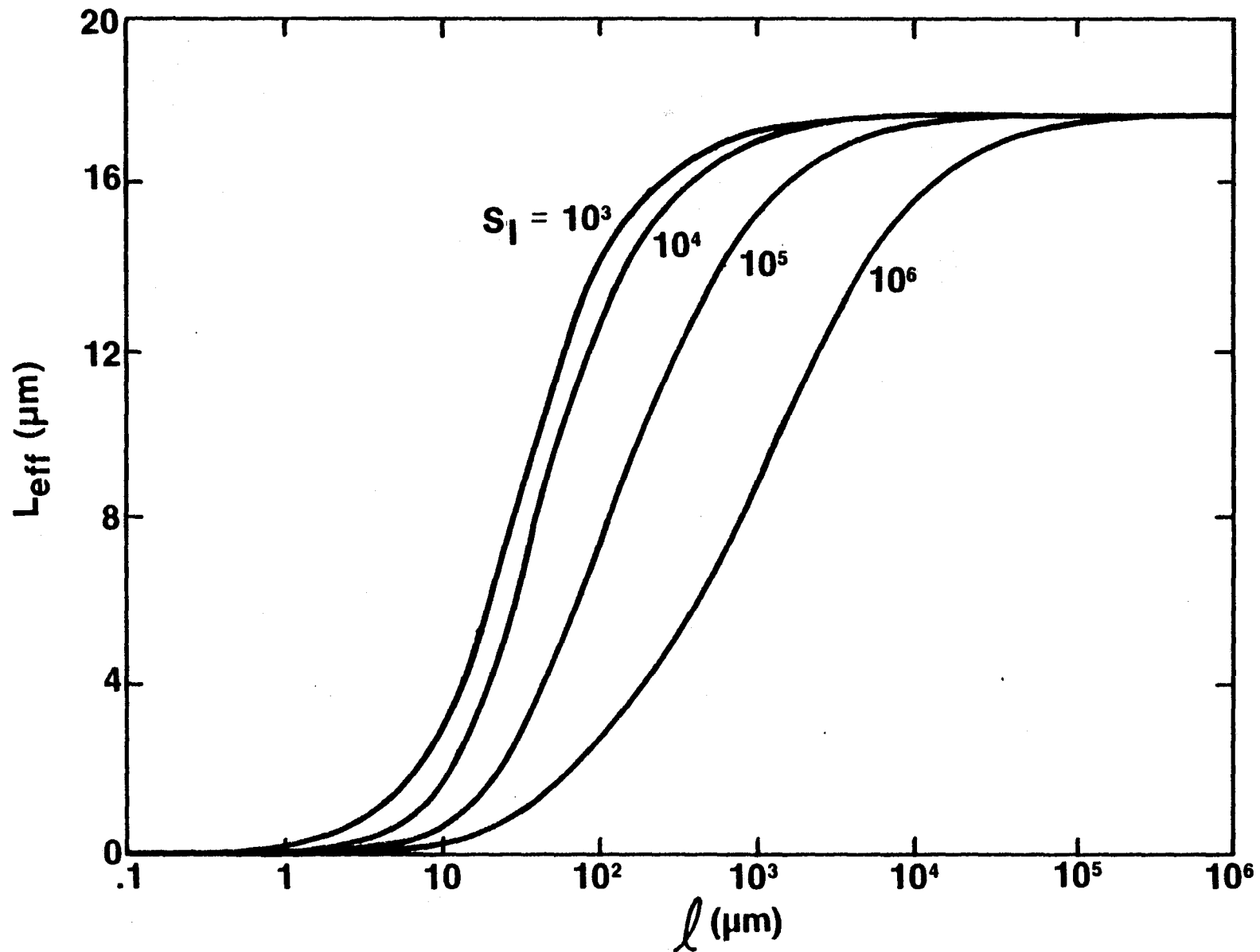Fig. 3-55 Detailed band diagram in vicinity of grain boundary (from Yee [202]).

Fig. 3-56 Diffusion length of CdTe as a function of grain size for several grain boundary recombination velocities (from Yee [202]).
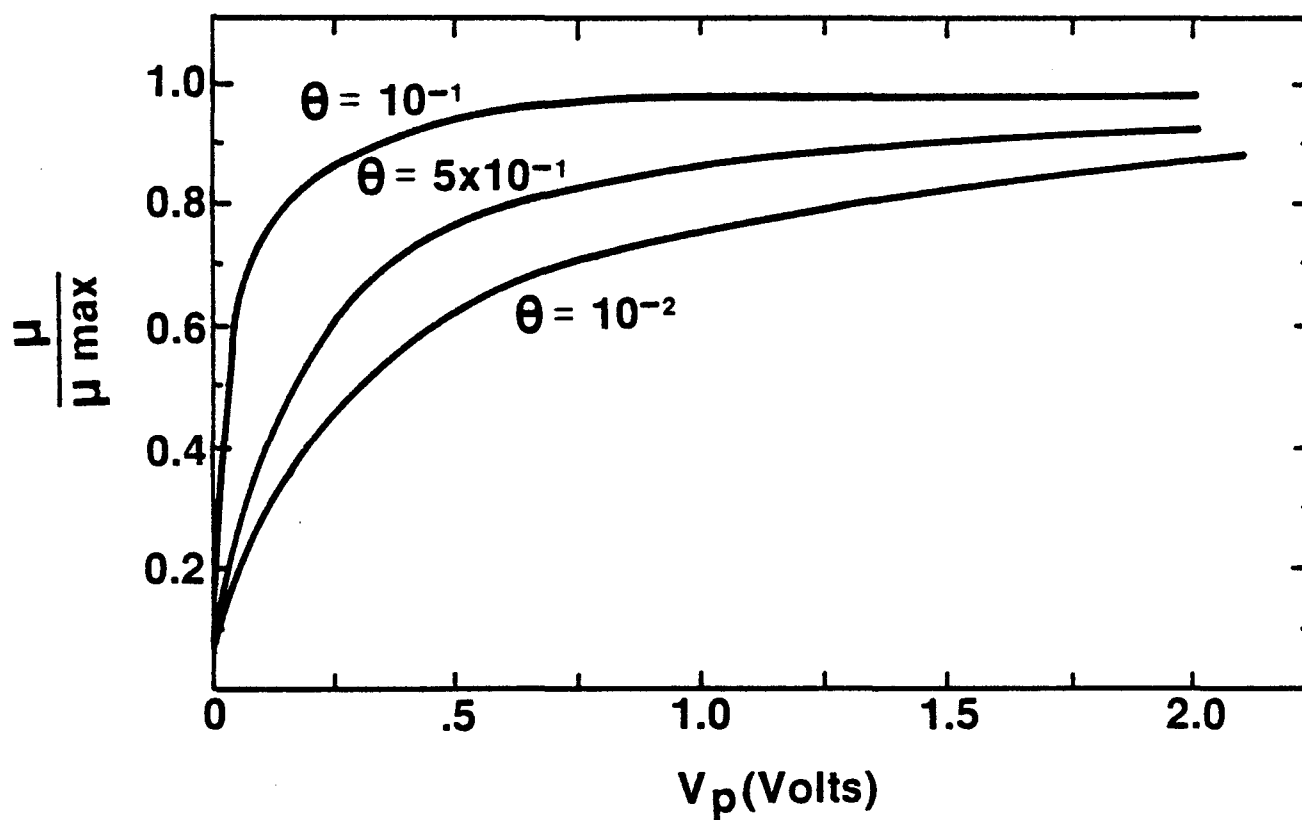
Fig. 3-57 Calculated dependence of Hall mobility, normalized to maximum
value, on surface potential for various surface state densities. θ
is the ratio of induced free charge to trapped charge in surface
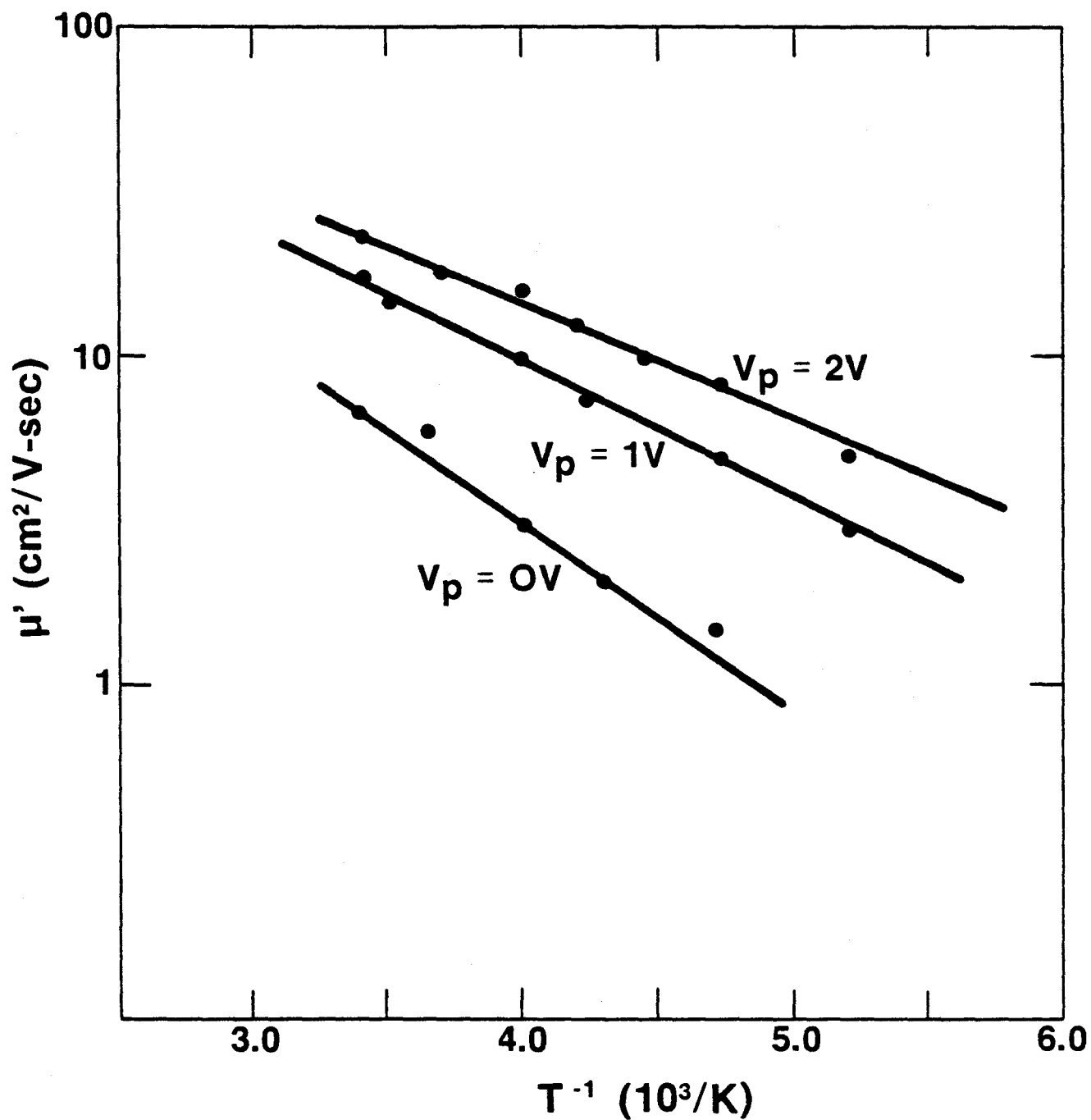states and traps (from Waxman et al. [32]).

Fig. 3-58 Variation of Hall mobility with inverse temperature for various applied surface potentials in SiO-CdS thin film field effect structure (from Waxman et al. [32]).

DISTRIBUTION LIST

No. of Copies	Distribution
1·	Department of Energy: DOE, SERI Site Office Contracting Officer Attn: Charles M. Skinner
1	Chicago Operations Office Interim Program Division Attn: M. E. Jackson
1	Division of Solar Technology Office of Asst. Director for Administration Attn: R. H. Annan
1	Office of Asst. Secretary for Conservation & Solar Applications Attn: R. Scott
1	Office of Solar, Geothermal, Electric & Storage Programs Attn: Martin Adams
1	Division of Energy Technology Administration Attn: S. Hansen
1	Division of Distributed Solar Technology Office of the Director Attn: R. San Martin
1	Division of Central Solar Technology Office of the Director Attn: H. Coleman
1	Division of Energy Storage Systems, ETS Office of the Director Attn: G. Pezdirtz
1·	Division of Planning & Energy Transfer, ETS Office of the Director Attn: Leslie Levine
1	Wind Energy Systems Attn: L. Divone